

Device Architectures for Improved Temporal Response with Amorphous Selenium Radiation Detectors

by

Ahmet Camlica

A thesis
presented to the University of Waterloo
in fulfillment of the
thesis requirement for the degree of
Doctor of Philosophy
in
Electrical and Computer Engineering

Waterloo, Ontario, Canada, 2019

© Ahmet Camlica 2019

Examining Committee Membership

The following served on the Examining Committee for this thesis. The decision of the Examining Committee is by majority vote.

External Examiner: Sven Achenbach
Professor, Dept. of Electrical and Computer Engineering,
University of Saskatchewan

Supervisor(s): Karim S. Karim
Professor, Dept. of Electrical and Computer Engineering,
University of Waterloo
Denny Lee
Professor Adjunct, Dept. of Electrical and Computer Engineering,
University of Waterloo

Internal Member: Guoxing Miao
Associate Professor, Dept. of Electrical and Computer Engineering,
University of Waterloo

Internal Member: Michael Reimer
Assistant Professor, Dept. of Electrical and Computer Engineering,
University of Waterloo

Internal-External Member: Eihab Abdel-Rahman
Professor, Dept. of System Design Engineering,
University of Waterloo

I hereby declare that I am the sole author of this thesis. This is a true copy of the thesis, including any required final revisions, as accepted by my examiners.

I understand that my thesis may be made electronically available to the public.

Abstract

Amorphous selenium (a-Se) is a commercially mature direct conversion photoconductor capable of very high spatial resolution that enables the early detection of small and subtle lesions in breast cancer screening and diagnostics. However, a-Se exhibits poor collection efficiency due to low carrier mobility and charge trapping related to its amorphous nature. Release of trapped electrons gives rise memory artifacts such as photocurrent lag, that can last for several seconds after the cessation of the X-ray pulse, thus making a-Se a challenging material for use in high spatial resolution dynamic imaging applications.

In this research, the intrinsic causes of temporal behaviour in a-Se photoconductor are investigated using lag, ghosting and pulse height spectroscopy (PHS) measurements on conventional a-Se detectors. The measured data is compared to the data obtained with alternative a-Se imaging device architectures for improved dynamic imaging performance. The alternative device architectures include: (1) use of a polyimide blocking layer that permits the operation of a-Se devices with higher electric fields, (2) a high field capable solid-state unipolar charge sensing detector that can achieve hole-mostly charge sensing and (3), small pixel geometries to obtain the small pixel effect (SPE).

Theoretical and experimental results show that an image lag of less than 1.5% is achieved using the solid-state unipolar charge sensing detector for dynamic imaging which is in stark contrast to measurements performed on conventional a-Se imaging devices that exhibit a lag of up to 16%. PHS measurements are also presented that demonstrate, for the first time, a measured energy resolution of 8.3 keV at 59.5 keV was for the unipolar charge sensing device in contrast to 22 keV at 59.5 keV for conventional a-Se devices. Also, the photon counting ability of a-Se photoconductor was demonstrated by integrating a SPE capable a-Se detector with a CMOS pixel array having $11 \times 11\text{-}\mu\text{m}^2$ pixels. Measured results on this CMOS array using a mono-energetic radioactive source are presented which indicate for the first time, that amorphous semiconductors can be used for photon-counting X-ray imaging applications.

The research results indicate that mature large-area a-Se photoconductor, when incorporated with a single polarity charge sensing device design such as SPE or the solid-state unipolar charge sensing detector, can meet the requirements of high spatial resolution dynamic medical imaging applications such as spectral mammography or even microangiography without resorting to new sensor materials or crystalline semiconductors that are challenging to scale up to larger areas because of cost and yield issues associated with growth and bonding technology.

Acknowledgements

First and foremost, I would like to thank Dr. Karim S. Karim for his guidance, encouragement, and trust, throughout this academic endeavor.

I lack the words to express my gratitude to Dr. Denny Lee for his unconditional support. My collaboration with Dr. Lee was one of the best times of my PhD. He was always there for me to discuss all of my new ideas, and to encourage me. He truly is a good role model and always has many insightful comments and suggestions.

I would like to show appreciation to my examining committee, Dr. Sven Achenbach, Dr. Guoxing Miao, Dr. Michael Reimer, and Dr. Eihab Abdel-Rahman, for accepting to review my work.

I would like to thank Dr. Peter M. Levine for help with the pulse-height spectroscopy setup and Dr. M. Z. Kabir and Salman Arnab for help with the theoretical analysis of the hole conduction mechanism in polyimide and the simulation studies of the unipolar charge sensing detector.

I am highly grateful to Hyunsuk Jang of Vieworks Co, who always supported me and was very generous with his time for discussions related to my project. Collaboration with Vieworks Co. was instrumental to the success of this work. Additionally, I would like to thank the Government of Turkey for its support of my research in the form of Ministry of Education Scholarship.

I would like to thank Richard Barber and Dr. Czhang-Ho Lee for their support in keeping the G2N tools and lab operational, in ensuring our safety in the clean room, and for their valuable suggestion.

I would like to thank all members of the Silicon Thin-Film Applied Research (STAR) group, past and present, for their friendship and advice. Special thanks go to Jerry Liang, Abdallah El-Falou, and Hummer Li for the invaluable support and discussion on the electronics of the characterization system.

Special thanks go to my family for their love, encouragement and care. I cannot imagine finishing all my achievements without their endless moral support.

Finally, thanks to my wife, Zehra, and to my son, Yusuf Asaf, for their endless love, patience, support and for shining a different color onto my life.

To my wife, Zehra, and my son, Yusuf Asaf,

whose love and supports are the treasure of my life.

Table of Contents

List of Tables	xiv
List of Figures	xv
1 Introduction	1
1.1 Digital radiology	1
1.2 Direct vs. indirect conversion	4
1.3 Amorphous selenium as a photoconductor	6
1.4 Energy integration vs. photon counting	9
1.5 Motivation	12
1.6 Objective	13
1.7 Thesis organization	15
2 Metrics of Detector Performance	17
2.1 Introduction	17
2.2 X-ray interactions in photoconductors	18
2.3 Charge transport in amorphous semiconductors	20

2.3.1	Time-of-flight technique	23
2.4	Performance metrics of digital X-ray detectors	24
2.4.1	Sensitivity	26
2.4.2	Dark current	29
2.4.3	Noise	31
2.4.4	Temporal response	33
2.5	Conclusion	34
3	Device Structure to Achieve Low Dark Current Amorphous Selenium Radiation Detectors	35
3.1	Introduction	35
3.2	Method and materials	37
3.2.1	Device fabrication	37
3.2.2	Measurement setup and experimental details	40
3.3	Results and discussion	43
3.3.1	Pulse height spectroscopy measurements	43
3.3.2	Dark Current Measurements	44
3.3.3	Photoresponse	46
3.4	Mathematical Model	49
3.5	Conclusion	52
4	Modeling of Amorphous Selenium Based Unipolar Charge Sensing Detectors	54
4.1	Introduction	54

4.2	Induced signal analysis	56
4.2.1	The Shockley-Ramo theory	58
4.2.2	Unipolar charge sensing	60
4.3	Simulation results	62
4.3.1	Signal rise-time	63
4.3.2	Charge collection efficiency	66
4.3.3	Energy resolution	70
4.3.4	Swank noise	74
4.3.5	Monte Carlo simulation	75
4.4	Conclusion	79
5	Fabrication and Experimental Characterization of Unipolar Charge Sensing Detector	82
5.1	Introduction	82
5.2	Design and fabrication of the unipolar charge sensing detector	85
5.3	Pulse height spectroscopy setup	92
5.3.1	Noise analysis and linearity measurements	96
5.4	Experimental results	98
5.4.1	Spectral performance of conventional detectors	98
5.4.2	Device operation and charge transfer measurements of unipolar charge sensing detectors	107
5.4.3	Transient signal measurements	111
5.4.4	Spectral performance of unipolar charge sensing detectors	114
5.5	Photocurrent lag and ghosting measurements	116

5.5.1	Measurement setup and method	117
5.5.2	Experimental results	119
5.6	Conclusion	123
6	Amorphous Selenium Based CMOS-Integrated Single-Photon-Counting X-Ray Detector	125
6.1	Introduction	125
6.2	Sensor characterization	126
6.3	Detector design and implementation	128
6.4	Experimental results and discussion	131
6.5	Conclusion	132
7	Conclusions and Recommendations for Future Work	135
7.1	Conclusions	135
7.2	Recommendations for future work	138
	References	142

List of Tables

1.1	Digital X-ray imaging systems properties[1]	3
1.2	Material properties of selected direct conversion photoconductors [2]	6
2.1	Selected properties of un-doped and stabilized a-Se photoconductor. a= Undoped a-Se, b= stabilized a-Se [3]	25
3.1	Spin-coating and curing parameter of the PI layer.	37
3.2	Deposition conditions for a-Se films using thermal evaporator in G2N lab. .	40
4.1	a-Se parameters used in simulation studies. * indicates the parameters used for simulation studies of a-Se device with a poor electrical properties [3, 4].	66
4.2	Calculated parameters of conventional a-Se detector based on the Monte- Carlo simulation results	80

List of Figures

1.1	Digital X-ray image acquisition system and an X-ray image of a hand (image courtesy of ANRAD corporation).	2
1.2	a) Direct conversion of X-rays using a photoconductor which directly converts X-rays to electrical charges for collection. b) Indirect conversion of X-rays using a scintillator material which first converts X-ray photons into optical photons. Then the optical photons are converted to electrical charges by photodiodes. Spatial resolution of indirect conversion detectors is degraded due to lateral spreading of optical light.	5
1.3	Density of electronic states in amorphous selenium proposed by Abkowitz [5]	8
1.4	a) A PPS energy integrating pixel for photoconductor charge collection and storage. b) A 3T APS energy integrating pixel for photoconductor charge collection and storage.	10
1.5	Simplified circuit diagram of a typical photon counting system.	11
2.1	a) In Compton scattering, an incident X-ray interacts with an outer-shell electron, and creates an electron of kinetic energy E'' , an ionized atom, and a scattered X-ray photon of energy E' , b) in the photoelectric effect, the energy of an incident X-ray is fully absorbed by an electron, which is ejected from the atom causing ionization. An electron from the outer shell fills the vacancy in the inner shell, which creates a fluorescent X-ray [6].	19

2.2	a) Bremsstrahlung radiation is produced when energetic electrons are decelerated by the electric field of target nuclei, b) if an electron is liberated from an inner core shell, there exists a vacancy in its parent atom. A cascade of electron transitions can occur, which can produce one or more characteristic X-rays.	20
2.3	Density-of-states in amorphous semiconductors as proposed by Mott. Localized states are shaded and E_c and E_v refer to the mobility edges for the conduction and the valence bands, respectively. Reprinted from [7] with permission granted.	21
2.4	Energy diagram for an electron bound to a point charge in the presence of a uniform electric field (Poole-Frenkel effect) [8, 9, 10].	23
2.5	Schematic of time-of-flight experimental setup used for the charge transport measurements in a-Se device.	25
2.6	Comparison of x-ray attenuation coefficients for Si ($Z = 14$), CdTe ($Z = 48$; 52), HgI ₂ ($Z = 80$; 53), and a-Se ($Z = 34$). Generated using [11]	27
2.7	Images that demonstrate the appearance of lag and ghosting.	33
3.1	a) Schematic of the fabricated PI/a-Se detectors and PHS experimental setup. The feedback circuit of the preamplifier (A250CF) is optimized for a lower gain and a slower response of a-Se. Three different samples are fabricated with a various PI thickness ($0.8 \mu\text{m}$, $1.8 \mu\text{m}$ and $3 \mu\text{m}$).	38
3.2	Selenium evaporator in G2N lab (left); the evaporation assembly inside the vacuum chamber (right).	39

3.3	a) The measured ^{241}Am (59.4 keV) spectra of a-Se/PI detectors with a different PI thickness and same applied voltage, 750V, b) The corrected ^{241}Am spectra of a-Se/PI detectors for the same applied field, i.e., $10\text{V}/\mu\text{m}$. The required fraction of the applied voltage per $1\ \mu\text{m}$ PI layer is estimated around 60 V to achieve the same internal electric field for a-Se detectors having different thickness of PI layers.	44
3.4	a) Dark current density of a-Se detectors a) as a function of applied voltage, b) as a function of applied electric field. The dark currents are measured after 3600 second following the high-voltage application.	45
3.5	a) Photocurrent measurement results for the same applied voltage, i.e., 750 V, and b) same applied electric field, i.e., $10\ \text{V}/\mu\text{m}$. Detectors were exposed to X-ray pulses similar to that of fluoroscopy, (i.e., 30 fps at $10\ \mu\text{R}/\text{frame}$),	47
3.6	Photo-to-dark current ratio of the PI/a-Se detector as a function of PI thickness at various electric fields.	48
4.1	a) Cross section of a conventional pixelated detector, b) Cross section of a detector with an internal grid layer, c) Weighting potential distribution for a conventional and unipolar charge sensing detector.	58
4.2	Cross-sectional view of (a) conventional and (b) unipolar charge sensing detectors, (c) simulated weighting potentials for the detector in (a) and (b), (d) and electric field simulation of unipolar charge sensing detector.	61
4.3	Normalized collected charge as a function of time for three interactions depths, 0.2L, 0.5L and 0.8L. (a) simulations are performed for a conventional selenium detector without the grid, (b) a unipolar selenium detector with a grid pitch of $50\ \mu\text{m}$, (c) $35\ \mu\text{m}$ and (d) $20\ \mu\text{m}$	65

4.4	Calculated charge induction efficiencies as a function of thickness for two different a-Se detector with a different charge transport properties as shown in Table 4.1, a) simulated for the electrical parameters of the fabricated device (for $d_{a-Se}=70 \mu m$), b) simulated for the poor transport properties of an a-Se device reported in the literature (for $d_{a-Se}=70 \mu m$), and c) simulated for the electrical parameters of the fabricated device (for $d_{a-Se}=105 \mu m$).	69
4.5	Examples of energy spectrum. Good energy resolution (red) and poor energy resolution (black) are provided for comparison.	71
4.6	Flow chart for the Monte-Carlo simulation of the signal formation process in amorphous selenium x-ray detectors [12].	76
4.7	Simulated pulse-height spectra for mono-energetic gamma-ray sources a) for ^{241}Am and c) for ^{57}Co) as a function of applied electric field, b) and d) demonstrate some of the Gaussian fitted curves (at $10 V/\mu m$) to calculate the parameters in the Table 4.2.	78
5.1	A total of 6 detector arrays with a various pixel pitch were fabricated on a single glass substrates. The pixel pitch of the detectors are $20 \mu m$, $35 \mu m$ and $50 \mu m$	86
5.2	Schematic representation of a) the pixel array and c) a single pixel, b) cross-section of the unipolar charge sensing detector (2-D) and d) single pixel (3-D).	87
5.3	Fabricated unipolar charge sensing detectors and part of their micrograph (a) with and (b) without evaporated selenium.	89
5.4	Explanation of fabrication process steps.	91

5.5	a) Pulse-height spectroscopy experimental setup for energy and time resolution measurement, b)copper housing with a vibration isolation foam, c) aluminium housing for the front-end electronic and the detector, d) a-Se detector on the low-noise custom-designed PCB, e) the CUBE preamplifier attached to the PCB, and f) the Dante ADC.	93
5.6	Circuit diagram of the PHS system and a typical output pulses of the preamplifier (yellow trace) and the shaper (green trace).	94
5.7	a) Output of the CUBE preamplifier, b) output of the shaper, c) output of the MCA for the input test pulses.	98
5.8	a) Output signal of the Dante ADC, b) linearity test results of the PHS system, c) Illustration of Gaussian noise parameters.	99
5.9	Measured energy spectrum by the a-Se conventional detector with a) ^{241}Am and b) ^{57}Co gamma-ray sources as a function of applied electric field. . . .	100
5.10	a) Measured ionization energy vs. applied electric field, b) adapted from Blevis et al [13], and simulated ionization energy vs. electric field.	101
5.11	^{241}Am spectra obtained by our conventional a-Se detector, Blevis et. al [13] and Monte-Carlo simulation.	102
5.12	a) Measured σ vs. E, b) adapted from Blevis et al. [13] and simulated σ vs. E.	103
5.13	Measured energy resolution of the conventional a-Se detector for the incident gamma-ray sources of ^{241}Am and ^{57}Co	104
5.14	a) Measured Swank vs. E, b) adapted from Blevis et al. [14] and simulated Swank vs. E.	105
5.15	Calculated Swank noise based on Gaussian fitting and full spectrum. Reprinted from [12] with permission granted.	106

5.16	Simulated electric field stream lines for the device having a 20- μm pixel pitch. Inset shows the required grid voltage for the same device configuration for various pixel pitch, 20, 35 and 50 μm	108
5.17	Experimental Setup used for charge transfer measurements.	108
5.18	Charge transfer measurement for (a) 50 μm pixel, (b) 35 μm pixel, (c) 20 μm pixel at approximately 8 V/ μm	110
5.19	Collected charge as a function of time at $E = 8 \text{ V}/\mu\text{m}$ for a single gamma-ray photon interaction. For the conventional planar detector, signal rise-time is highly depth dependent and in the worst-case it is electron-transit-time-limited. However, for the unipolar charge sensing detector, signal risetime is substantially reduced due to near-field effect. Insets show the results for the multiple events.	113
5.20	Spectrum of ^{241}Am obtained from the conventional and unipolar charge sensing a-Se detectors at 8V/ μm . Simulation result is also included (adapted from Stavro et. al. [15]).	115
5.21	Typical output signal of a-Se detector under continuous X-ray pulse illumination [16].	118
5.22	Photocurrent pulses obtained for first frame lag measurements by conventional and unipolar charge sensing devices.	119
5.23	Ghosting measurement results for conventional detector as a function of accumulated dose for various applied field.	120
5.24	Photocurrent measurements results for average lag estimation a) Unipolar charge sensing device with 20- μm pixel b) Conventional a-Se device with PTCBI hole blocking layer.	122
6.1	Time-of-flight (TOF) transient photoconductivity measurements of an a-Se sensor showing the response of (a) holes and (b) electrons.	127

6.2	Simplified cross-section of the CMOS-integrated a-Se SPC X-ray detector.	128
6.3	Photograph of the $4 \times 3\text{-mm}^2$ SPC X-ray detector IC.	129
6.4	CMOS pixel circuit schematic, consisting of two amplifier stages followed by a latch. Capacitor C_i represents the parasitic input capacitance of the pixel. Output-offset correction of amplifier PA1 is implemented with capacitors C_{os} .	130
6.5	Timing diagram showing the three-phase operation of the CMOS pixel circuit. Reset dead time is $0.3\mu\text{s}$ and the integration (track) phase lasts for $9.7\mu\text{s}$	130
6.6	Calibrated pulse-height spectrum from measurement of a $70\text{-}\mu\text{m}$ -thick a-Se sensor exposed to a mono-energetic $59.5\text{-keV } ^{241}\text{Am}$ source.	131
6.7	Experimental setup of the integrated a-Se SPC detector. The Al/Pb collimation tube attached to the lid (containing the radiation source) is aligned with the SPC chip surface using a precision stepper. The source to detector distance is 7 mm	132
6.8	Measured counting results from 80 adjacent pixels in one row of the CMOS-integrated SPC detector when exposed to a mono-energetic $60\text{-keV } ^{241}\text{Am}$ source.(a)Counted photons per pixel with the radiation source present and absent (dark).(b)Hit probability versus input generated charge.(c)Histogram of detected photons.(d)Histogram counts for threshold offset.	133

Chapter 1

Introduction

1.1 Digital radiology

Radiography is an imaging technique where X-rays are emitted from an X-ray source are transmitted through a patient and are detected in a detector. X-ray imaging provides two-dimensional representation of the three-dimensional non-uniformly composed structure. The degree of X-ray attenuation is based on the material composition and density along the path of the X-ray beam. Thus, the X-ray intensity is modulated through the overlapping structures and the corresponding two-dimensional contrast image is formed. A typical digital X-ray image acquisition system is shown in Fig .1.1.

The invention of X-rays by Wilhelm Rontgen in 1895 opened a new era not only in medical imaging, but also in science and industry with the applications ranging from clinical diagnostics to protein crystallography and non-destructive testing [17, 18, 19, 20]. The conventional detector consists of photographic film coupled with a light emitting phosphor screen which is packaged in a light-tight cassette. X-ray photons are first converted to visible lights by the phosphor screen. Then, photographic film is exposed to visible light creating a latent image. Finally, a permanent X-ray image is formed by the chemical development process. The quality of the X-ray image obtained from the conventional

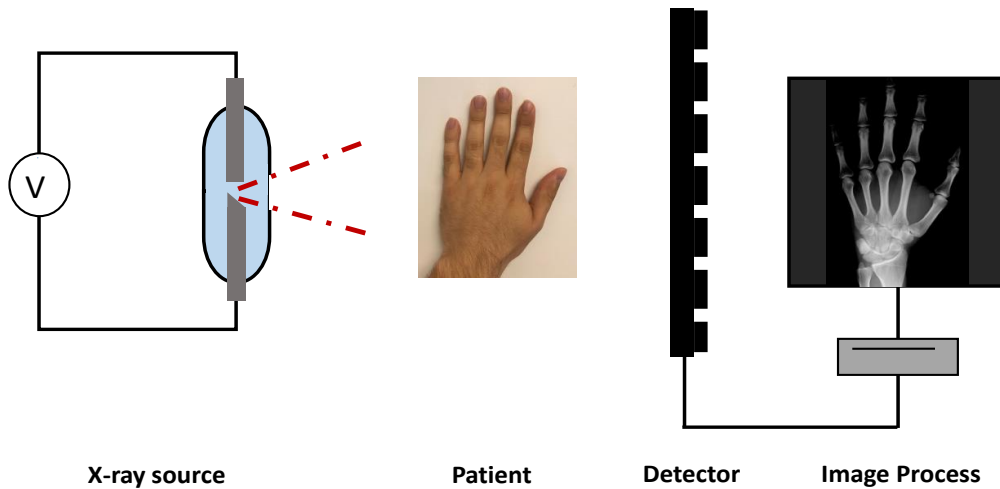


Figure 1.1: Digital X-ray image acquisition system and an X-ray image of a hand (image courtesy of ANRAD corporation).

detectors has been greatly improved over the last century. For this reason, this system has been accepted by radiologists who do not feel the need to replace it with its digital counterpart. However, the conventional X-ray imaging systems possess considerable drawbacks such as digital incompatibility, respectively higher X-ray doses and difficulties with storing and transferring X-ray images. When it comes to the dynamic imaging required for interventional radiology such as angiography, image intensifiers integrated with charge-coupled devices (CCD) or complementary metal oxide semiconductors (CMOS) have been widely employed. In this device, the final X-ray image is formed in several steps. First, the X-ray photons are converted to optical photons, which are then converted to electrons by a photocathode. The electrons are accelerated across the vacuum tube and are focused down to the size of the output window. They are then viewed by a camera. All these steps to convert X-ray images to visible light compromises image quality [21]. Furthermore, a complex lens and mechanical systems along with an array of CCD or CMOS result in cost and size issues.

Considerable research has been conducted in recent years to replace these conventional

Table 1.1: Digital X-ray imaging systems properties[1]

Clinical task	Chest radiography	Mammography	Fluoroscopy
Detector size	35 cm x 43 cm	18 cm x 24 cm	25 cm x 25 cm
Pixel size	200 μm x 200 μm	50 μm x 50 μm	250 μm x 250 μm
Number of pixels	1750 x 2150	3600 x 4800	1000 x 1000
Readout time	< 5 s	< 5 s	1/30 s
X-ray spectrum	120 kVp	30 kVp	70 kVp
Mean exposure	300 μR	12 mR	1 μR
Noise level	6 μR	60 μR	0.1 μR

static and dynamic X-ray imaging systems with their digital counterparts. The most recent technology for digital radiography is the flat panel detector (FPD) which benefits from the amorphous silicon thin-film transistor (TFT) active matrix array which has been highly developed by the digital display technology. FPDs are compatible to both static and dynamic X-ray imaging. For instance, FPDs are currently able to readout entire images in 1/60 seconds (60 Hz), which is sufficient for fluoroscopy [22].

There are several modalities that utilize the digital FPDs in medical imaging. In order to generate images with the same or possibly better temporal and spatial resolutions compared to conventional imaging systems, the digital FPDs should meet some requirements as outlined in Table 1.1 [1]. Most of these requirements have been tackled with current technology. However, achieving low noise is still a challenging task especially for dynamic imaging. In fact, there have been extensive research efforts to reduce the noise by either changing the material composition and structure of the detector, or the read-out circuit technology.

1.2 Direct vs. indirect conversion

Digital X-ray detectors consist of two main components: an X-ray absorption layer and a read-out circuit. The first component converts X-rays to electrical charges while the second component stores and transfers these electrical charges to the off-panel circuitry. The common taxonomy of digital X-ray detectors is based on the X-ray detection methods by the X-ray absorption layer. In direct conversion, X-rays are absorbed by a photoconductive layer (e.g., a-Se, CdZnTe, HgI₂ or PbO), and converted to electrical charges which are collected under an applied electrical field right after [23, 24]. However, indirect conversion requires two stages of the conversion layer. First, X-rays are converted to visible photons by the scintillator layer (e.g., CsI or Gd₂O₂S), and then these visible photons are converted to electrical charges by an auxiliary photodetector, which can be either Schottky MIM/MIS diode or PIN photodiode. In both direct and indirect detection, the generated charge is collected by a solid-state readout circuit such as amorphous silicon (a-Si) TFT or CMOS. Fig. 1.2 shows the schematic of direct and indirect conversion detectors.

Indirect detection detectors suffer from the lateral spreading of the optical light, which causes secondary blur within the image and degrades spatial resolution [25, 26]. Recently, needle-like scintillator structures were introduced to inhibit the lateral spreading of the photons, but the degree of the spatial resolution improvement was found to be limited with this structure [27]. Most of the currently available digital X-ray detectors that do not require higher spatial resolution are based on indirect detection. The high temporal response of PIN diode and easy coupling to a scintillator material make an indirect detection detectors a good candidate, especially for the dynamic imaging applications.

The inherent limitation of spatial resolution with an indirect detection detectors can be overcome using the direct detection method. Under the high voltage applied to the photoconductor, a uniform electric field is created, and all the generated charges are driven to either the top or bottom surface of the photoconductor layer to be collected by a readout circuit. Lack of light spreading and the application of an electric field with a direct detection detector enable the achievement of higher spatial resolution [25, 28]. However, a

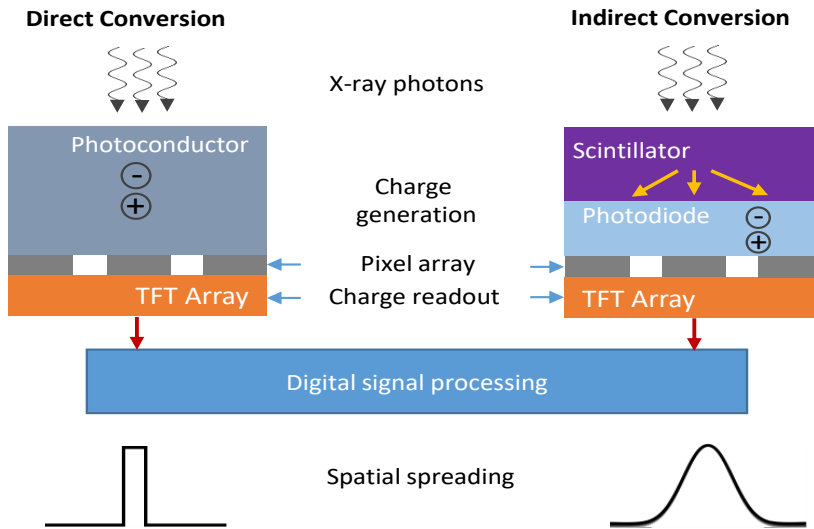


Figure 1.2: a) Direct conversion of X-rays using a photoconductor which directly converts X-rays to electrical charges for collection. b) Indirect conversion of X-rays using a scintillator material which first converts X-ray photons into optical photons. Then the optical photons are converted to electrical charges by photodiodes. Spatial resolution of indirect conversion detectors is degraded due to lateral spreading of optical light.

requirement of a high voltage supply is a drawback of this type of detection.

For a photoconductor to be a good candidate for a direct detection detector, it should have specific material properties [23, 29]. A higher atomic number is desirable so that almost all the incoming X-ray photons are absorbed within the practical photoconductor thickness to reduce the patient dose. The amount of the radiation energy required to generate the electron-hole pair should be as low as possible to have higher intrinsic sensitivity. Lower dark current is required to create higher dynamic range. The mobility and life time product for carriers should be within the practical range to efficiently collect photoinduced charge. The transit time for the lower mobility carrier should be less than the image read-out time or the inter-frame time of the dynamic type detector. Repeated x-ray exposures should not change the photoconductors intrinsic properties and should not create X-ray fatigue. The photoconductor should be easily coated to a large area for a reasonable cost

Table 1.2: Material properties of selected direct conversion photoconductors [2]

Photoconductor	Absorption depth at 30 keV (μm)	W (eV)	Resistivity ($\Omega\cdot\text{cm}$)	$\mu_e\tau_e(\text{cm}^2/\text{V})$	$\mu_h\tau_h(\text{cm}^2/\text{V})$
a-Se	149	50	$10^{14} - 10^{15}$	$0.3 \times 10^{-6} - 10^{-5}$	$10^{-6} - 6 \times 10^{-5}$
CdZnTe	81	5	10^{11}	2×10^{-4}	3×10^{-6}
HgI ₂	91	5	4×10^{13}	$10^{-5} - 10^{-4}$	10^{-6}
PbI ₂	137	5	$10^{11} - 10^{12}$	7×10^{-8}	2×10^{-6}

without very high temperature so that damage does not occur in the active matrix array.

Currently, amorphous-selenium (a-Se), cadmium telluride (CdTe) and cadmium zinc telluride (CZT) are the only commercially available direct conversion photoconductors that meet some of the aforementioned requirements [30, 31, 32, 33, 34]. Material properties of some direct conversion photoconductors which might be potentially used in the future are summarized in Table 1.2 [2].

1.3 Amorphous selenium as a photoconductor

A-Se is one of the most highly developed photoconductors due to its technological importance in the photocopying industry. A-Se served as a photoreceptor of office copiers (i.e., Xerox 914) for over three decades after the mid-1950s before being replaced by modern inexpensive organic materials. The atomic number of selenium is 34 and it is a member of the VI Column in the periodic table. Selenium can be found in both crystalline and amorphous form in nature. The experimental observations of the electronic and optical characteristics of a-Se are essentially interpreted through its density of states (DOS) band diagram [35, 36, 37]. Due to the presence of long-range disorders in amorphous materials, DOS for a-Se is complicated and still not understood very well [38]. The most accepted DOS model for a-Se is based on the Abkowitz DOS model, which was derived from a series of experimental results of time of flight (TOF) transient photoconductivity, xerographic

dark discharge and residual voltage decay measurements [5]. The DOS model proposed by Abkowitz is shown in Fig. 1.3. The notable feature of this DOS model is that there are extended states from the conduction band (CB) and valance band (VB) edges along with the four sets of defect states within the bandgap. The defect states close to the CB and VB are shallow electron and hole traps, respectively. Near the Fermi level, deep electron and hole traps exist. The electron mobility is controlled primarily by shallow traps, where charge carriers are captured and released several times while traversing a photoconductor. Therefore, the effective drift mobility is modified by the time they spend in the trap state. The conduction mechanism in a-Se is considered to be trap limited transport. On the other hand, deep electron and hole trap states determine the lifetime of charge carriers. In the case of X-ray imaging applications, the photoconductor sensitivity, which is mainly defined by the Schubweg¹ of the charge carriers, will be limited by deep trap concentration. Note that the deep hole trap state stays at 0.87 eV from the edge of the VB, and the electron deep trap state stays at 1.22 eV from the edge of the CB. A-Se has the band gap of 2.22 eV.

Pure a-Se tends to crystallize over time and its electrical properties are altered [39, 40]. Selenium used for FPDs is called stabilized a-Se. The rate of crystallization can be reduced by alloying a-Se with a small amount of Arsenic (As) [3]. However, this doping process introduces more deep hole trap states and reduces hole life time [9]. This can be compensated by adding Chlorine (Cl) (10-20 ppm). The thermal stability and carrier transport properties of stabilized a-Se can be optimized by adjusting the amount of As and Cl [41].

Digital X-ray detectors should be at least the same size as the object that is being imaged since X-rays cannot be focused. A-Se is well-suited for X-ray detector fabrication because it can be easily vacuum-coated over a large area up to 1000 μm with good uniformity [3]. Since the substrate temperature is increased up to 65-70 degrees C at most during the evaporation, the process does not damage the readout circuit such as a-Si TFT active

¹The average drift distance by a free charge carrier is called Schubweg and given by $\mu\tau E$, where μ and τ are the mobility and the lifetime of the carrier, respectively, and E is the applied electric field.

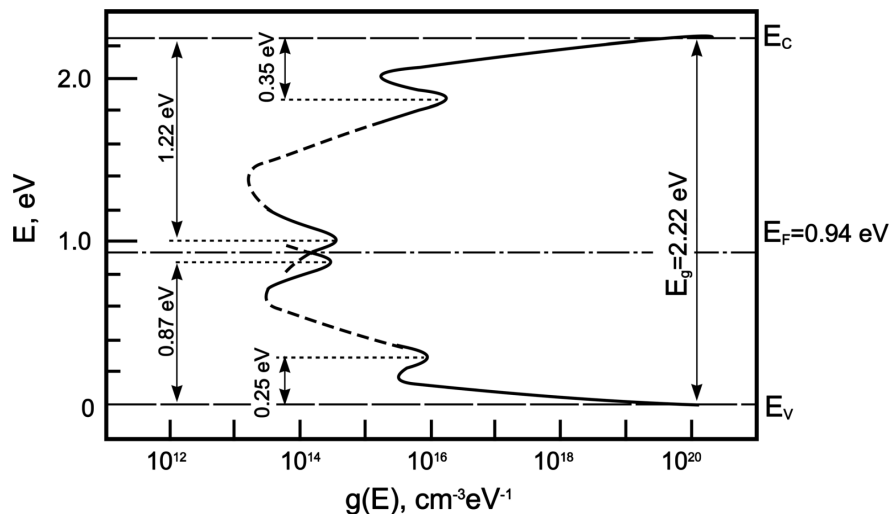


Figure 1.3: Density of electronic states in amorphous selenium proposed by Abkowitz [5]

matrix array [42]. In addition, despite the lower atomic number of a-Se, evaporation of the thick layer allows almost full absorption of X-ray photons within the medical imaging energy range. Some of the polycrystalline materials can be fabricated over a large area as well, but these materials exhibit a high dark current due to grain boundaries [3]. A-Se is a highly resistive material ($\sim 10^{14}\Omega\cdot\text{cm}$), thus, the dark current through a-Se remains low even under the application of a relatively high electric field [43]. Another advantage of a-Se over the other photoconductors is that its K-edge is at 12.7 keV, which makes a-Se a suitable material for mammography [44]. Note that re-absorption of K fluorescent photon with higher energies occurs away from the initial photon interaction sides (e.g., possibly in neighboring pixels), which degrades the spatial resolution of the detectors. Due to the applied electric field and the absence of granularity noise, a-Se detectors provide unsurpassed spatial resolution.

Aside from all the advantages mentioned above, the main drawback of a-Se is that the charge transport properties of a-Se are still far from optimal to achieve acceptable charge collection efficiency, especially under a lower electric field with a thicker layer of a-Se [45, 46, 47, 48, 49, 50]. While the charge collection efficiency for holes is respectively

adequate, the collection efficiency for electrons is severely degraded due to the high density of energy-distributed defect states which causes a trapping of some drifting carriers through the photoconductor layer [51, 52].

1.4 Energy integration vs. photon counting

The type of readout circuits used to acquire X-ray induced charges can be mainly divided into two categories: energy integrating and photon counting. Each type of readout circuit has its own corresponding electronic parts for charge storing and processing [53]. However, the charge conversion process for both can be either direct or indirect. The conventional pixel architecture of an energy integrating detector is passive pixel sensor (PPS), shown in Fig. 1.4(a) for a direct conversion a-Se detector [54]. Basically, the working principle of the PPS is as follows: i) the generated charge by the X-ray interaction is directed towards the collecting electrode under the applied electric field, ii) then, the charge is stored on the storage capacitor, C_{st} , over a given time period (i.e., integration time), iii) finally, the stored charge is transferred to the external digital circuitry. For CMOS technology, the active pixel sensor (APS) is adopted [55]. An APS is typically comprised of three transistors (3T): a reset transistor that resets the storage capacitor, a source-follower that converts collected charge to voltage, and a pixel select transistor (Fig. 1.4(b)). An integrating circuit based on CMOS technology generally provides a better signal-to-noise ratio compared to PPS due to an on-chip multiplexer, especially for the small pixel where the X-ray induced signal is limited. The current PPS architecture is amplifier noise limited, especially for the low dose X-ray imaging applications where a high frame rate is required [56].

Today, most of the deployed imaging systems for medical diagnosis and industrial non-destructive testing are based on energy integration technology. Integrating systems accumulate the X-ray signal over a certain time interval and provide a measurement such that the weight, W , of every photon contributing to the formation of the image is proportional to its energy ($W \propto E$) [57]. Thus, higher energy photons contribute more to the image

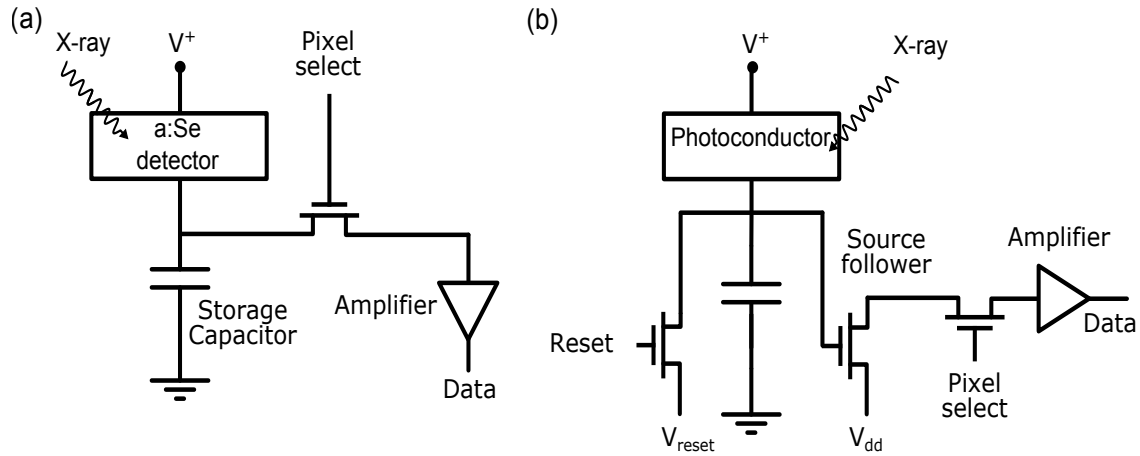


Figure 1.4: a) A PPS energy integrating pixel for photoconductor charge collection and storage. b) A 3T APS energy integrating pixel for photoconductor charge collection and storage.

signal than the lower energy ones. The energy information of the X-ray energy spectrum involved in the integration process is simply lost. However, for the mammography in which variations of soft tissues constitute the object to be imaged, lower energy photons carry more contrast information than transmitted photons of higher energy. Since the energy integration mode puts more weight on the photons with a higher energy, the weighting will be contrary to the information content. Generally, the lowest possible mean X-ray energy is utilized to enhance contrast of image, but this requires higher patient dose. To address this energy weighting problem, it is proposed that the optimal weighting factor for mammography should be inversely proportional to the cube of the photon energy, which is impossible to realize with an energy integrating systems [58, 57, 59]. Another limitation of the energy integration mode of operation is that integration systems are inherently confronted with the problem of noise that originates from both the detector and the read-out circuit. Poor noise rejection of the energy integrating system limits the signal-to-noise ratio (SNR) of the system and this deficiency is compensated at the expense of higher patient dose [60]. This is especially true in high frame rate applications, where short acquisition

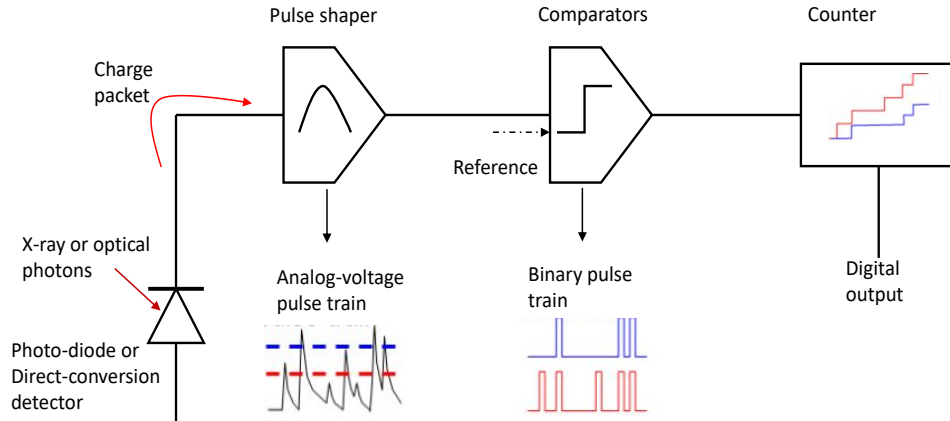


Figure 1.5: Simplified circuit diagram of a typical photon counting system.

times are required. The X-ray generated signal is respectively lower, and the integrated noise becomes more prominent.

Photon counting systems, however, do not measure the total intensity of the incident X-ray photons, but do measure the number of individual photons with the energy above a certain threshold. The measurable flux is therefore from a single photon to several million photons/pixel/second with a theoretically unlimited dynamic range [8]. Simplified circuit diagram of a typical photon counting system is shown in Fig. 1.5. The generated charge from a single photon interaction is amplified and altered to voltage output. Then, the output is compared to a low-level discriminator. Through sweeping the threshold voltage and subtracting consecutive images, an optimum threshold can be achieved. Ideally, the low-level discriminator must be high enough for optimum noise rejection and low enough to not acquire significant beam hardening. Signals exceeding the threshold are counted as a valid event and assigned the same weight. In this case, W is independent of energy and is equal to unity. Proper adjustment of the threshold level leads to optimum energy weighting, and the total patient dose can be reduced up to 20% compared to energy integration [61]. For a properly designed photon counting detector, there is no electronic and background

noise with an internal thresholding. Therefore, the system is defined as a quantum noise limited. Photon counting imaging has become possible due to advances in microelectronics that allow the design and fabrication of integrated circuits with pixelated pulse processing front-end electronics with low noise.

1.5 Motivation

Mammography requires higher spatial resolution to detect micro-calcifications in the breast, which are an early warning signal of breast cancer. Early detection of subtle lesions can improve cancer diagnosis and save lives. Currently, the highest performance direct imaging FPDs used for mammography are based on a-Se technology. This is because a-Se offers cost-effective and reliable coupling to large area readout circuitry, and more importantly, higher spatial resolution compared to other photoconductors, which is essential for mammography. However, this inherent spatial resolution has not been leveraged for real-time imaging applications. For example, micro-angiography for imaging fine brain vessels requires a spatial resolution approaching 20 lp/mm, which is achievable with selenium technology. The challenge is that a-Se detectors suffer from memory artifacts such as lag that limit the frame rate of the X-ray imager. The frame rate reduction is typically attributed to lag, which manifests itself as increased dark conductivity. With lag, the subsequent image frames carry spill over signal from the previous exposure. Increasing the pixel readout rate makes this problem worse and thus, overcoming the temporal artifacts becomes critical to enabling a-Se based higher spatial resolution real-time detectors for large area imaging.

In addition, there is considerable interest in photon counting X-ray imaging because single X-ray photon counting can not only enable low noise, low dose X-ray imaging, but allows for optimal energy weighting and discrimination of the incident photons. Energy discrimination can help differentiate tissue of different densities in a more accurate manner, e.g., differentiating soft tissue and calcifications for more accurate breast cancer diagnosis. Although photon counting imagers require more complex pixel readout circuits, the

fundamental limitation is the X-ray photoconductor. Today, photon counting imagers are exclusively made using crystalline or polycrystalline materials such as silicon and CZT which are not large area compatible. The ideal photoconductor for photon counting should possess properties such as: 1) room temperature operation, 2) high resistivity and low leakage, 3) high conversion gain to enable single photon detection, and 4) fast operation for higher count rate. A-Se can be a candidate for the photon counting because of its relatively high sensitivity, room temperature operation and high bandgap of 2.2 eV which yields the lowest dark current of any commercial photoconductor today. Most importantly, a-Se can be evaporated over a large area as a thick film with respectively lower manufacturing costs. However, a-Se has been ruled out as a feasible radiation imaging photoconductor for dynamic imaging applications due to its low temporal resolution. Despite the considerable progress made in materials development, the charge transport properties of a-Se are not optimal for photon counting mode. While the collection efficiency of holes is generally quite adequate in a-Se, the collection efficiency of electrons is invariably much worse. The mobility lifetime product for electrons is typically an order of magnitude less than those for the holes. Also, given that the photon interaction occurs at a random location in the detector volume, the generated electrons drift across the variable range to the collecting electrode. This results in variable signal rise time due to electrons with slower mobility, and creates depth dependent noise.

1.6 Objective

In this research, given the preceding limitation of the a-Se photoconductor, we explore the causes of poor temporal response in the a-Se photoconductor for real-time dynamic and photon counting X-ray imaging applications using lag, ghosting and pulse height spectroscopy (PHS) measurements on conventional a-Se detectors. The measured data is compared to alternative a-Se imaging device architectures for improved dynamic imaging performance. The alternative device architectures include: (1) use of a polyimide blocking

layer that permits the operation of a-Se devices with higher electric fields, (2) a high field capable solid-state unipolar charge sensing device, and (3) small pixel geometries to obtain the small pixel effect (SPE).

First, we investigate the electrical conduction mechanism in the polyimide (PI) hole blocking layer to successfully suppress the dark current related noise. Once the lag originated from the cumulative charge injection from the positively biased contact is eliminated, the remaining lag is accounted for by the intrinsic properties of the a-Se photoconductor. The electrical properties of PI are investigated to properly limit the charge injection, and thus ensure that the measured lag is due to the intrinsic properties of a-Se only. Limiting dark current plays a critical role in revealing intrinsic properties of a-Se.

Next, we investigate the intrinsic temporal response through lag and ghosting measurements of conventional a-Se detectors. We also investigate the intrinsic energy resolution of a-Se for photon counting imaging using a characterization method common in high energy physics called pulse-height spectroscopy (PHS). Although the method itself has been discussed in literature, benchtop PHS systems have been used to characterize higher gain, faster crystalline and polycrystalline photoconductors. To characterize a-Se, the PHS experimental setup needs to be optimized for a lower gain and slower response. A PHS system must be set up to investigate single photon detection and the photon counting capability of a-Se with common radiation sources such as ^{241}Am and ^{57}Co gamma-ray sources. Critical to its feasibility for photon counting mammography and other photon counting applications, we must determine the intrinsic energy resolution and the maximum limit to the photon counting rate for a-Se.

Once the conventional a-Se detectors are characterized with lag and PHS measurements, we examine alternative device architectures to improve the temporal response both for the integration mode and photon-counting applications. The alternative device architectures achieve a unipolar charge sensing with the carrier types having a higher mobility-lifetime product (i.e., holes for a-Se) by establishing a strong near field effect in the proximity of the collecting electrode. We fabricated a solid-state unipolar charge sensing device similar to

Charpaks multi-wire proportional chamber invented for gaseous detectors in terms of the operation principle. The same characterization methods used for conventional detectors will be utilized for this unipolar charge sensing device and the results will be compared.

At the conclusion of this research, we demonstrate the photon counting capability of the a-Se photoconductor combined with the CMOS detector. The detector features $11 \times 11 - \mu\text{m}^2$ pixels to overcome a-Se count-rate limitations by unipolar charge sensing of the faster charge carriers (holes) via a unique pixel geometry that leverages the SPE for the first time in an amorphous semiconductor. Measured results from a mono-energetic radioactive source are presented and demonstrate the untapped potential of using amorphous semiconductors for high-spatial-resolution photon-counting X-ray imaging applications.

This research suggests that the well-established large-area a-Se photoconductor incorporating with unipolar charge sensing can meet the requirements of emerging medical imaging applications such as photon-counting mammography or micro-angiography without resorting to new sensor materials or crystalline semiconductors that are challenging to scale up to larger areas.

1.7 Thesis organization

The primary focus of this thesis is the development of a-Se X-ray imaging detector with an improved dynamic imaging performance. The thesis chapters are organized as follows:

- Chapter-2 provides performance metrics of digital X-ray imaging systems such as sensitivity, dark current, noise, dynamic range and memory effects in direct conversion FPDs. It also investigates the different mechanisms responsible for the carrier transport in amorphous solids, including a-Se.
- Chapter-3 demonstrates the use of PHS measurements to extract the internal electric field of an a-Se detector with a PI blocking layer. The hole conduction mechanism

incorporating with Poole-Frankle effect is investigated for the optimum dark current performance of a-Se radiation detectors.

- Chapter-4 presents detailed modeling on charge induction, signal rise-time and charge collection efficiency for both conventional and unipolar charge sensing detectors via the analytical models and the simulation studies. Energy resolution of a conventional a-Se detector is investigated through Monte-Carlo simulation model and the impact of hole trapping on the detector temporal and energy resolutions are demonstrated.
- Chapter-5 presents the design and fabrication of the unipolar charge sensing device architecture for mitigating the poor temporal resolution problem of a-Se radiation detectors. Series of experiments to demonstrate and improve the imaging abilities of a-Se detectors for dual-energy mammography and fluoroscopy are described. Then, energy and timing resolutions of the unipolar charge sensing detector are evaluated with a very low-noise pulse-height spectroscopy and photocurrent lag measurement systems, respectively.
- Chapter-6 reports the results from a single photon-counting X-ray detector monolithically integrated with an a-Se photoconductor. The detector features $11 \times 11 - \text{mm}^2$ pixels to overcome a-Se count-rate limitations by unipolar charge sensing of the faster charge carriers (holes) via a unique pixel geometry that leverages the small pixel effect employed in the photoconductors suffering from a poor charge collection problems.
- Chapter-7 concludes the thesis. A summary of contributions is presented along with recommendations for future work.

Chapter 2

Metrics of Detector Performance

2.1 Introduction

The X-ray detector should be designed and optimized to administer the lowest patient dose that produces an image quality adequate for diagnosis and intervention. The overall detector performance is typically defined by a linear cascade model to investigate signal and noise transfer as a function of spatial frequency. Photoconductors for X-ray imaging are selected based on a variety of criteria including sensitivity, dark current and charge transport properties. The performance of a read-out circuit is also characteristic of the overall performance of the detector. Therefore, the intrinsic properties of the photoconductor together with the performance of the read-out circuitry determine the required patient dose.

In this chapter, some of the evaluation metrics for X-ray detector performance at zero spatial frequency, which are mostly related to implemented device structures in this thesis, are introduced in the following sections. Some theories and concepts which are required to understand the imaging characteristics of the X-ray imaging systems are also introduced. Due to the scope of this thesis, the detailed performance analysis of the full panel detector containing read-out circuit contribution is not discussed in detail as a function of a spatial

frequency. For the cascaded imaging system analysis with the Fourier-based metrics, the reader is referred to [62, 63, 64, 65, 66].

2.2 X-ray interactions in photoconductors

In the hard X-ray energy regime of 10-120 keV used for medical X-ray imaging, X-rays interact with a matter by scattering, penetration or absorption. The types of interactions are Rayleigh and Compton scattering, and photoelectric effect. The mechanisms of absorption and scattering through photoelectric effect and Compton scattering, respectively, cause the attenuation of the X-ray photons and thus result in loss in the strength of the X-ray beam. However, Rayleigh scattering is an elastic (coherent) scattering of X-ray photons by atomic electrons where there is no exchange of energy from X-ray photons to the photoconductor. The photon interaction through Rayleigh scattering does not result in a local deposition of energy in the medium, and both incoming and scattered photons energies are identical.

Both photoelectric effect and Compton scattering contribute to the absorption of energy in the photoconductor. Compton scattering is inelastic scattering and is typically observed when the incoming photon energy is higher than the binding energy of the atomic electron. The outcomes of this interaction are the quasi-free electron with some kinetic energy E'' , an ionized atom, and the scattered X-ray photon with energy E' left after the imparted energy to the electron. The Compton scattering process is illustrated in Fig. 2.1(a). Note that the imparted energy depends on the scattering angle which is random in nature. The Compton scattering cross-section nearly occurs independent to the energy of the photon, E , and the atomic number of the photoconductor, Z . However, photoelectric interaction cross-section is proportional to Z^3/E^3 [67].

The interaction through the photoelectric effect, however, results in a total energy transfer of the X-ray photon into the photoconductor. Part of the energy is used to overcome the electron binding energy, and the remaining energy is converted to the kinetic energy of the free electron. The photoelectric process is illustrated in Fig. 2.1(b). Photoconductors

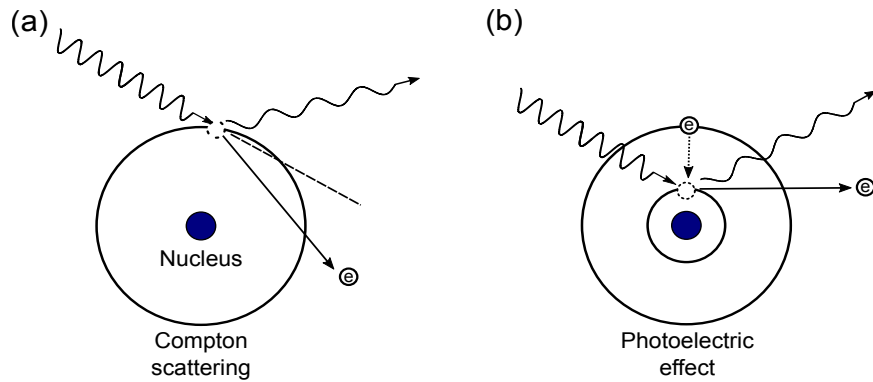


Figure 2.1: a) In Compton scattering, an incident X-ray interacts with an outer-shell electron, and creates an electron of kinetic energy E'' , an ionized atom, and a scattered X-ray photon of energy E' , b) in the photoelectric effect, the energy of an incident X-ray is fully absorbed by an electron, which is ejected from the atom causing ionization. An electron from the outer shell fills the vacancy in the inner shell, which creates a fluorescent X-ray [6].

with high Z such as a-Se ($Z=34$) attenuate hard X-ray energies through photoelectric interaction. Photoelectric interaction occurs depending on the energy of the incident photon, and the energy of the shell in which the corresponding electron is bound. For instance, if the photon energy is not enough to eject an electron from the K-shell (the inner most shell with a higher electron binding energy), then an electron on the outer-shell (L shell, M shell and so on) can be ejected. When the electron is ejected from the inner shell, a cascade electron transition process is initiated. This transition process creates characteristic X-rays (K-fluorescent, L-fluorescent, etc.) which are absorbed by either the same or neighbouring pixels, depending on the energy. The escaped characteristic X-ray photon also causes incomplete energy transfer. This degrades detector sensitivity [68]. The energy of the characteristic X-ray is one of the intrinsic properties of the photoconductor. For this reason, it is desirable to have a photoconductor with a lower characteristic X-ray energy to maintain adequate spatial resolution and sensitivity [69]. For example, the energy of the K-fluorescent photon in a-Se is 12.66 keV which is absorbed in a practical photoconductor

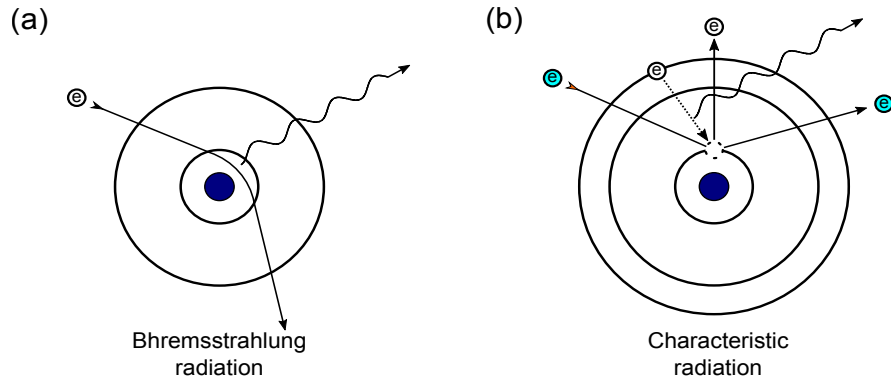


Figure 2.2: a) Bremsstrahlung radiation is produced when energetic electrons are decelerated by the electric field of target nuclei, b) if an electron is liberated from an inner core shell, there exists a vacancy in its parent atom. A cascade of electron transitions can occur, which can produce one or more characteristic X-rays.

thickness, and thus does not degrade spatial resolution and sensitivity appreciably. The ejected electron, also called the secondary electron, leads ionization along its trajectory and creates electron-hole pairs. Furthermore, the secondary electron interacts with the nucleus and orbits of the atoms along its track through Coulomb interaction and loses part of its energy. The loss of this energy is converted to bremsstrahlung radiation. The formation of characteristics and bremsstrahlung radiation are illustrated in Fig. 2.2.

2.3 Charge transport in amorphous semiconductors

In contrast to crystalline semiconductors with well-defined charge conduction mechanisms via well-defined energy bands, a charge transport in amorphous semiconductors can be complicated due to the distribution of disorder-induced localized states. Referring to the Mott Model with Density of States (DoS) in amorphous semiconductors (shown in Fig. 2.3), three main types of charge transport mechanisms exist [7, 70]. Carriers with energy higher than E_c can be excited to the extended electronic states, where the carrier conduction is

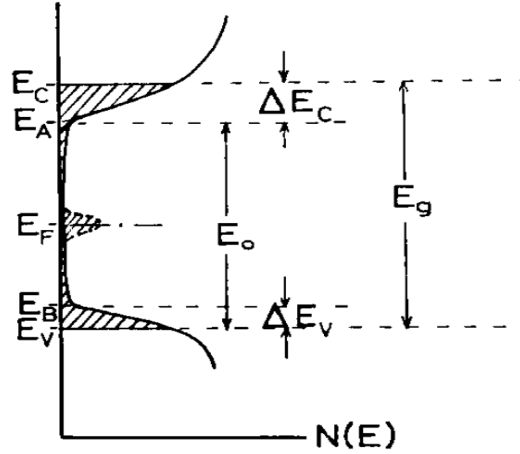


Figure 2.3: Density-of-states in amorphous semiconductors as proposed by Mott. Localized states are shaded and E_c and E_v refer to the mobility edges for the conduction and the valence bands, respectively. Reprinted from [7] with permission granted.

like that of the electrons in the conduction band of crystalline semiconductors. The charge transport occurs based on Bloch wave function because the Schubwegs of the carriers in these states is much longer than the interatomic distance. Roughly, the mobility of the carriers in these states is higher than $100 \text{ cm}^2/\text{V.s}$ [9]. When the carriers are excited to extended states just above the mobility edge with a high density of localized states, Schubwegs of the carriers become comparable to the interatomic distance. Thus, the conduction mechanism can not be considered as a simple band transport. The motion of the charge carriers can be described with Brownian motion. In this case, the predicted mobility of the carriers is in the order of $1 \text{ cm}^2/\text{V.s}$ [9]. However, in the localized states below E_c at room temperature, Bloch wave function does not extend. The carriers may hop to localized states through tunneling near the Fermi level. Spear explained the mobility for *activated hopping* transport by the equation below [71]:

$$\mu = \frac{eR^2}{kT} V_{PH} \exp[-2\alpha R] \exp\left[-\frac{W}{kT}\right], \quad (2.1)$$

where R is the average hopping distance, V_{PH} is the hop frequency, and W is the activation energy. Here, $\exp[-2\alpha R]$ describes the overlap of the wavefunction on the neighbouring hopping states. The corresponding carrier mobility due to the activated hopping mechanism can be in the order of $10E-2 \text{ cm}^2/V.s$

Hopping transport is typically the main conduction mechanism for charge transport in a-Se [72]. The microscopic mobility in a-Se can be modulated by traps that are present at the lower energy level with respect to the microscopic conduction level. The drift mobility of carriers in a-Se is the effective mobility which is defined by the capture and release of the carriers in the shallow trapping states. The mobility is based on the time that carriers spend on the trapping center. It is modified by a factor of $t_c/(t_c + t_r)$, where t_c is the amount of time that the carrier is free, and t_r is the amount of time that the carrier stays in the trap states.

The carriers captured by the trap states can be re-emitted from the traps by either a thermally activated process or applied electric field. The release time of the carriers due to the thermal activation process follows Boltzmann statistics and is given in the equation below [9]:

$$\frac{1}{\tau_R} = V_{PH} \exp\left[-\frac{E_T}{kT}\right], \quad (2.2)$$

where τ_R is the mean release time, V_{PH} is a phonon frequency, and E_T is the depth of the trap below the band edge. The detailed balance considerations relate to the trapping and de-trapping time when the hopping transport is applicable. It is given by:

$$\frac{\tau_C}{\tau_R} = \frac{N_C}{N_T} \exp\left[-\frac{E_T}{kT}\right], \quad (2.3)$$

where N_C is the density of states in the conduction band.

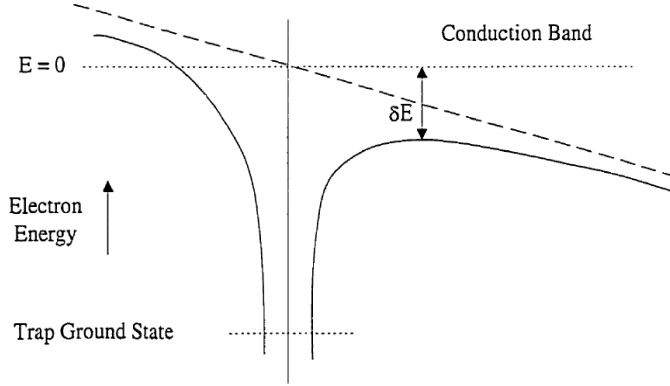


Figure 2.4: Energy diagram for an electron bound to a point charge in the presence of a uniform electric field (Poole-Frenkel effect) [8, 9, 10].

Furthermore, the application of an electric field lowers the potential barrier, E_T , through the Poole-Frenkel effect and enhances the release of the trapped charges, as shown in Fig. 2.4 [8]. The amount of the barrier decrease is given by:

$$\delta E = \beta\sqrt{E}, \quad (2.4)$$

where β is the Poole-Frenkel constant and E is the applied electric field. The above equation for release time estimation should be modified when the applied electric field exists as below:

$$\frac{1}{\tau_R} = V_{PH} \exp\left[-\frac{E_T - \beta\sqrt{E}}{kT}\right]. \quad (2.5)$$

2.3.1 Time-of-flight technique

The well-established method to measure the charge transport properties of highly resistive disordered solids such as a-Se is the time-of-flight (TOF) transient photoconductivity experiment [73, 74]. A typical TOF experimental setup used for the measurements of charge

transport properties of a-Se is shown in Fig. 2.5. Using a short laser pulse (e.g., typically a few hundreds of picoseconds), such a device consisting of a-Se, for instance, is illuminated from the side that contains the transparent electrode to create a narrow sheet of charge. Given that the transport of carriers in a-Se is non-dispersive [75, 76], the width of the charge sheet does not broaden during its drift along a-Se thickness under the applied electric field. The drift of the carriers is thus time-resolved and captured on an oscilloscope. After this, the mobility can be estimated based on the equation below:

$$\mu = \frac{L^2}{t_T V}, \quad (2.6)$$

where L is the thickness of a-Se, and V is the applied voltage. Note that the intensity of the laser should be relatively low and an excessive charge injection from the contact metals should be prevented to maintain the small signal condition. The lifetime of the carriers can also be measured by using the TOF measurement method. Table 2.1 summarizes the charge transport properties of the un-doped and stabilized a-Se obtained using TOF measurement technique. The charge transport properties in a-Se change significantly with doping and fabrication conditions, as seen in Table 2.1, where a wide range of values has been reported. In this thesis, we also carried out TOF measurements to ensure the quality of the samples used for unipolar charge sensing devices, in which the temporal response is particularly dependent on hole mobility.

2.4 Performance metrics of digital X-ray detectors

There are several metrics used to describe and compare the performance of X-ray imaging systems. The most important characteristics of the X-ray imaging systems involve sensitivity and image resolution of the detector. Moreover, digital detectors have some intrinsic issues that do not apply to the analog imaging systems such as dark current. For instance, an imaging system's dose efficiency is characteristic of its overall performance

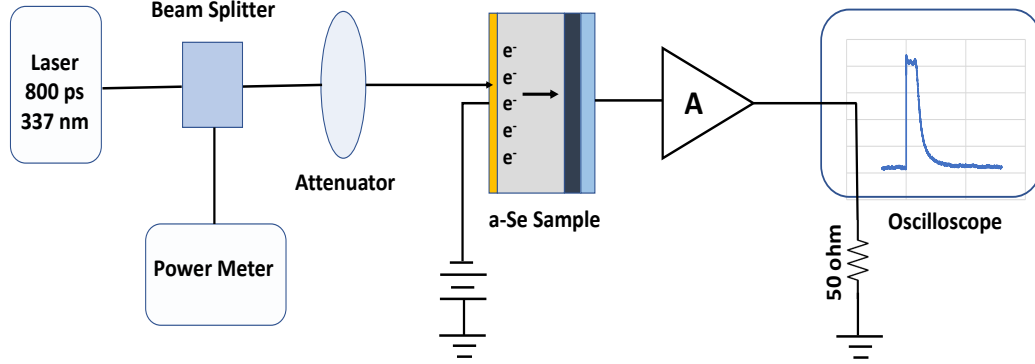


Figure 2.5: Schematic of time-of-flight experimental setup used for the charge transport measurements in a-Se device.

Table 2.1: Selected properties of un-doped and stabilized a-Se photoconductor. a= Un-doped a-Se, b= stabilized a-Se [3]

Property	Value	Comment
E_g (eV)	2.0	Optical transmission through thin films.
E_g (eV)	2.1-2.2	Electrical and xerographic measurements.
μh ($cm^2 V^{-1} s^{-1}$)	$0.13 - 0.14^{a,b}$	Very reproducible, independent of thickness and source of a-Se. Thermally activated.
τ_h (μs)	$10 - 100^a$ $50 - 500^b$	Good quality film. Depends on the substrate temperature, impurities and Se processing.
μe ($cm^2 V^{-1} s^{-1}$)	57×10^{-3a} $2 - 4 \times 10^{-3b}$	Slightly field dependent and depends on the source of a-Se and As content. Thermally activated.
τ_e (μs)	$10 - 100^a$ $200 - 1000^b$	Depends on impurities and Se processing. Independent of the substrate temperature. Increases with As content.
σ_{dc} ($(\Omega cm)^{-1}$)	$10^{-17} - 10^{-14}$	Dark conductivity is thermally activated. Very sensitive to impurities. 10^{17} is for deoxygenated sample.

which is defined by the cascade relationship between the input and the output of the system. Therefore, it is critical to understand the contributions of all the stages of the imaging system on the quality of the output signal. In this section, we briefly explain these metrics related to the explored device structures and their applications in this thesis. Note that there are some other important metrics used for image evaluation not explained here, such as modulation transfer function, noise power spectrum etc. The interested readers can investigate more by consulting the references [22, 44, 77, 78, 79, 80, 81].

2.4.1 Sensitivity

Photoconductor sensitivity is a measure of average conversion efficiency of incident X-ray photons to the charge integrated on the pixel storage capacitance. The higher the sensitivity of the detector, the lower the patient dose is required to obtain an X-ray image with a reasonable quality. The X-ray sensitivity of an imaging detector is given by the amount of the collected charge per unit area per unit exposure of incident radiation:

$$S = \frac{Q}{AX}, \quad (2.7)$$

where Q is the collected charge in Coulomb (C), A is the area of the radiation receiving side of the detector in cm^2 , and X is the radiation exposure in Roentgen (R). Then the unit of the sensitivity is $\text{C}/\text{cm}^2\cdot\text{R}$.

The sensitivity of the x-ray detector depends on three distinct stages: 1) photon absorption in a photoconductor, 2) conversion of the absorbed photons to free EHPs (the required energy is defined as the ionization energy), 3) and the fraction of the collected charge. The fraction of the X-ray photons attenuated in the photoconductor is defined by the term quantum efficiency, η , which is mainly based on the linear attenuation coefficient, $\alpha(e)$, and the thickness of the photoconductor, L , that X-ray photons traverse. η of a photoconductor is given by:

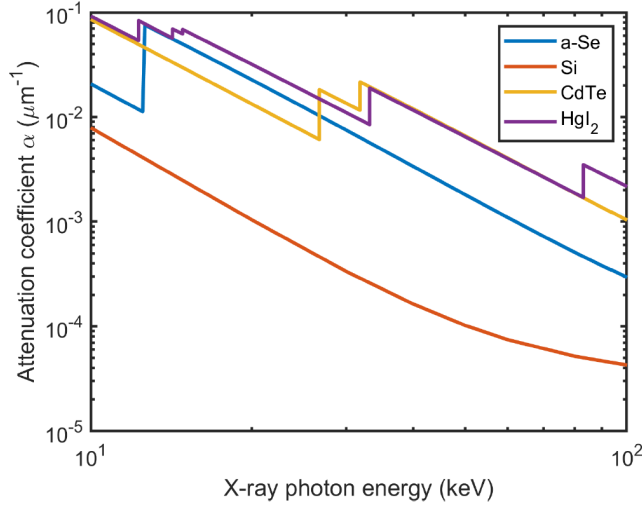


Figure 2.6: Comparison of x-ray attenuation coefficients for Si ($Z = 14$), CdTe ($Z = 48$; 52), HgI_2 ($Z = 80$; 53), and a-Se ($Z = 34$). Generated using [11]

$$\eta(E) = 1 - e^{-\alpha(E)L}, \quad (2.8)$$

where $\eta(E)$ varies between 0-1. To achieve higher quantum efficiency, a photoconductor thickness should be much larger than the attenuation depth (*i.e.*, $L \gg \alpha^{-1}$). Note that α depends on the atomic number (Z) and the density of the photoconductor, and the energy of X-ray photons. Therefore, higher Z is desirable for higher X-ray attenuation. For instance, mean X-ray energy used for mammography is 20 keV, and the required a-Se thickness for such imaging procedures is around 200 μm to sufficiently absorb most of the incoming X-ray photons. However, the thickness of a-Se should be close to 2000 μm to be used for a chest radiography examination where the mean X-ray energy is 60 keV. The attenuation coefficients as a function of X-ray photon energy for several direct conversion photoconductors are shown in Fig 2.6. Higher Z polycrystalline photoconductors (e.g., CdTe) have a superior quantum efficiency compared to a-Se. However, the sensitivity for these materials is highly degraded due to incomplete charge collection which is also the main

limitation with a-Se. The research in this thesis is mainly concerned with incomplete charge collection problems. Although the results are obtained from the a-Se based detectors, the proposed device structure can be utilized for polycrystalline photoconductors as long as the limitations with the current fabrication procedures are overcome. The amount of the required photon energy to create a single free electron-hole pair (EHP) is called the EHP creation energy, or the ionization energy, W_{\pm} . Generally, EHP creation energy depends on the band-gap energy, E_g , of the photoconductor for most of the semiconductors, and is expected to follow Klein's rule [82]:

$$W_{\pm} \sim 2.8E_g + E_{phonon}. \quad (2.9)$$

This rule is very suitable to most of the crystalline semiconductors such as high purity Si, which has been used for most of the photon-counting detectors to measure incident photon energies (i.e., energy-binning) with a high energy resolution. However, there are some exception photoconductors which do not follow the rule. For instance, W_{\pm} is less than that estimated by Klein's rule for HgI_2 and PbI_2 , where the EHP creation energy is dependent on the applied electric field.

The energy required to create a EHP in a-Se is also quite higher than the estimated value by Klein's rule. The root of the problem is that some of the EHP recombine before they separate into free electrons and holes due to the disordered nature of a-Se with lots of defect states. Previous studies have shown that EHP creation energy in a-Se depends on the incident photon energy (either optical or high energy photon), applied electric field and temperature through a series of measurement techniques such as xerographic discharge or pulse-height spectroscopy [83, 13].

In the final stage of photon-to-charge conversion, the sensitivity of the photoconductor is defined by its charge collection efficiency, which depends on the relative magnitude of the carrier Schubwegs, $\mu\tau E$, with respect to the photoconductor thickness, L . The charge collection efficiency, η , under applied electric field, E , is governed by the well-known Hecht equation [84, 85]:

$$\eta_{collection} = \frac{\mu\tau E}{L} [1 - \exp(-\frac{L}{\mu\tau E})], \quad (2.10)$$

where η converges to unity when a sufficiently high electric field is applied and converges to zero as the electric field is close to zero. For instance, the limited sensitivity with a-Se due to Schubweg limited charge collection efficiency is one of the reason that a-Se has been ruled out as a viable photoconductor that can be used for photon-counting imaging today. One of the criteria that an ideal photoconductor should possess is that the dark current should be negligibly small to achieve higher dynamic range. The requirement of a higher applied field for a-Se operation, however, increases the dark current level due to the increased charge injection, which leads to lower X-ray sensitivity. Also, a photoconductor should have a wide bandgap to have negligible dark current, which also degrades the sensitivity. Therefore, there is an inevitable compromise between achieving lower dark current and higher X-ray sensitivity in most of the photoconductors.

2.4.2 Dark current

For direct conversion detectors, thermal generation of charge carriers and application of electric field for achieving an efficient charge separation lead current flow even in the absence of any radiation (i.e., dark conductivity). Such current is known as a dark current. The dark current introduces noise into the detector by accumulating charge on a pixel storage capacitor and limits the smallest amount of X-ray radiation that can be detected.

For a-Se, thermally generated charge carriers in the bulk are negligible due to the large mobility gap (2.2 eV). Because a high electric field is required to operate a-Se detectors due to the field dependent photogeneration and charge collection efficiencies, the dominant source of dark current is the injection of charge carriers from the electrodes [86]. Although dark current in a-Se has been studied extensively after a-Se was started to be employed for FPDs, the dark current behaviour has not been fully understood. The main

conclusion, however, is that the surface of the a-Se layer and properties of the junction between the metal contacts and a-Se have profound effects on the observed dark current level. Also, imperfection in the film fabrication conditions and complicated measurement procedures due to the existence of non-steady state current introduce some complexity when identifying the main mechanism responsible for dark current behaviour [86, 87, 88]. For example, Johanson and coworkers studied the effect of different contact metals on the I-V characteristics of a-Se. It was expected that Schottky contact can be established since the work function of a-Se (i.e., 5.9 eV) is larger than the work function of all the metals. However, no correlation has been observed between the metal type and dark current, which again implies that the dark current mechanism in a-Se can not be explained with simple I-V measurements. Previous studies on the dark current behaviour of a-Se interpreted the charge injection through one of the following mechanisms:

- Space-charge-limited-current (SCLC). It was reported that steady-state photogenerated current follows the SCLC mechanism with $J \propto (V^2/L^3)$ when the device is illuminated from one metal contact side or $J \propto (V^3/L^5)$ when illuminated from both sides, both types of carriers' injection dominate. Note that J is a current density and L is the thickness of the a-Se layer [89].
- Tunneling of carriers from the metal electrodes to the a-Se layer. The tunneling is explained by the Fowler-Nordheim (FN) tunneling mechanism [90].
- Hopping of charges from the metal Fermi level into the localized states in a-Se, following the electric field-activated hopping injection model as explained in the charge transport section [75].

Dark current in a-Se can be suppressed significantly by adding a blocking layer between electrodes and photoconductor layers. A proper blocking layer should have a high potential barrier, high trap density and very low mobility for one of the carrier types while it facilitates the collection of the other type of carrier. Thus, a blocking layer acts as either

a hole or an electron blocking layer. It has been reported that the hole injection from the positively biased electrode of a-Se detectors is the dominant source of dark current. Recently, Abbszadeh reported that the Polyimide (PI) hole blocking layer successfully limits excessive hole injection from the positively biased electrode and prevents photo-induced darkening and crystallization [91, 92, 52]. In this thesis, we further investigate the electrical conduction mechanism in the PI layer to more efficiently mitigate charge injection, and enhance the temporal resolution of a-Se detectors for high frame rate imaging application.

2.4.3 Noise

An ideal X-ray imaging system is fundamentally limited with a quantum noise which is originated from the quantum nature of the X-ray beam in which photons are distributed in a random pattern. Assuming that the fluctuation in the X-ray intensity follows Poisson statistics and the mean of the total number of absorbed X-ray photons by a detector is given by N , the standard deviation is estimated as $N^{1/2}$. This system is known as a quantum-noise limited system with a signal-to-noise ratio of $N^{1/2}$. Note that quantum noise can be reduced at the expense of increased radiation dose, or vice versa, the radiation dose can be decreased at the expense of reduced visibility. In fact, most x-ray imaging procedures are conducted at a point of reasonable compromise between acceptable visibility and lowest possible noise level.

Today, most of the deployed X-ray imaging systems work with an energy integration mode, which is susceptible to noise related to both the photoconductor and readout circuit. The main contributors of photoconductor intrinsic noise are Swank and leakage-shot noises. Swank noise originates from the fluctuation of the EHP creation energy due to the ionization process and charge carrier recombination and trapping. Swank noise is also known as gain fluctuation noise. The ideal detector system has a Swank factor of 1 [93]. The origin of the leakage shot noise is the dark current that is caused by mainly charge injection from the contacts as explained in the previous section. The leakage shot noise, N_d , for an energy integrating systems is given by:

$$N_d = \sqrt{\frac{J_d A T_f}{e}}, \quad (2.11)$$

where J_d is the dark current density of a-Se, A is the area of the pixel, T_f is time between successive readout, and e is the charge of an electron (1.6E-19 C). For instance, for a 5pA/mm² given dark current density, 150 μ m pixel pitch and 60 ms of readout time, the leakage shot noise is calculated around 250 e^- .

Considering PPS readout architecture, the total noise components are the thermal and flicker noise of the on-pixel TFT switch, the thermal noise of the column charge amplifier and the analog-to-digital converter (ADC) noise. Today, most of the FPDs, either indirect (CsI-PIN diode) or direct conversion (a-Se based), are integrated with PPS readout architecture due to its compatibility to large areas required for X-ray imaging. However, PPS architecture is inherently limited with column charge amplifier noise, that significantly reduces the dynamic range, especially for low dose imaging applications such as fluoroscopy. For instance, the total input-referred noise of an indirect FPD is reported around 1500 e^- for 80 μ m pixel pitch [94].

Single photon counting (SPC) X-ray detectors, on the other hand, provide energy discrimination for improved image contrast and offer the advantages of lower noise and higher dynamic range compared to traditional integration-mode X-ray detectors. The impact of the electronic noise on the output signal can be minimized by setting the low-level discriminator value properly, in a way that should neither reject the true events, nor cause significant beam hardening. SPC also enables improved dose efficiency and multi-energy imaging for enhanced contrast visualisation. Single photon counting (SPC) imagers used for mammography have shown significant dose reduction up to 40% while providing an image with a sufficient quality [95].

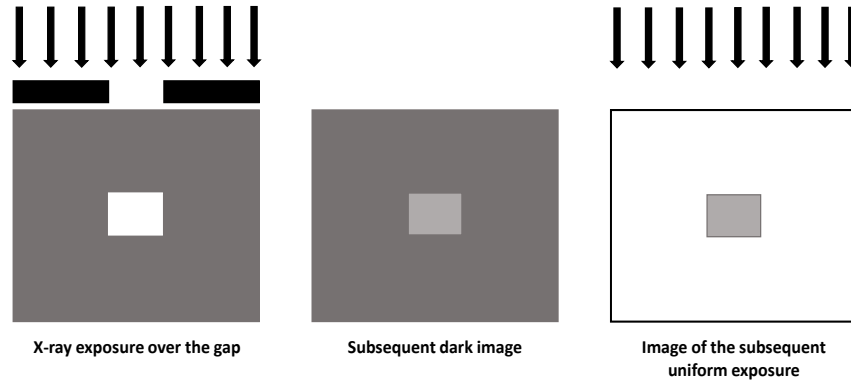


Figure 2.7: Images that demonstrate the appearance of lag and ghosting.

2.4.4 Temporal response

The temporal response of direct conversion photoconductors can be characterized by two important figures-of-merit, namely lag and ghosting. Lag is the spill-over of image charge into the subsequent image frame due to the thermal release of trapped charge. It gives rise to an increased dark conductivity after the cessation of X-ray pulse [96, 97]. Charge injection from the biased electrodes dramatically increases during the X-ray exposure and contributes to the image lag [97]. Ghosting can be described as a reduced detector sensitivity due to the recombination of the trapped charge with the photogenerated charge during the subsequent X-ray exposure. As illustrated in Fig. 2.7, lag results in increased pixel values in the previously exposed area, while ghosting manifests itself as reduced pixel values, and can only be measured on the subsequent X-ray images. The temporal response of a detector is more important for the high frame rate imaging applications such as fluoroscopy. Currently, the highest performance commercial FPDs are based on a-Se technology, but there is no a-Se commercial detector operating with a high frame rate because increased lag degrades the temporal response and makes a-Se detectors impractical for real time imaging today. Image lag is a common problem for most of the direct conversion photoconductors such as HgI_2 and PbO , and prevents the use of such materials for the commercial FPDs.

Nevertheless, it has been shown that ghosting is not significant in the clinical dose range, but it becomes a significant problem at higher doses.

2.5 Conclusion

The X-ray interaction mechanisms in a photoconductor and charge generation process are briefly described. It is indicated that the main charge generation mechanism in the medical imaging energy range (10-120 keV) is based on photoelectric effect. Some of the intrinsic effects, such as K-fluoresce escape, which cause the reduction in sensitivity and spatial resolution are also mentioned. The charge transport mechanism in an amorphous semiconductor, particularly for a-Se, is explained. It is also shown that the temporal response of X-ray imaging detectors is characterized by lag and ghosting. The limitations and advantages with the current energy integrating systems and single photon-counting (SPC) detectors are discussed. Two main drawbacks of the energy integrating system are that, first, they do not provide energy information of the detected photons that can be used to improve contrast resolution to discriminate especially soft tissues and second, they require a large patient dose to overcome this limitation. Both issues are addressed by SPC detectors. However, current SPC X-ray detector technology is limited to small-area imaging applications due to scaling constraints on both the X-ray sensor material and the readout integrated circuit (IC). Energy integrating systems are still very commonly employed for most of the imaging applications despite the limitations mentioned here because they offer some distinct advantages such as large area compatibility for a reasonable cost due to well-established TFT technology. In the following chapters, we propose a device structure for circumventing the problem of poor charge transport with a-Se to enable the design of single photon counting and energy integrating detectors, for spectral mammography and real-time fluoroscopy respectively (dynamic imaging operation). A-Se is already the predominant technology for large-area mammography X-ray detectors (static imaging operation) operated with energy integration mode.

Chapter 3

Device Structure to Achieve Low Dark Current Amorphous Selenium Radiation Detectors

3.1 Introduction

Direct conversion amorphous selenium (a-Se) based flat-panel detectors are a mature X-ray imaging technology and are used in mammography for their higher spatial resolution and quantum efficiency when compared to their indirect-conversion counterparts [3, 98, 44, 99, 100, 101, 69, 102]. Direct-conversion detectors typically require the application of a large electric field across the a-Se layer to achieve adequate separation and collection of X-ray generated charge [13, 103]. The large electric fields, however, can give rise to undesirable leakage current in the detector, which degrades signal-to-noise ratio, and can also cause persistent photocurrent lag [104, 97, 105]. These adverse effects are usually resolved by using a blocking contact layer between the contact metal and photoconductor [106, 30]. Recently, the use of an organic polyimide (PI) blocking layer with a-Se detectors has been reported and shown to successfully limit excessive hole injection from the positive electrode

to the bulk while simultaneously preventing photo-induced darkening and temperature and stress induced crystallization [92, 16, 107].

Despite these successful demonstrations, the mechanism of hole transport through the PI layer is still not well understood. A better understanding of this phenomenon could aid in the development of new a-Se detectors featuring improved long-term stability and X-ray-dose efficiency. Previous investigations hypothesized that hole conduction mechanism in the PI layer could be explained by the presence of space charge-limited currents (SCLC) or Fowler-Nordheim tunneling [108, 109]. The controversy arises because the local electric field within both a-Se and PI layers influences charge conduction and determining the magnitude of this local electric field has not been accomplished accurately to date using direct methods. In the past, the local electric field was obtained indirectly via time-of-flight (TOF) measurements [110]. However, this method provides limited accuracy because the hole mobility, which is non-linearly dependent on the effective electric field, must be determined.

In this chapter, we demonstrate, for the first time, the use of pulse-height spectroscopy (PHS) to extract the internal electric field of an a-Se photoconductor having a PI blocking layer. PHS is traditionally used to determine the ionization energy of radiation sensitive semiconductors for a given incident photon energy by accurately measuring the number of charge carriers generated by a single photon [111]. These ionization energy measurements are then used to obtain the energy resolution of gamma radiation detectors[112, 113]. Since the ionization energy is inversely related to the internal electric field, PHS could offer an opportunity to directly measure this field. Furthermore, PHS could provide more accurate internal electric field measurements compared to existing techniques because minor single photon interactions for radiation detectors are not expected to distort the internal electric field in any substantial manner.

The chapter is organized as follows. In the next section, we introduce the fabricated device structure and the experimental setups used for measurements. In Section 3.3, we demonstrate the use of PHS to extract an internal electric field in a-Se and PI layers. We

Table 3.1: Spin-coating and curing parameter of the PI layer.

Spin-coating polyimide	Parameter		Curing	Parameter
Initial spin-speed (RPM)	500	500	Initial temperature ($^{\circ}C$)	20
Initial spin-time (sec)	7	7	Temperature ramp-rate ($^{\circ}C$)	4
Final spin-time (RPM)	5000	3000	Final temperature ($^{\circ}C$)	340
Final spin-time (sec)	35	35	Total cure time (hours)	2
Approximate thickness (μm)	1	2	Cooling time (hours)	4

also report I-V measurement results in the dark and under X-ray illumination from several devices featuring a constant a-Se layer thickness, but a varying PI layer thicknesses. In Section 3.4, we verify our experimental results using a model that incorporates the Poole-Frankel emission model.

3.2 Method and materials

3.2.1 Device fabrication

A total of three a-Se detectors are fabricated with a variable PI layer thickness. A schematic of the sample structure is shown in Fig. 3.1. PI hole blocking layers are spin coated onto indium-tin-oxide (ITO) covered glass substrates, which are used as bottom electrode. The thickness of the PI layers is defined by the speed of spinning and the duration of the curing process. HD-MicroSystem offers wide range of PI solutions with a different viscosity. In this study, we used PI-2610 and PI-2611 to obtained PI layers with a thickness of 0.8 μm 1.8 μm and 3 μm , respectively. The detailed process parameters used for spin-coating and curing of PI layers are shown in Table 3.1. For all the samples, a 75- μm thick layer of stabilized a-Se alloy is thermally evaporated on top of the PI layers, which is followed by evaporation of an Au top contact having an effective area of 1 mm x 1 mm. The thickness of a-Se is optimized to achieve a compromise between maximum photon absorption rate

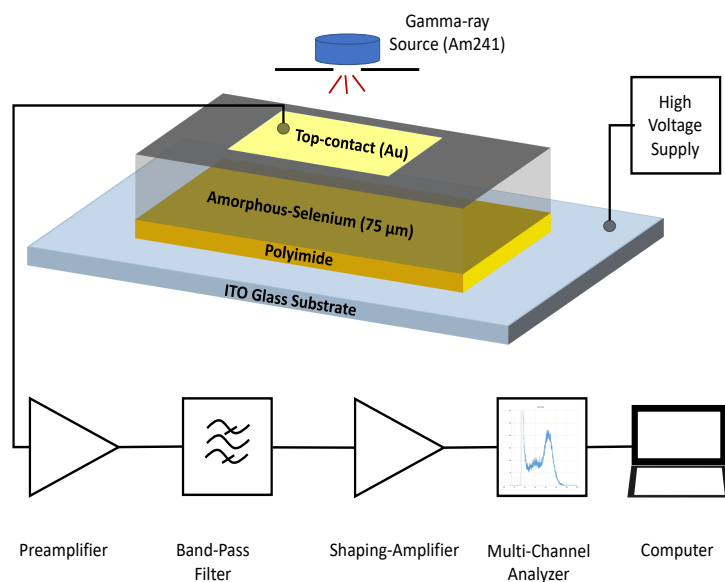


Figure 3.1: a) Schematic of the fabricated PI/a-Se detectors and PHS experimental setup. The feedback circuit of the preamplifier (A250CF) is optimized for a lower gain and a slower response of a-Se. Three different samples are fabricated with a various PI thickness ($0.8 \mu\text{m}$, $1.8 \mu\text{m}$ and $3 \mu\text{m}$).

for the energy of the gamma-ray source (^{241}Am , 59.4 keV) used for PHS experiments and the noise level of the PHS system, which increases significantly as the applied voltage to the sample increases.

Any contamination on the glass substrates (e.g., oil and dust particles) may cause long/short-term stability problem with an a-Se film, for instance crystallization, which alters the electrical properties substantially. To avoid this potential problem, all the ITO covered glass substrates were cleaned using ultrasonic bath just before loading them to a-Se evaporator, following the procedure below:

- Wash substrates in acetone in the ultrasonic bath for 10 minutes
- Wash substrates in iso-propanol in the ultrasonic bath for 10 minutes

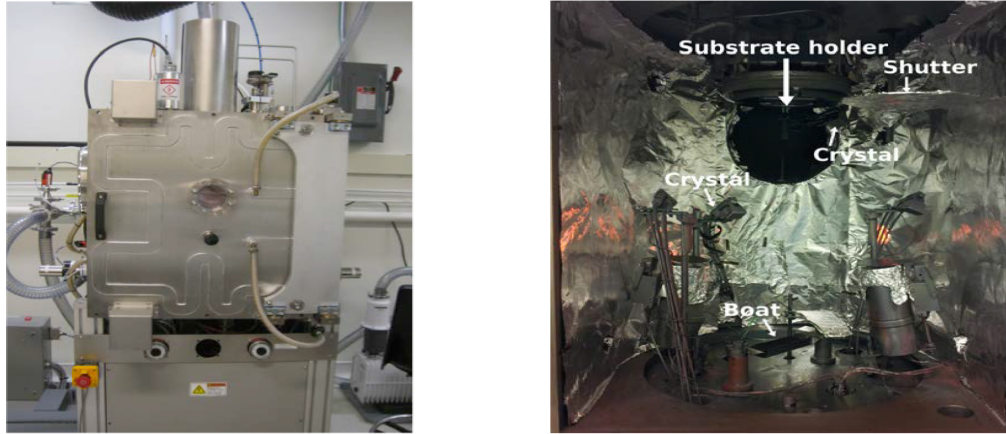


Figure 3.2: Selenium evaporator in G2N lab (left); the evaporation assembly inside the vacuum chamber (right).

- Rinse substrates with de-ionized water
- Blow dry substrates using nitrogen flow

The deposition of an a-Se film onto the PI covered ITO glass substrates was performed using thermal evaporation system under high vacuum. The dedicated vacuum chamber was installed at the Giga-to-Nano Electronic Center (G2N), University of Waterloo, and shown in Fig. 3.2. The system has a molybdenum evaporation boat and a rotating substrate holder that provides a uniform film due to its constant rotation rate. A deposition of an a-Se film onto the substrate is prevented by two shutters, one above the evaporation boat and one below the substrate holder, until the desired evaporation rate and stability are achieved. A rough thickness of the evaporated film on the substrate is estimated by the combination of quartz crystal reading and tooling factor that we investigated after several trial depositions. Actual film thickness was measured using a Dektak-8 stylus profilometer. The substrate holder maintains the substrate temperature of 65°C, which is necessary to achieve an a-Se film with a high electrical quality, as reported previously by Dr. Belev [42]. The electrical quality and reproducibility of the a-Se film fabricated using

Table 3.2: Deposition conditions for a-Se films using thermal evaporator in G2N lab.

Chamber Pressure (torr)	5×10^{-7}
Substrate temperature ($^{\circ}C$)	65
Deposition rate (A/s)	110(<i>for</i> $\leq 40\mu m$) and 170 – 180(<i>for</i> $> 40\mu m$)
Boat temperature ($^{\circ}C$)	300-400
Platen rate (RPM)	50

this evaporation system were investigated previously and demonstrated that the quality of the film meets the standard for an electronics-grade a-Se [4]. The deposition parameters used with this system are summarized in Table 3.2. The selenium source material used for the fabrication of the detectors were pellets alloyed with 0.2% arsenic (As) and 10 ppm chlorine (Cl) with 5N purity (supplied by New Metals and Chemicals Corporation in Japan). Such an a-Se composition is called stabilized a-Se which provides increased stability and hole transport properties. A thin layer of gold (50 nm) was deposited on top of an a-Se film as a top electrode for each detector using a shadow mask. The evaporation of gold is performed using another thermal evaporation system dedicated for metal and organic material deposition at G2N. The active area of each detector is defined by the area of opening in the shadow mask.

3.2.2 Measurement setup and experimental details

Critical to its feasibility to determine single photon detection and photon counting capability of a-Se with the common radiation sources, the PHS experimental setup needs to be optimized for a lower gain, and slower response observed with a-Se detectors due to its electron transit-time limited response and high ionization energy (i.e., $W_{\pm} \sim 45eV$ at $10 \text{ V}/\mu m$). Shown in the Fig. 3.1 is the PHS experimental setup diagram where the a-Se sample is used as a gamma-ray ionization detector. The front-end electronics employed in the PHS system is mainly composed of charge-sensitive preamplifier, shaping amplifier and multi-channel analyzer. Current pulses resulting from the charge created by absorbed

photons were integrated on the low-noise charge preamplifier. The output voltage of the preamplifier is proportional to the induced charge due to the single photon absorption in a-Se detector. The preamplifier also acts as a buffer layer for a-Se detector by isolating the loading effects of the subsequent signal processing stages. In order to minimize capacitive loading effect on the preamplifier input stage, the detector is located very close to the preamplifier and a short interconnecting cable is used. Ideally the preamplifier does not provide any signal shaping, and it is capable of driving the signal output to the subsequent electronics represented by a large capacitance. The rise-time of the signal is consistent with the charge collection time in a-Se detector. The PHS system consists of Amptek-A250CF charge amplifier and Ortec-570 shaper, which is modified to provide shaping times in the range of 0.5-44 μ s. Assuming the preamplifier has an open loop gain of $-A$, the output voltage is given by:

$$V_{out} = -AV_{in}, \quad (3.1)$$

$$V_{out} = -A \frac{Q}{C_i + (A + 1)C_f}, \quad (3.2)$$

$$V_{out} = -\frac{Q}{C_f} \left(\text{Assuming } A \gg \frac{C_i + C_f}{C_f} \right), \quad (3.3)$$

where C_i is the input capacitance, Q is the photoinduced charge, C_f and R_f are the feedback capacitance and resistance respectively. The equation 3.3 states that the V_{out} is proportional to the total integrated charge and independent of the input capacitance. The decay time of the output signal is determined by the time constant of the feedback circuit, which is equal to $R_f.C_f$. To ensure complete charge collection, the preamplifier feedback circuit was designed to provide an adequate decay time while maintaining the lowest possible thermal noise originating from the feedback resistor.

A shaping amplifier was utilized for conditioning the preamplifier output signals with extended decay times to minimize pile-up probability and to improve signal-to-noise ratio.

Shaping time was also adjusted in consideration of the slower carrier transit time, (i.e., electrons in a-Se), to avoid ballistic deficit [59]. The shaped pulses were converted by the multi-channel-analyzer (Ortec-927) into digital data which forms the pulse height spectra. System noise and linearity tests were carried out by injecting a known amount of charge through the test input and measuring the corresponding spectral response, similar to the procedure followed in section 5.3.1. The preamplifier input capacitance was minimized to reduce input-referred noise in order to achieve definable peaks on the component of the low frequency noise. The dominant contributor to the electronic noise was then found to be the preamplifier with the measured noise of $420 e^- + 12 e^-$, which is within the range of noise rating reported by the manufacturer.

Dark and photo currents were measured as a function of applied electric field. A high-voltage power supply (SRS-PS365) to apply a positive voltage on the ITO layer, and a semiconductor parameter analyzer (Agilent-4156) were both automated to carry out dark-current measurements. The samples were rested in a short circuit configuration in a light-proof-box for at least 24 hours between measurements to enable complete release of trapped charge. Photo-current measurements were performed using a low noise current amplifier (Keithley-427) having programmable bandwidth and gain settings. The output of the current amplifier was connected to an oscilloscope. Before the measurements, the a-Se sample was replaced by a photodiode to evaluate the current amplifier response. Oscilloscope traces were offset corrected using the current suppression adjustment of the current amplifier. Samples were exposed to X-ray pulses similar to that of fluoroscopy, (i.e., 30 fps at $10 \mu\text{R}/\text{frame}$), where the X-ray pulse generator (EPS 45-80 RF) was programmed and triggered using a signal generator.

3.3 Results and discussion

3.3.1 Pulse height spectroscopy measurements

The measured spectra from our fabricated a-Se detectors are shown in Fig. 3.3(a). The detectors were all operated at the same applied voltage (750V) while being irradiated by a collimated mono-energetic gamma-ray source (Am241, 59.4 keV). Measurements were carried out for at least 12 hours until the spectral peaks were clearly observed above the background noise. A tailing in the low energy region of the spectra is insignificant for the purpose of this study indicating an incomplete charge collection due to the poor inherent transport properties of electrons in a-Se. Our measured ionization energy, W_{\pm} , of approximately 45 eV from 75- μm -thick a-Se detector with a 0.8- μm -thick PI layer is in agreement with previously reported studies [13].

From our results in Fig. 3.3(a), we are able to derive the internal electric field of a-Se in each detector regardless of the employed PI layer thickness. Previous studies have shown that W_{\pm} in a-Se is inversely correlated to the applied electric field [13]. Therefore, we expect that if the applied fields are the same, the spectral peaks should be formed at the same location, under the assumptions that (1) the photon energy and electrical properties of a-Se films are identical, (2) no significant space charge is developed, and (3) the electric field is uniform. However, as is apparent from Fig. 3.3, W_{\pm} is not constant, which we can attribute to the degradation of the internal electric field due to the increased thickness of the PI layer.

We also carried out measurements to determine the required fraction of the applied voltage needed to obtain the same internal electric field for all three detectors. We increased the applied voltages to the a-Se detectors having 1.8- μm and 3- μm -thick PI layers until a W_{\pm} of approximately 45 eV was observed for all detectors. The results are shown in Fig. 3.3(b), where a sub-linear dependency is evident. The extrapolated value of voltage increment is about 60 V for every 1- μm increase in PI layer thickness, assuming that a scaled-field extrapolation is acceptable. Our estimated value is smaller compared to previ-

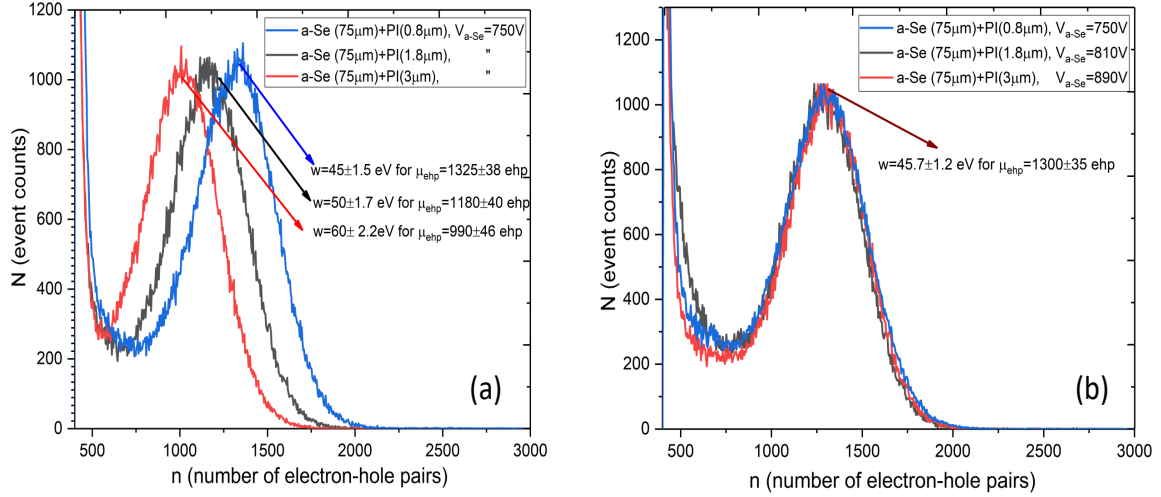


Figure 3.3: a) The measured ^{241}Am (59.4 keV) spectra of a-Se/PI detectors with a different PI thickness and same applied voltage, 750V, b) The corrected ^{241}Am spectra of a-Se/PI detectors for the same applied field, i.e., $10\text{V}/\mu\text{m}$. The required fraction of the applied voltage per $1\ \mu\text{m}$ PI layer is estimated around 60 V to achieve the same internal electric field for a-Se detectors having different thickness of PI layers.

ously reported threshold electric field for carrier injection (i.e., $140\ \text{V}/\mu\text{m}$), implying that hole injection does not contribute significantly to electrical conduction [108]. Consequently, our devices are operated in the *steady-state* regime in the absence of photo-illumination. It was shown in previous studies that the electric field configuration in a-Se detectors, especially around the contact metals, under illumination can be substantially changed, which may cause an excessive charge injection in turn [114]. This is further investigated with our devices in *Photoresponse* section.

3.3.2 Dark Current Measurements

We now investigate the influence of PI layer thickness on the dark-current and photo-current levels of our a-Se detectors under different applied fields. Previous studies of the

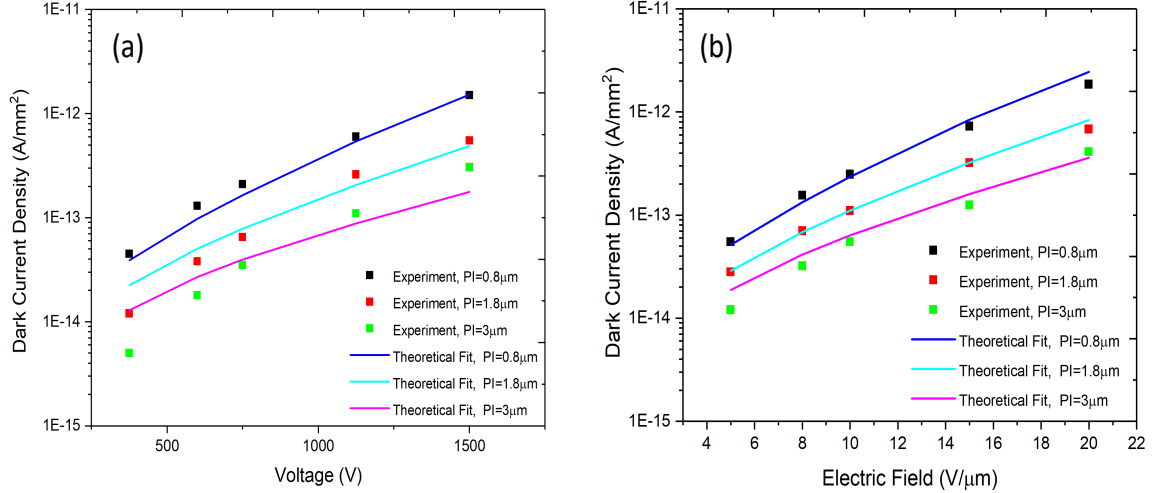


Figure 3.4: a) Dark current density of a-Se detectors a) as a function of applied voltage, b) as a function of applied electric field. The dark currents are measured after 3600 second following the high-voltage application.

dark current in a-Se/PI structures mainly considered the applied voltage dependence where it is not possible to scale this to the same electric field especially for the devices prepared for indirect imaging. Voltage drop within the PI layer of such devices can be significant as the application requires a device having a respectively thin a-Se layer, (e.g., 2-16 μm). It is therefore critical to measure dark and photo currents for the same internal electric field after the investigation of voltage drop within the PI layer.

We first display the measured dark-current of our detectors as a function of applied voltage in Fig. 3.4(a). Because the dark current decays with time before setting due to a time-dependent trap localization process in a-Se, we report the dark current after 3600 second following the high-voltage application. As apparent from the results, dark current increases with increasing applied voltage. However, it is questionable that whether the lower dark current observed for devices with thicker PI layers is due to the more effective dark current suppression or diminished internal electric field.

For a better comparison, we now show, in Fig. 3.4(b), the measured dark current as a function of applied electric field. Although the dark current slightly increases for both detectors having 1.8- μm and 3- μm -thick PI layers after adding the fraction of the voltage required to determine the internal electric field same for all detectors, it appears that the thicker PI layer further reduces the dark current. It is also evident that using relatively thin PI layer under high applied electric field (i.e., above 20 V/ μm) may not be sufficient to achieve the dark current level within the range necessary for low-dose clinical X-ray imaging applications, such as fluoroscopy [2].

3.3.3 Photoresponse

Detectors were illuminated with a pulsed X-ray source to investigate whether the increased PI thickness leads to a charge accumulation. This is of great importance because any major charge accumulation within a-Se/PI interface degrades internal electric field substantially, which makes a-Se impractical for X-ray imaging applications due to its electric-field-dependent charge generation and collection efficiencies. The measurements were carried out under varying applied voltages, electric fields and X-ray dose. The dose was measured with a dosimeter (Solidose-300) during each measurement. The dosimeter was placed at the same level as the detectors and the dose was tracked for all exposures. We expect to observe a sub-linear relationship between photo-current and bias voltage based on our assumptions that drift as the main component of photo-current, and that there is no space-charge-limited conduction inside a-Se [52]. As seen in Fig.3.5(a), the photo-current amplitude is higher for the device with the thinnest PI layer, and decreases with increasing the PI layer thickness for the same applied voltage and a-Se thickness. This demonstrates that the effective electric field within the bulk is degraded due to the presence of thicker PI layer, as was the case for PHS experiments. Although the photo-current slightly decreases during the pulse, the amplitudes of consecutive pulses are similar. We speculate that the slight decrease in photo-current at the end of each pulse is caused by the fact that the rate of electron flow from the a-Se layer through the PI layer towards the ITO contact might

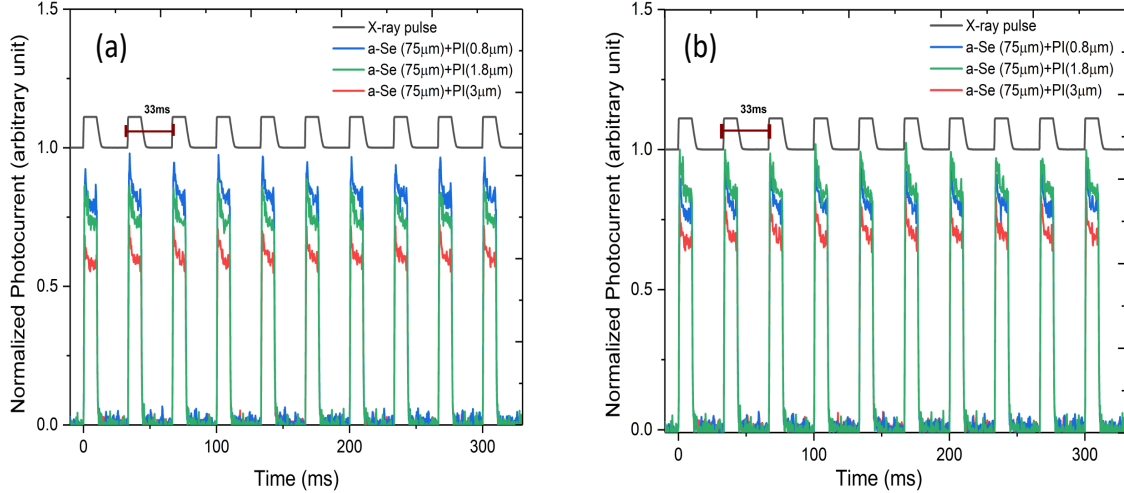


Figure 3.5: a) Photocurrent measurement results for the same applied voltage, i.e., 750 V, and b) same applied electric field, i.e., 10 V/ μm . Detectors were exposed to X-ray pulses similar to that of fluoroscopy, (i.e., 30 fps at 10 $\mu\text{R}/\text{frame}$),

be slightly slower than the accumulation of X-ray generated electrons at the interface, which temporarily changes the internal electric field. However, the recovery mechanism that creates injecting/non-injecting current within the metal contact with PI works very fast even with very short pulses, which proves that there is no significant accumulation at the interface.

Fig. 3.5(b) shows the measured photo-current dependence of the a-Se detectors on the applied electric field. We observe that, although the modification of applied bias to have same internal electric field increases the photo-current amplitudes for the samples with a 1.8- μm and 3- μm PI layers, photo-current measured for the sample with a 3- μm PI layer remains lower compared to other samples. The reason of having a lower photo-current for the sample with a 3- μm -thick PI layer is that the rate of electron flow from the bulk of a-Se, through the PI layer towards the ITO contact might decrease with further increasing the PI layer thickness.

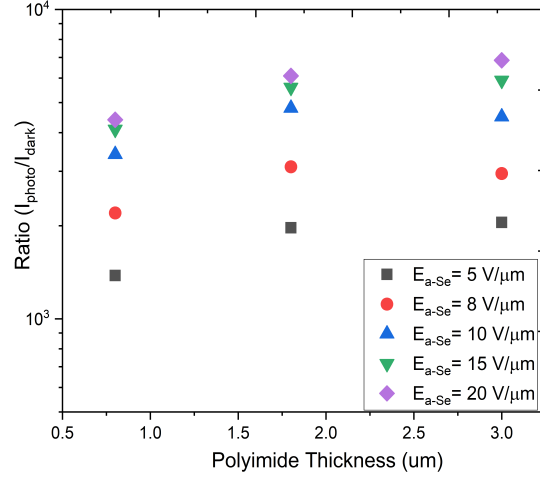


Figure 3.6: Photo-to-dark current ratio of the PI/a-Se detector as a function of PI thickness at various electric fields.

To investigate whether the use of a thicker PI layer reduces the dynamic range of our a-Se detectors, we carried out further photo-current measurements. Fig. 3.6 illustrates the photo-to-dark current ratio results for all fabricated detectors as a function of applied electric field. We observe that a PI thickness of about $1.8 \mu\text{m}$ is optimal for achieving higher photo-current while maintaining low dark current, and no further improvement is achieved using a thicker PI layer. We attribute this result to two reasons. First, the reduction of the interface electric field depends on the trapped-carriers concentration. However, as the amount of trapped carriers increases, it eventually saturates so no further dark-current reduction is observed. Second, further increase in the PI layer thickness does not provide more dark-current suppression since the thermal generation current determines the lowest dark current attainable.

3.4 Mathematical Model

Previous experimental works have demonstrated that the main source of dark current in a-Se detectors is the injection of holes from the metal contacts and the bulk thermal generation current is relatively small [104, 86]. The measured dark-current results from our detectors are consistent with the fact that the bulk thermal generation and electron injection currents are negligible compared to the hole injection current because of the high band gap and a very low electron mobility in a-Se, respectively. Once the injection current is suppressed, the thermal generation current determines the amount of the dark current. This is apparent from our measured results that further increase in PI layer does not decrease the dark current. Furthermore, although the dark current increases with the increased electric field, we observe that there is no strong dependence on electric field, as is the case for the Poole-Frankel model. Therefore, we believe it is more appropriate to model the dark current behavior of a-Se/PI devices with the Poole-Frankel emission model because of this weak dependency and material characteristics of PI with lots of defect states.

The present result of Fig. 3.3 indicates that the change of voltage needed per 1 μm PI layer is 60 V to maintain the same internal electric field (10 V/ μm) in a-Se layer. That means, the voltage drop across the PI layer per unit thickness is almost seven times larger than that in the a-Se layer, which indicates that the average electric field in the PI layer is approximately seven times larger than a-Se layer. Since the average resistivity of the PI layer is almost an order of magnitude larger than a-Se, the injection current is limited by the charge carrier transport through the PI layer. A very high density of surface states ($2.5 \times 10^{20} \text{ cm}^{-3} \cdot \text{eV}^{-1}$) exists in the PI layer within 1 nm from the metal contact [115]. These states consist of electron and hole trapping states with Gaussian distribution peaked at LUMO and HOMO states. The LUMO and HOMO levels at the surface of PI are located at about -3.8 eV and -6.3 eV from the vacuum level. Charge carriers detrapping from the surface states constitute a current. According to [115], current due to charge detrapping from surface traps with Poole-Frenkel effect is [116],

$$J_h(t) = eN_V\mu_h F_1(t)\exp\left\{-\frac{\phi_h - \beta_{PF}\sqrt{F_1}}{kT}\right\}, \quad (3.4)$$

where k is the Boltzmann constant, T is the absolute temperature, $\beta_{PF} = \sqrt{e^3/\pi\epsilon_{pi}}$ is the Poole-Frenkel coefficient, e is the elementary charge, $\epsilon_{pi}(= \epsilon_0\epsilon_r)$ is the permittivity of PI, N_V is the effective density of states in the valence band of PI, $F_1(t)$ is the instantaneous electric field at the ITO/PI interface and μ_h and ϕ_h are the effective hole mobility and barrier height in the PI layer, respectively. The effective drifting hole concentration in the PI layer can be written as:

$$p(t) = N_V\exp\left\{-\frac{\phi_h - \beta_{PF}\sqrt{F_1}}{kT}\right\}. \quad (3.5)$$

The instantaneous electric field $F_1(t)$ changes due to trapping/detrapping of injected holes in the energy distributed deep trapping states of the PI layer. The energy distributed deep trapping states are discretized to m segments/levels. The trapping rate equation for the trapped holes at a trap level E_{tm} is:

$$\frac{dp_{tm}}{dt} = C_{tm}N_{tm}\theta_h\left[1 - \frac{p_{tm}}{N_{tm}}\right]p(t) - \frac{p_{tm}}{\tau_{rm}}, \quad (3.6)$$

where N_{tm} is the initial unoccupied trap concentration at the trap level m , C_{tm} is the deep trapping capture coefficient, p_{tm} is the trapped hole density, $\theta_h = \mu_h/\mu_{0h}$, μ_{0h} is the hole mobility in the extended states of the PI layer, and τ_{rm} is related to the trap depth E_{tm} from the mobility edge of the valence band by $v^{-1} \exp(E_{tm}/kT)$, where v is the attempt-to-escape frequency. The relation between v and C_{tm} can be determined by the principle of detailed balance, which gives $v = N_v C_{tm}$.

Since the thickness of the PI layer is much smaller than the bulk, a nearly uniform trapping/space charge, over a long time, can be assumed in the PI layer. Neglecting trapping in the nearly intrinsic a-Se layer, the instantaneous electric field $F_1(t)$ is determined by solving the Poissons equation with the boundary condition that the integral of the electric field distribution must equal to the applied voltage, i.e.:

$$F_1(t) = \frac{V_0}{(L/r + d)} - \frac{ep_t(t)d}{2\epsilon_{pi}}, \quad (3.7)$$

$$p_t(t) = \sum_m p_{tm}(t), \quad (3.8)$$

V_0 is the applied bias voltage, L is the a-Se layer thickness, d is the PI layer thickness and r is the ratio of resistivity of the PI layer with respect to a-Se layer.

The defect states close to the middle of the bandgap of a-Se have a significant probability for thermal excitation of both types of carriers. Therefore, the steady-state thermal generation rate is dominated by the emission from traps within kT of E_{FD} [86]. If the excitation rates for electrons and holes are equal, E_{FD} is very close to the middle of mobility gap. The generation rate for a fully depleted sample is determined by the average carrier release time and can be written as [117]:

$$g = N(E_{FD})kTv \exp \left[- (E_c - E_{FD} - \beta_{PF}\sqrt{F})/kT \right], \quad (3.9)$$

where, $N(E_{FD})$ is the density of states of a-Se at energy E_{FD} in the midgap. It is assumed in equation 3.9 that the density of states is constant over kT near E_{FD} in a-Se. Assuming that the liberated carriers are not lost by trapping or recombination (any loss of carriers can be reflected in the effective value of g) the steady-state thermal generation current,

$$J_{th} = egL. \quad (3.10)$$

The total dark current density is the sum of all current components, $J_d(t) = J_h(t) + J_{th}$.

The coupled algebraic-differential equations 3.4-3.9 are simultaneously solved using MATLAB to get the instantaneous electric field profile, trapped carriers, and dark current. We consider six discrete deep hole trapping states, E_{tm} from 0.7 to 0.95 eV, and the energy width of each state is 0.05 eV. Note that the shallower trap levels (eV) retain negligible trapped carriers because of the very short thermal release time. The effective hole mobility $\mu_h = 10^{-6} cm^2/Vs$ [118], $N_V = 6 \times 10^{21} cm^{-3}$ [109], and $\epsilon_r = 3.4$ [108] are

taken in calculation for the PI layer. Fig. 3.4 shows the simulated dark current results for various PI layer thicknesses as a function of applied voltage and electric field in a-Se layer, respectively. Symbols and solid lines present experimental data and theoretical fit to the experimental results, respectively. Thicker PI layer provides more effective dark current suppression due to higher trapped carrier in the PI layer which reduces the electric field at the ITO/PI interface (See equation 3.7) and thus reduces the hole injection current as well.

One can notice that the model shows a better agreement for the dark current versus field characteristics (Fig. 3.4(b)) than for the dark current versus voltage characteristics (Fig. 3.4(a)). The reason is that the internal electric field is not accurately known in dark current versus voltage measurement and the dark current depends critically on the interface electric field (F_1 in equation 3.4). Moreover, the model shows a very good agreement in dark current versus field characteristics for the PI layer thickness of 0.8 and 1.8 μm . However, the agreement is not well for the PI thickness of 3 μm (magenta curve in Fig. 3.4(b)). The assumption of uniform trapping in the PI layer is reasonably good for thinner PI layers but probably starts to fail in thicker PI layers (3 μm or more). Note that a minor error in the calculation of interface electric field (equation 3.7) can make a substantial change in the calculation of injection current (equation 3.4).

3.5 Conclusion

We demonstrated the use of PHS measurements, to the best of our knowledge, the first use of pulse-height-spectroscopy (PHS) to determine the hole transport mechanism of the emerging blocking contact material, PI, when integrated with an a-Se photoconductor. The experimental results show that approximately 60 V is necessary for every 1 μm PI layer added in a-Se detector to maintain the same internal electric field. Also, the hole conduction mechanism in PI layer is modelled by employing Poole-Frankel Model due to the weak dependency of the measured dark current to the internal electric field and the

material characteristics of PI with lots of defect states. Our approach using PHS offers a new experimental technique to better understand the impact of emerging blocking contact materials when integrated with existing (e.g. a-Se, CZT) and emerging (e.g. HgI₂, PbO, TlBr) direct conversion radiation detectors. Acquiring better insight into the conduction mechanisms of blocking contacts is a critical step to designing high-performance radiation detectors with enhanced lifetimes and photosensitivity, and low leakage currents and photocurrent lag.

Chapter 4

Modeling of Amorphous Selenium Based Unipolar Charge Sensing Detectors

4.1 Introduction

The performance of energy integration systems is inherently limited, due to inefficient noise rejection capabilities [119]. High noise degrades signal-to-noise ratio, and leads to poor dose efficiency, which is compensated for by an additional radiation dose [60, 120]. An alternative approach to energy integration systems is the use of photon-counting detectors, which can efficiently eliminate electronic and Swank noise, and enables proper energy weighting, which improves signal-to-noise ratio in the low contrast region (e.g. soft tissue) [121, 122, 123, 124]. Existing photon-counting detectors for breast screening is based on silicon (Si) and cadmium-telluride (CdTe) technology [125, 126, 127, 128]. However, these materials are not compatible with large area fabrication, and they each have their own specific limitations. For example, Si has a low atomic number, limiting its use for high-photon energy imaging applications. On the other hand, CdTe suffers from low fabrication

yield and poor charge transport problems [129, 130].

Amorphous selenium (a-Se) can address some of the aforementioned limitations of photon-counting detectors for breast screening applications (e.g., mammography and tomosynthesis) [131]. The rationale for exploring a-Se for photon-counting includes: (1) a-Se offers cost-effective and reliable coupling to large area readout circuitry; (2) a-Se provides very high intrinsic spatial resolution and detection efficiency in the mammography energy range (with a lower k-edge energy, 12.6 keV), compared to crystalline photoconductors such as CdTe; 3) a-Se detectors can be operated at room temperature due to their wide band-gap (2.2 eV) [132, 133]. All of these attributes render a-Se attractive as a photon-counting radiation detector. Currently, the highest performance commercially available energy integrating mammography detectors are based on a-Se technology.

Despite the unique advantages of a-Se noted above, some limitations remain. These include electron trapping and high ionization energy, W_{\pm} [13, 134]. Poor electron transport is a critical issue in the development of photon-counting a-Se detectors. For example, the charge collection time for each EHP created in a-Se layer may vary, depending on photon-interaction depth, due to portion of the signal being induced by an electron. Furthermore, and most importantly, electrons can be trapped prior to being collected by the collecting electrode, which greatly reduces charge collection efficiency. Assuming that all the photogenerated charges are collected with a higher collection efficiency, the photon-counting rate of conventional a-Se falls significantly short from meeting the required count-rate for photon-counting mammography, due to the longer shaping time (e.g. 10-100 μ s) necessary for electron collection. All of these effects give rise to an asymmetric long tail to the left of the photopeak in the measured energy spectra, and degrades energy resolution. The high ionization energy of a-Se is another cause for the degraded energy resolution, because the intrinsic energy resolution is fundamentally limited by the number of EHP generated for a given photon energy. Recently, some studies have demonstrated that this fundamental limit can be addressed by achieving an avalanche gain, by operating the a-Se detector at a very high electric field (~ 90 V/ μ m) [92, 135, 136].

In this chapter, using theoretical calculations and analytical models, we demonstrate that the primary limitation of a-Se detectors lead to a degraded temporal resolution. The simulation results for induced signal on the collecting electrode, as a result of single photon interaction, and for pulse-height analysis using the Monte-Carlo method, are obtained using both conventional and unipolar charge-sensing a-Se detectors. The energy resolution and Swank factor for the conventional detectors, which define the lowest theoretical noise achievable in a-Se, are calculated based on the simulation results, and compared with that of unipolar charge-sensing device results.

4.2 Induced signal analysis

In ionic materials and doped semiconductors, charge neutrality is retained at all points, because the photogenerated charge is covered by the compensating charge, and its field is prevented from being sensed at a microscopic distance. As a result, no current is observed on the collecting electrode until the drifting charge arrives to the corresponding electrode [137]. However, for high resistivity photoconductors, there is no reservoir of compensating charge; thus, charge neutrality is not observed, at least not in the time scale where the drifting charge reaches the corresponding electrode. The characteristic relaxation time of a medium is given by $\tau = \epsilon\rho$, where ρ is resistivity, and $\epsilon = \epsilon_0\epsilon$ is the dielectric constant of the material. For example, a-Se has a resistivity of approximately $10\text{E}+14 \Omega\text{cm}$, and a relative dielectric constant of 6.7. Hence, the relaxation time is estimated at roughly one minute. This relaxation time is very long compared to the typical carrier transit times of a few ten micro-seconds. Therefore, the photocurrent resulting from the photogenerated carrier arises entirely due to induction. For the detector having a single-continues electrode (Fig. 4.1), the induced charge can be found simply by the conservation of energy argument as following [137, 138]:

- The total power necessary to move the charge package, q , at velocity v in the direction of the electric field, E , is equal to $P = qEv$.

- This power must be supplied by the power supply that maintains the voltage, $V = E.L$, which is constant over the photoconductor thickness, L . The power is also equal to $P = V.i$, where i is the current. Thus, $i = qv/L$.
- The charge package can be separated into electrons, $-eN(t)$ and holes, $eN(t)$, each of which are collected by the opposite electrodes, and their densities can be changed due to trapping/detrapping and recombination. The current of the single-continuous pixel electrode is then found as:

$$i(t) = \frac{e}{L}[N_e(t)v_e + N_h(t)v_h]. \quad (4.1)$$

Assuming the electrode is connected to active integrator circuits (e.g. charge-sensitive preamplifier), and the integration time is long enough for allowing the charge carriers to reach their respective electrodes (possibly, some of the charge can be trapped in the bulk of the photoconductor), the net charge as a function of photon interaction depth is given by:

$$Q(z_i) = \frac{eN_e\lambda_e}{L}[1 - \exp(-\frac{z_i}{\lambda_e})] + \frac{eN_h\lambda_h}{L}[1 - \exp(-\frac{L - z_i}{\lambda_h})]. \quad (4.2)$$

The energy conservation argument, however, is not applicable to the pixelated electrodes, because it gives the total current, not the fraction that flows through a single pixel. For the pixelated detector, the instantaneous electric field, E , (normal component over the surface of pixel electrode S) on the trajectories of each charge carrier should be calculated to find the total time-dependent charge, Q . Q , which arises due to a single EHP motion, is given by:

$$Q = \oint \epsilon E.ds. \quad (4.3)$$

Considering the large number of electric field components that need to be calculated on

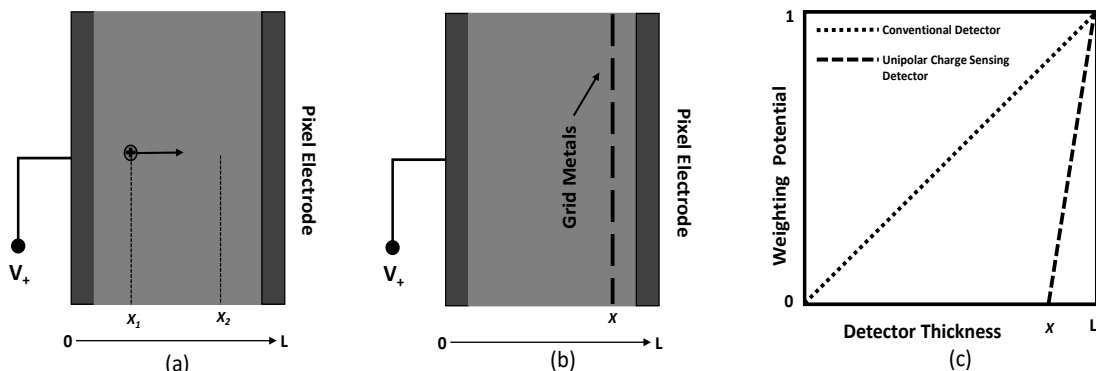


Figure 4.1: a) Cross section of a conventional pixelated detector, b) Cross section of a detector with an internal grid layer, c) Weighting potential distribution for a conventional and unipolar charge sensing detector.

each point of the charge trajectory, and the large number of EHPs for each incident photon, this calculation will be tedious and time-consuming to perform.

4.2.1 The Shockley-Ramo theory

The Shockley-Ramo theorem provides a much more convenient means for calculating the induced charge on pixelated electrodes [139, 140]. The Shockley-Ramo theorem was initially introduced for vacuum-tubes where no space-charge exists, but was later formulated for semiconductor devices with a space-charge [141]. The calculation of an induced charge with the Shockley-Ramo theorem depends on the geometry of the detector and pixel electrode, material properties, and weighting potential.

The weighting potential for a specific pixel electrode, i , is the electrostatic potential produced by assuming that the pixel electrode i is set to unit potential, all other pixel electrodes are grounded, and no space-charge exists. The weighting potential, ϕ_i , is a dimensionless quantity and can be solved by the Laplace equation below (4.4), using electromagnetic field simulation software (e.g. COMSOL Multiphysics, which was applied in this thesis), setting the voltage of the corresponding pixel electrode to 1, and the top

electrode and other pixel electrodes to 0.

$$\nabla^2 \phi_i = 0. \quad (4.4)$$

The induced charge Q_i and current I_i due to the motion of point charge q on the pixel electrode i is given by:

$$Q_i = -q\phi_i(\mathbf{x}), \quad (4.5)$$

$$I_i = qv \cdot E_i(\mathbf{x}), \quad (4.6)$$

where v is the instantaneous velocity of the moving charge q , and $E_i(\mathbf{x})$ is the conceptual weighting field. The unit for the weighting field is m^{-1} .

If we assume charge q in Fig. 4.1(a) is moved from \mathbf{x}_1 to \mathbf{x}_2 , the induced charge due to this movement on the pixel electrode i is given by:

$$Q_i = q[Q_i(\mathbf{x}_2) - Q_i(\mathbf{x}_1)] = q \frac{\mathbf{x}_2 - \mathbf{x}_1}{L}, \quad (4.7)$$

where L is the thickness of the photoconductor. Note that the weighting potential for a conventional detector is a linear function of depth, with 0 at the biased electrode, and this increases linearly to 1 at the pixel electrode, as shown in Fig. 4.1(c). For example, for the single-element detector with a single continuous electrode, $E_i(\mathbf{x}) = 1/L$ and $\phi_i(\mathbf{x}) = \mathbf{x}/L$; thus, the induced current is given as $I_i = qv/L$. Calculating the weighting potential of the charge q at \mathbf{x} on its track to the pixel electrode, the induced charge on the pixel electrode is estimated as $-q\phi_i(\mathbf{x})$. This means that the total charge removed from the pixel electrode to the readout circuit as a result of the charge motion in the bulk of the detector is given by $q \Delta\phi_i(\mathbf{x})$. Equation 4.7, with its very basic form, states that if charge q is trapped somewhere within the bulk, only a fraction of the photo-induced charge is collected by the

read-out circuitry. Additionally, it is obvious from the equation that the induced charge on the collecting pixel electrode is only determined from the initial and final location of the drifting charge carriers, and is independent of the actual detector potential and space-charge that may be present. Note that the form of the weighting potential is different than that of the actual electric potential of the detector. The actual electric potential only defines the trajectory and velocity of the charge carriers.

4.2.2 Unipolar charge sensing

When a unipolar charge-sensing device is considered, either with an internal grid (e.g. a Frisch grid) [50] or small pixel effect [142], weighting potential is no longer considered a function of detector thickness. Such localized preferential charge-sensing can be implemented by establishing a strong near-field effect within the proximity of the pixel electrode. The basic unipolar charge-sensing device structure with an internal grid and corresponding weighting potential distribution (ideal case) is shown in Fig. 4.1(b) and (c). Such a weighting potential distribution means that no charge is induced on the pixel electrode, due to movement of charge carriers between the top electrode and the grid layer (i.e. far-field). Only the charge with a higher mobility passing through the grid layer contributes to the output signal of the detector. It should be noted that the weighting potentials calculated in Fig. 4.1(c) assume that there is no charge-trapping in the bulk of the photoconductor.

The difference between the weighting potentials for the conventional and unipolar charge-sensing detectors can be explained based on the idea that the induced charge on the pixel electrode is proportional to the density of the electrostatic flux-lines terminating on the corresponding pixel electrode. For the conventional detector, the flux-line density connecting the moving charge to the pixel electrode is constant through the photoconductor; therefore, the weighting potential changes in proportion to the detector thickness, reaching 1 on the collecting pixel. However, referring to the electric field simulation results for the corresponding unipolar charge-sensing device in Fig. 4.2(d), the flux lines are evenly distributed in the bulk, but much more dense in the region between the grid layers and the

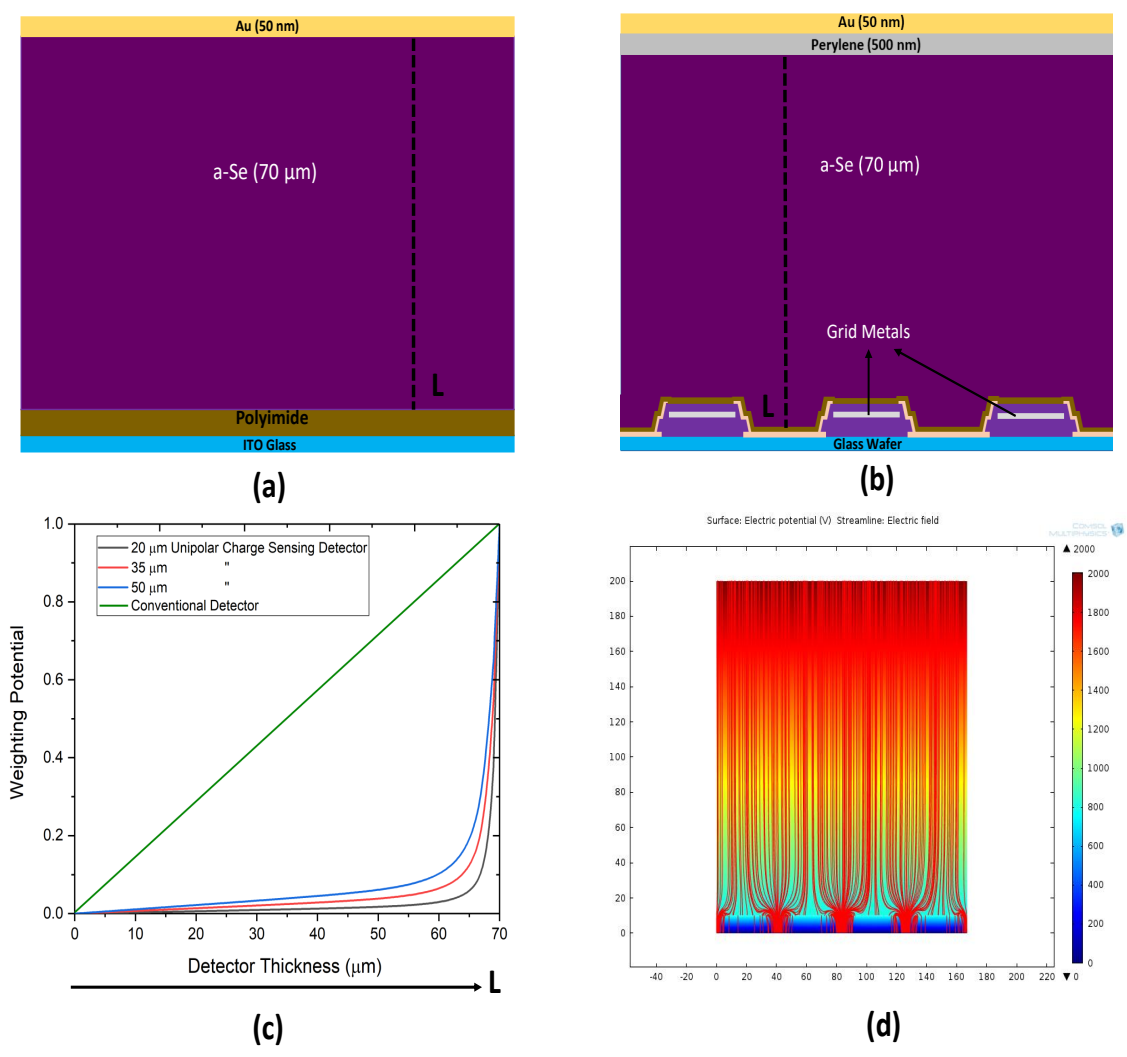


Figure 4.2: Cross-sectional view of (a) conventional and (b) unipolar charge sensing detectors, (c) simulated weighting potentials for the detector in (a) and (b), (d) and electric field simulation of unipolar charge sensing detector.

collecting pixel (i.e. the near-field region) when a voltage with the same polarity is applied to both the top electrode and grid layer. Such a flux-line density produces a rapid rise in collecting pixel signal once the moving charge enters into this near-field region. In the next

chapter, we demonstrate that this unique charge induction mechanism can be utilized to reduce loss of spectroscopic resolution caused by poor electron collection in a-Se detectors.

4.3 Simulation results

Due to the lower electron mobility of a-Se detectors, the random distribution of photon interaction through a photoconductor causes significant fluctuation in the induced charge. This fluctuation gives rise to peak broadening in the energy spectra, and considerably degrades the energy resolution of the a-Se detector. However, we expected the unipolar charge-sensing device to primarily prevent a charge induction on the collecting electrode due to the portion of slower carriers motion, and leads to improved energy and time resolution in a-Se detectors. However, the extent to which the unipolar charge-sensing can help to reduce the adverse effect of slower carriers on the time domain response of a-Se detectors remains unclear. To properly answer this question, and to quantify temporal response and energy resolution improvement, we first analyzed the time-domain response and intrinsic energy resolution of a conventional a-Se detector using simulation studies.

The conventional and unipolar charge-sensing detectors in Fig.4.2(a) and (b) were fabricated and employed for our experimental measurements (details will be provided in the next chapter). A conventional detector consists of an a-Se photoconductor layer that is fitted between two electrodes to form a sandwich cell; one is the top electrode with a specific electric potential for establishing an electric field for carriers drift, while the second is the pixel electrode, which is generally kept at 0 potential and connected to the read-out circuit to collect photogenerated charge. The unipolar charge-sensing detector, however, additionally includes internal grid metals to establish a near-field effect. The top and grid electrodes are positively biased, so that charge carriers with a higher mobility life-time product (e.g., holes for a-Se) are steered down to the collecting electrode. Based on the equation 4.5 and the conditions mentioned in the previous section, weighting potential distribution along the vertical line passing through the center of the collecting electrode

for both detectors were calculated, and results are shown in Fig. 4.2(c). The weighting potential provides a means for visualizing the development of signal output as the charge carriers move within the photoconductor. It can be seen in Fig. 4.2(c) that most of the signal generation occurs in the near-field region of the unipolar charge-sensing device, while the signal output for the conventional device constantly develops as the charge carriers traverse, indicating the depth-dependent response. Carriers moving within this near-field area contribute most to the total signal, while the motion of carriers outside this region contribute very little. Electrons trapped outside the near-field region is of little importance for the unipolar charge-sensing device, because the electrons are not likely to induce significant charge on the collecting electrode. For conventional detectors, however, all carrier motion that happens within the bulk of a-Se is responsible for development of the signal.

4.3.1 Signal rise-time

The temporal response of the collected charge using the simulated weighting potential results is calculated as a function of photon-interaction depth. The collected charge can be found by means of weighting potential, by simply integrating equation 4.6 for the boundary conditions, as defined by charge carrier drift time. The right-side of equation 4.6 is the time derivative of $-eV_W(x)$; hence, as the point charge moves from position x_1 to x_2 , the net charge built-up on an integrating capacitor connected to the electrode, alongside the contributions of electrons and holes, is given by [143]:

$$Q_b = e \frac{\mu_h E \tau_h}{\Delta x} \left[1 - e^{\frac{-\Delta x}{\mu_h E \tau_h}} \right] \sum_{n=1}^{\frac{L-x_i}{\Delta x}} \left\{ [V_W(x_i + [n-1]\Delta x) - V_W(x_i + n\Delta x)] e^{\frac{-n\Delta t_h}{\tau_h}} \right\}, \quad (4.8)$$

$$Q_b = e \frac{\mu_e E \tau_e}{\Delta x} \left[1 - e^{\frac{-\Delta x}{\mu_e E \tau_e}} \right] \sum_{n=1}^{\frac{x_i}{\Delta x}} \left\{ [V_W(x_i - [n-1]\Delta x) - V_W(x_i - n\Delta x)] e^{\frac{-n\Delta t_e}{\tau_e}} \right\}, \quad (4.9)$$

where x_i is the photon absorption depth, E is the electric field, and μ and τ are carrier mobility and lifetime, respectively. The subscripts e and h represent electron and hole, respectively. Δt_h and Δt_e are the times required for a hole and electron to travel a distance of Δx . The results were obtained at $E = 8\text{V}/\mu\text{m}$ (the same field used for experiments), using the electrical properties of our fabricated a-Se film, as summarized in Table 4.1. Hole and electron mobilities were measured with a time-of-flight measurement technique, the details of which can be found in 6.2.

From Fig. 4.3(a), it is clear that the temporal profile of the collector signal is composed of fast and slow-rising parts, which in turn are clear contributions of holes and electrons, respectively. Due to the low mobility of electrons, the collection time of electrons is significantly extended. To achieve complete charge collection with such a detector, the shaping time (or integration time) should be very long, according to the electron transit time, and assuming no electron trapping occurs. However, this is often impractical during the finite collection time for readout electronics. Furthermore, a photon absorbed at different depths relative to a collector will induce different amounts of charge for a given shaping time. As can be observed from the results, the magnitude of the induced charge for the photon interaction happening close to the top electrode is much higher than that of the induced charge, due to an interaction happening close to the collector. This degradation of total induced charge becomes worse when interaction depth gets closer to the collector. Therefore, depth-dependent signal rise time and charge collection leads to a severe ballistic deficit ¹ in the possible application of an a-Se-based photon counting detector [144].

For the unipolar charge-sensing device with a $50\ \mu\text{m}$ grid pitch, however, the pulse shape stays low and rises relatively instantaneously after entering into the near-field region, as shown in Fig. 4.3(b). For example, the rise time for the conventional detector for photon interaction at $0.2\ \text{L}$ is estimated around $30\ \mu\text{s}$, while in the same situation for the unipolar charge sensing device, rise time is a sub-microsecond. Additionally, the magnitude of the

¹Ballistic deficit is the loss of output signal amplitude due to the interplay between the finite charge collection time in a detector and the characteristic shaping time of the amplifier.

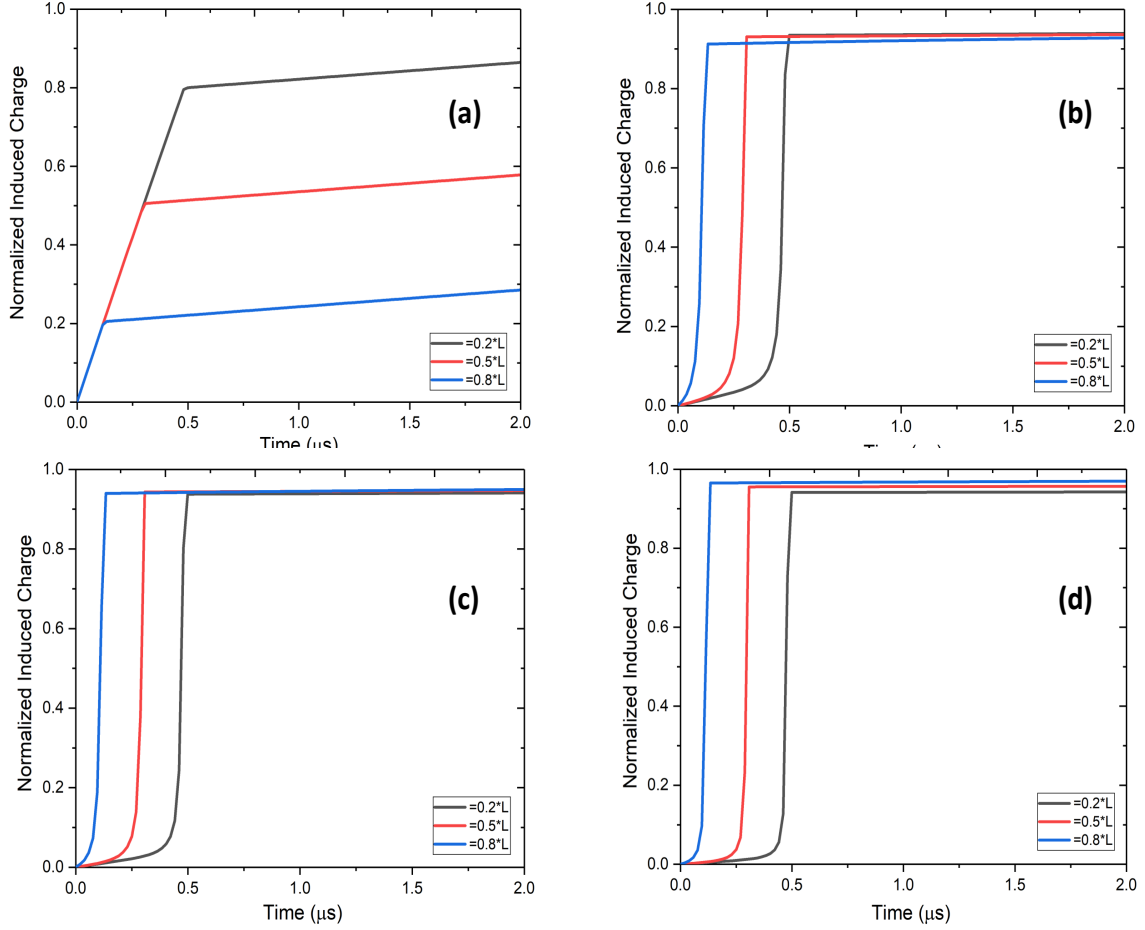


Figure 4.3: Normalized collected charge as a function of time for three interactions depths, 0.2L, 0.5L and 0.8L. (a) simulations are performed for a conventional selenium detector without the grid , (b) a unipolar selenium detector with a grid pitch of 50 μm , (c) 35 μm and (d) 20 μm .

collected charge is close to unity for the shaping time, which is adjusted according to the hole transit time. Note that the improvement of temporal response with the unipolar charge sensing device is twofold: (1) the electron contribution is mostly eliminated from the signal output; (2) only holes passing the grid layer (i.e. in near-field) can contribute substantially

Table 4.1: a-Se parameters used in simulation studies. * indicates the parameters used for simulation studies of a-Se device with a poor electrical properties [3, 4].

	Fabricated in G2N/UW	Reported in literature
Hole mobility, μ_h , ($\text{cm}^2/\text{V} \cdot \text{s}$)	0.147	0.12*, 0.13-0.15
Hole lifetime, τ_h , (μs)	120	8.2*, 50-500
Electron mobility μ_e , ($\text{cm}^2/\text{V} \cdot \text{s}$)	0.004	0.003*, 0.002-0.004
Electron lifetime, τ_e , (μs)	200	100*, 200-1000

to the signal output. Therefore, the shaping time can theoretically even be set for the hole transit time in the near-field region, which primarily depends on the grid-to-collector distance. Fig. 4.3(c) and (d) show the collected charge for the unipolar charge sensing detector with a grid pitch of $35 \mu\text{m}$ and $20 \mu\text{m}$ respectively. The charge collection time decreases, and the temporal response of the detector improves as the grid pitch becomes smaller. This verifies that the shielding for the slower carriers (i.e. electrons), aimed at inducing a significant amount of charge on the collecting electrode, are more effective, and their deleterious effect on the output signal is mitigated by a grid pitch approaching the ideal design, as shown in Fig. 4.1(c). Here, one might question the intrinsic limit of the temporal resolution improvement, because intuitively, it cannot be increased indefinitely. Existing studies have reported that the temporal response is limited alongside the spatial spreading of the radiation-generated carrier packet, which follows Gaussian statistics [50].

4.3.2 Charge collection efficiency

Another way to characterize the uniformity of the detector response as a function of photon interaction depth is to calculate the charge induction efficiency. Regarding optimum detector response, it is expected to achieve a signal output with almost the same amplitude for any photon interaction depth, indicating that the entire photogenerated charge is collected at almost full efficiency. The detector response is independent of photon interaction

depth. To illustrate the improved signal output uniformity achievable through unipolar charge-sensing, we calculated the efficiency for different internal grid pitch ranges (similar to that of fabricated unipolar charge-sensing detectors), as well as for a conventional a-Se detector. The efficiency calculations are also indicative of the limitations that a unipolar charge-sensing device might present. The model used for the efficiency calculation takes into account the uniform trapping effect for both types of carrier. Thus, it demonstrates the effect of a-Se film thickness and electrical properties on detector response.

The charge trapping process should be modelled by the probability density function (PDF), due to its random nature. If we assume that a photon is absorbed at x_1 , and electrons and holes are collected by the top and bottom electrodes, the PDF for electrons and holes trapped at x'_1 and x''_1 , respectively, are given by the following equations [145, 146],

$$p_{top}(x'_1 | x_1) = \alpha' e^{-\alpha'(x_1 - x'_1)}, \quad (4.10)$$

$$p_{bottom}(x''_1 | x_1) = \beta' e^{-\beta'(x''_1 - x_1)}, \quad (4.11)$$

where α' and β' are the linear attenuation coefficients for electrons and holes, respectively, and given by:

$$\alpha' = 1/\mu_e \tau_e F_1, \quad (4.12)$$

$$\beta' = 1/\mu_h \tau_h F_1. \quad (4.13)$$

The polarity of the current induced by both an electron and a hole on any electrode is the same; therefore, the charge induction on any electrode is a contribution of both types of carriers. The collected charge at the bottom electrode, due to the moving hole generated at x_1 , is:

$$Q_{bottom}(x) = \sum_{m=x_1+1}^{N-1} [V_W(x_1) - V_W(m)] [e^{-\beta'(m-x_1)} - e^{-\beta'((m+1)-x_1)}] + e^{-\beta'(L_1-x_1)} [V_W(N) - V_W(x_1)], \quad (4.14)$$

and similarly, for the top electrode, due to a moving electron generated at x_1 is:

$$Q_{top}(x) = \sum_{m=1}^{x_1-1} [V_W(x_1) - V_W(m)] [e^{-\alpha'(x_1-(m+1))} - e^{-\alpha'(x_1-m)}] + e^{-\alpha'(x_1)} V_W(x_1), \quad (4.15)$$

where $\Delta x_1 = L_1/N$ is the uniform step-size and N is the number of spatial divisions. The discrete point $x_1 = x_i \Delta x_1$, where x_i is an integer from 1 to N . The weighting potential (V_W) is considered to be constant within each step. Then, the total collected charge at the pixel electrode due to EHP generated at x_1 is given by:

$$g_4(x_1) = Q_{grid}(x_1) + Q_{top}(x_1). \quad (4.16)$$

The results of charge collection efficiency calculation for 70 μm -thick selenium operated at 8 $\text{V}/\mu\text{m}$ for two different a-Se films with different electrical properties, are plotted in Fig.4.4. The a-Se film properties (summarized in Table 4.1) used for this calculation are that of one fabricated at G2N/University of Waterloo, as well as one with electrical properties adapted from the literature, and indicating poor a-Se film quality. The sample with poor electrical properties suffers from low hole-lifetime; therefore, we expect that time response for a unipolar charge-sensing device may be limited. The intention is to indicate the possible limitations that will be imposed on a unipolar charge-sensing device due to poor hole transport. Employing a-Se with high electrical quality, on the other hand, will help us to reveal intrinsic temporal response limitations of an a-Se-based unipolar charge-sensing device.

In Fig.4.4(a), the highly non-uniform response of a conventional detector with our a-Se layer can be attributed to poor electron transport properties. The downward curvature of charge induction efficiency at the collecting electrode side is obviously a result of electron trapping. Photogenerated electrons at this side need to travel a longer distance, but some may become trapped due to their shorter Schubweg, prior to reaching the top electrode. On the other hand, we observed that the response for the unipolar charge sensing device was quite uniform, because the detector response only relied on the hole transport, and it continued to improve with a smaller grid pitch. The small curvature on the collecting

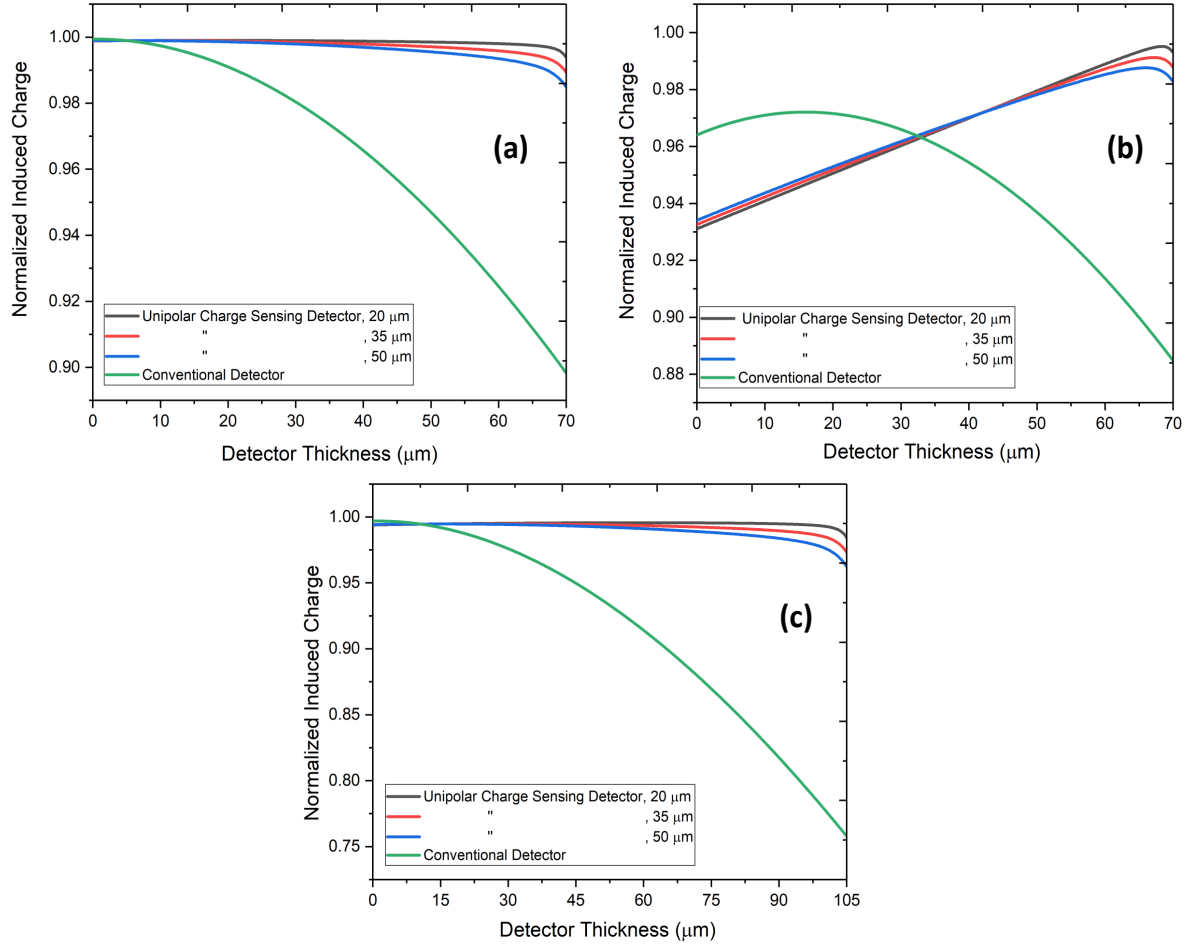


Figure 4.4: Calculated charge induction efficiencies as a function of thickness for two different a-Se detector with a different charge transport properties as shown in Table 4.1, a) simulated for the electrical parameters of the fabricated device (for $d_{a-Se} = 70 \mu m$), b) simulated for the poor transport properties of an a-Se device reported in the literature (for $d_{a-Se} = 70 \mu m$), and c) simulated for the electrical parameters of the fabricated device (for $d_{a-Se} = 105 \mu m$).

electrode side is due to the photon absorptions that happen in the near-field region; hence, photogenerated electrons induce a degree of signal on the collecting electrode. However,

some of them become trapped before reaching the top electrode. This is a minor effect on the output signal of the unipolar charge-sensing device, because the likelihood of having photon absorption in the near-field region is quite low, due to the relatively small region.

Regarding the other device with poor electrical properties, the detector response suffers from even hole- trapping, particularly for events that occur close to the top electrode (Fig.4.4(b)). Due to the Schubweg of the holes being degraded due to short hole-lifetime, some of the holes become trapped before being collected by the collecting electrode. This poor hole-lifetime effect extends further into the unipolar charge-sensing device. This happens because the charge induction with the unipolar charge-sensing relies primarily on hole transport. Since some of the holes become trapped prior to reaching the collecting electrode, the induced charge signal is lower than what would result if only holes passed completely through the grid layer, and were collected by the collecting electrode. We should state that the simulations herein were performed for our fabricated device, which only has a 70- μm -thick a-Se. For example, when the detector thickness is increased by only 50%, the charge induction efficiency drops to 75%, as shown in Fig.4.4(c). Given that the a-Se thickness employed for regular mammography detectors is roughly 200 μm , the non-uniformity in the detector response of conventional a-Se detectors may be further exacerbated. Charge induction efficiency can be additionally improved with a higher applied voltage; however, the improvement comes at the expense of a higher dark current, if a proper hole-blocking layer is not employed.

4.3.3 Energy resolution

Some medical imaging procedures, such as dual energy subtraction for mammography, requires measuring energy distribution of the incident radiation [147, 148, 149]. For such procedures, the performance of the radiation detectors is commonly defined by their ability to resolve the energy distribution or spectral information of transmitted X-ray or gamma-ray photons through the object of interest that is being imaged. The energy spectrum measured by the detector is called the response function of the detector for the energy

used in determination. Note that this definition is applicable to all types of radiation detectors used in other applications such as gamma-ray astronomy, nuclear spectroscopy, and non-destructive testing.

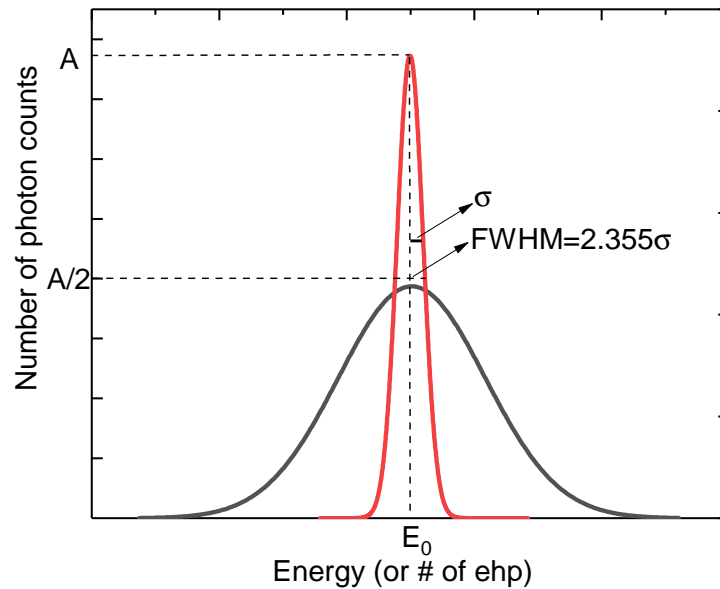


Figure 4.5: Examples of energy spectrum. Good energy resolution (red) and poor energy resolution (black) are provided for comparison.

The energy resolution of the detector is characterized by its response to the mono-energetic source of the radiation. Ideally the response should be a mathematical delta function; however, in reality, it is described by a Gaussian distribution, due to a level of noise added by the electronic system, as well as a statistical error that results from fluctuation from pulse to pulse, even for the same deposited energy for each event. When the fluctuation is smaller, the response function of the detector will be narrower when approaching a delta function. Fig.4.5 shows two response functions of two different detectors with superior and inferior performance, or good resolution and poor resolution, respectively. Given that the same number of photons are absorbed by the detectors, the areas under the spectrums should be equal. Despite the fact that both distributions are

centered at the same mean value, E_0 , the distribution obtained by the detector with poor resolution is much wider, which demonstrates the inability of such a detector to resolve specific details pertaining to the incident energy of the radiation. The most commonly used energy resolution metric is the full-width at half-maximum (FWHM), as defined by [144]:

$$\text{ER} = \frac{\Delta E}{E_0} \times 100\%, \quad (4.17)$$

where ΔE denotes the FWHM of the full energy peak in the measurement, and E_0 is the peak center or photon energy that is being measured. If we assume the formation of charge carriers follows the Poisson process, and a total number of N charge carriers are created on average, the expected inherited statistical fluctuation is given by the standard deviation, \sqrt{N} . Under this assumption, if this is the only source of fluctuation in the signal and N is a large number, the response function of the detector can be modelled by a Gaussian function as follow [144]:

$$G(E) = \frac{A}{\sigma\sqrt{2\pi}} e^{-\frac{(E-E_0)^2}{2\sigma^2}}, \quad (4.18)$$

$$\text{FWHM} = 2\sqrt{2\ln 2}\sigma \approx 2.355\sigma, \quad (4.19)$$

where A represents the area and σ is the standard deviation.

The response of many detectors is approximately linear, so that the average amplitude of pulse is equal to $E_0 = KN$, where K is a proportionality constant. Then, the standard deviation σ of the peak in the pulse-height spectrum is $\sigma = K\sqrt{N}$, and its FWHM is $2.355K\sqrt{N}$. Therefore, the energy resolution can be expressed as [144]:

$$\text{ER}_{\text{Poisson Limit}} = \frac{2.355K\sqrt{N}}{KN} = \frac{2.355}{\sqrt{N}}. \quad (4.20)$$

This equation implies that the energy resolution achievable is limited by the total number

of generated charge carriers. For example, to achieve an energy resolution below 1%, more than 55000 EHP must be generated by a photoconductor. This theoretical calculation indicates that an ideal detector should generate as many EHPs per event as possible, so that the energy resolution limited by the total number of EHP generated is as low as possible. However, careful measurements and maintaining system noise at the lowest possible level, and achieving an intrinsic response with some form of radiation detectors, have shown that energy resolution, at least an order of magnitude better than that predicted by the statistical argument given above, is achievable. These results state that the process that leads to the formation of each charge carrier is not independent, and cannot be modelled by simple Poisson statistics. To address this issue, Fano factor, F , was introduced to quantify the difference between the statistical fluctuation defined by the Poisson process, and that obtained through experimentation, and this difference is defined as [150]:

$$F = \frac{\text{observed variation in } N}{\text{Poisson predicted variance}(= N)} = \frac{\mu}{\sigma^2}. \quad (4.21)$$

If we re-arrange the energy resolution formula by adding Fano factor, F , then:

$$\text{Energy Resolution}_{\text{Poisson Limit}} = \frac{2.355K\sqrt{N}\sqrt{F}}{KN} = 2.355\sqrt{\frac{F}{N}}. \quad (4.22)$$

The energy resolution is scaled by a factor of \sqrt{F} . The energy resolution of scintillator detectors primarily follows Poisson statistics, with a Fano factor of unity. However, the energy resolution of most semiconductor detectors is better than what would be defined by Poisson statistics with a Fano factor much lower than unity. For example, Fano factor for CZT and silicon detectors has been measured at 0.089 and 0.01, respectively, indicating that an excellent energy resolution can be achieved with such detectors [151, 152].

A pulse-height measurement system should ideally measure the same amplitude of pulses for the same deposited photon energy. However, this is never practically possible, due to the presence of several noise and interference sources in the detector and the

measurement system. These include any drifting of the detector operation characteristics, electronic noise, and the statistical fluctuations that stem from the discrete nature of the measured signal. Two main sources of statistical fluctuation are: 1) when not all deposited photon energy is used for the generation of free charge carriers, and some of the energy is lost due to vibration in the crystal; 2) some of the generated charge is lost due to trapping and recombination, and hence, cannot be collected. Statistical noise is the dominant source of noise in most radiation detectors, and defines the minimum limit of detector performance achievable. Provided the noise sources are systematic and independent, the overall response function always tends toward a Gaussian shape, even if some of them are characterized by the distribution of other functions, according to statistical theory. Therefore, the total FWHM of the detector response can be found by quadrature of a selection of the FWHM values of each individual source of fluctuation, as shown below:

$$(\text{FWHM})_{\text{overall}}^2 = (\text{FWHM})_{\text{statistical}}^2 + (\text{FWHM})_{\text{noise}}^2 + (\text{FWHM})_{\text{drift}}^2 + \dots \quad (4.23)$$

4.3.4 Swank noise

The statistical fluctuation in the number of EHPs generated per absorbed photon is quantified by the Swank factor, I , also known as the information factor [153, 154]. The Swank factor is related to detector quantum efficiency (DQE) at zero spatial frequency, as per the following expression:

$$\text{DQE} = \eta(E)I(E), \quad (4.24)$$

where η is the quantum efficiency of the detector as a function of thickness and energy. The Swank factor is defined as [14]:

$$I = \frac{M_1^2}{M_0 M_2'}, \quad (4.25)$$

where M_n is the n^{th} moment of the detected EHP and defined by:

$$M_n = \sum_x p(x)x^n, \quad (4.26)$$

where the variation in x (number of detected EHPs) is given by the probability distribution, $p(x)$. Alternatively, the Swank factor can be calculated by the definition of the mean and standard deviation of a distribution when the detector response consists of a single photo-peak:

$$\mu = \frac{M_1}{M_0}, \sigma^2 = \frac{M_2}{M_0} - \left(\frac{M_1}{M_0}\right)^2, \mu^2 = \frac{\mu^2}{\mu^2 \sigma^2}. \quad (4.27)$$

The Swank factor approaches unity for $\sigma \ll 1$. The Swank factor is an important measure, because it can be used to identify the lowest achievable energy resolution (i.e. intrinsic energy resolution) when other factors affecting the width of the energy spectrum are suppressed, especially the collection efficiency.

4.3.5 Monte Carlo simulation

Monte Carlo modelling of a-Se detectors can provide insight into the fundamental limitations of energy resolution, as defined by material intrinsic properties such as Swank noise, trapping, and recombination limited charge collection efficiency. The spectral response of our conventional a-Se detector was simulated using varying applied electric fields, using mono-energetic gamma-ray sources at two different energies, 59.5 keV (^{241}Am) and 122 keV (^{57}Co), which were also used for our experimental PHS measurements. The simulated PHS results were utilized to identify the intrinsic properties of an a-Se photoconductor, such as Swank factor and energy resolution, without the extra noise added by the front-end electronic and dark current. A comparison between the simulation and our experimental results using Gaussian fitting enabled us to understand the effect of the system noise on the broadening of the spectrum.

Various functions were implemented by the simulation model to define the physics of the photon-absorption to charge-collection process [12]. The photon interactions processes,

such as photoelectric effect, as well as secondary electron interactions in the presence of an applied electric field, were modeled by PENELOPE [155]. Then, the detailed transport code, ARTEMIS, was used to simulate the three-dimensional spatial and temporal transport of EHPs and pulse-height spectra response. The Monte Carlo simulation model to some extent incorporated the effects of recombination and trapping on EHP transport. The detailed steps implemented for the Monte Carlo simulation framework process is shown in Fig. 4.6 [12, 156].

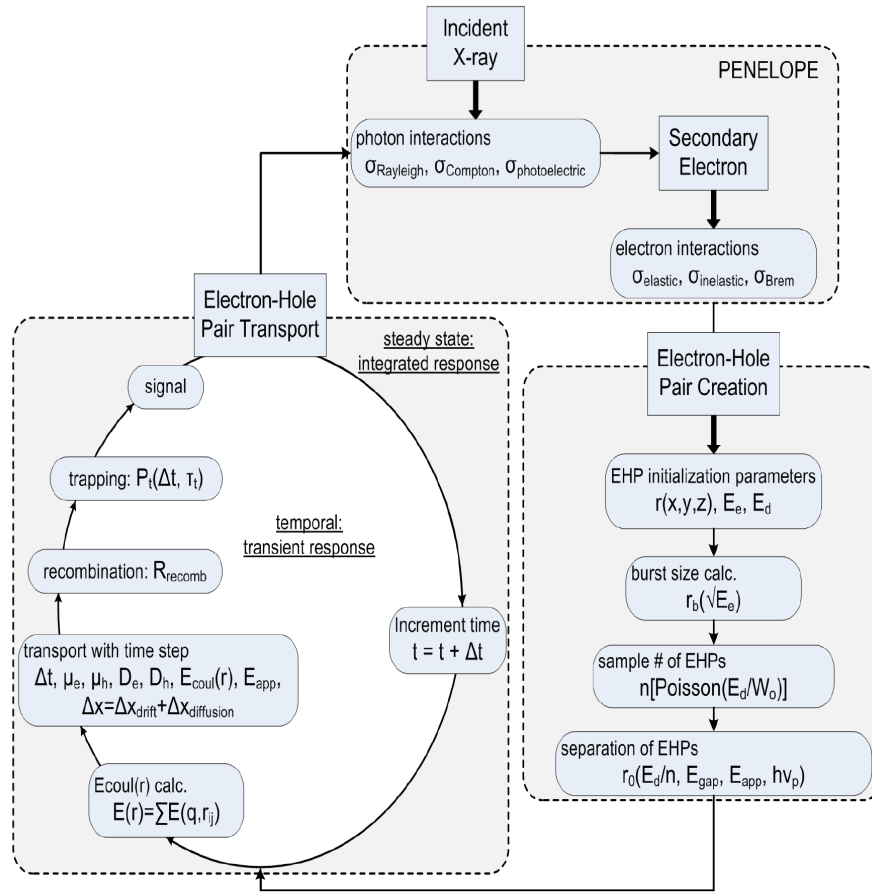


Figure 4.6: Flow chart for the Monte-Carlo simulation of the signal formation process in amorphous selenium x-ray detectors [12].

Fig. 4.7 illustrates the simulated pulse-height spectra for both mono-energetic gamma-ray sources as a function of applied electric field. The x-axis shows the number of electron-hole pairs created for the incident photon energy. The y-axis represents an event count for a fixed measurement time. All PHS consisted of two spectral peaks; the highest energy peak at the right corresponds to incident photon energy, and the lower energy peak occurred due to the generation and escape of K-edge fluorescent photons (12.6 keV). In addition, we observed continuous lower energy counts as a result of Compton scattering.

The results indicate that W decreases and detected EHP increases as the electric field increases. For example, the detected EHPs is 721 and 1931 for the applied field of $5 \text{ V}/\mu\text{m}$ and $20 \text{ V}/\mu\text{m}$, with ^{241}Am , respectively. This was expected, because the carriers Schubwegs are longer, thus trapping is less likely and more EHPs are collected. The number of EHPs also increases when incident photon energy is increased, thereby depositing more energy and leading to the generation of more charge carriers. Fig.4.7(b) and (d) show the Gaussian fitted curves for the PHS spectra for both incident photon energies at $10 \text{ V}/\mu\text{m}$. Each PHS is obtained for a different applied field, and incident photon energy is analytically fitted. Then, the Gaussian mean and variance, energy resolution, and Swank factor are calculated, as shown in Table 4.2. This fitting ignores the lowest energy peak resulting due to K-edge. As the electric field increases, the mean number of detected electron-hole pairs and its variance increases. Although FWHM (2.35σ) values are larger for a higher applied electric field, energy resolution improves for a higher applied field, which can be attributed to a larger number of collected EHPs (equation 4.20). The simulated Swank factor in all cases is higher than 0.99, due to very low variance in the Gaussian fitted curves. However, Gaussian fitting does not take into account Compton scattering, or K-fluorescent photon generation or escape. Existing studies have shown that a significant difference between the calculated Swank factor is observed when these effects are considered [12]. When we calculated the variance for the entire PHS distribution, the Swank factor was found to be lower than 0.65. Some of the calculated results in Table 4.2 are plotted in the next section, and compared with our experimental results.

The energy resolution of a unipolar charge-sensing device had previously been simu-

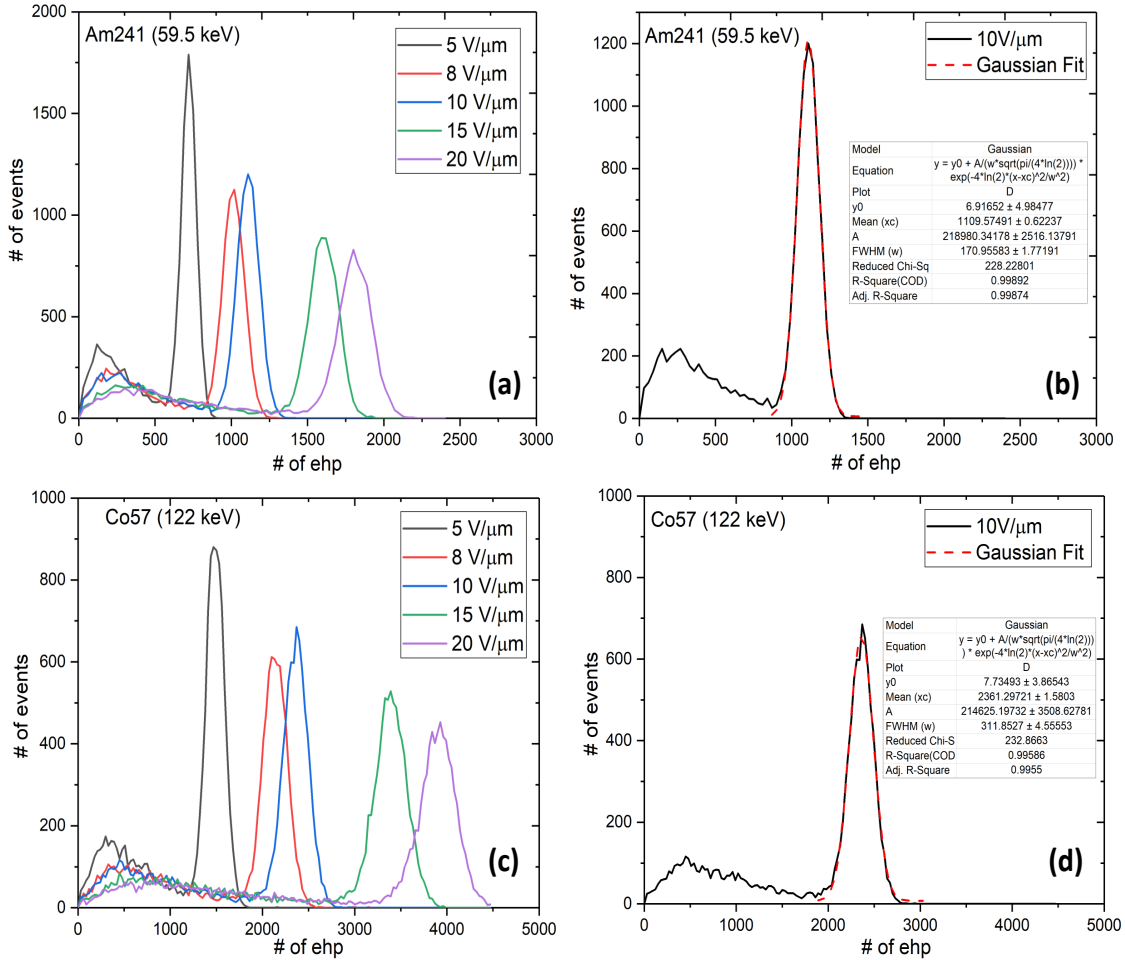


Figure 4.7: Simulated pulse-height spectra for mono-energetic gamma-ray sources a) for ^{241}Am and c) for ^{57}Co as a function of applied electric field, b) and d) demonstrate some of the Gaussian fitted curves (at 10 V/μm) to calculate the parameters in the Table 4.2.

lated using an analytical model by Stavro et. al [15]. Significant improvement in energy resolution was reported for such a detector, with an energy resolution of 10 keV when the detector was exposed to an ^{241}Am gamma-ray source. This improvement is attributed to complete charge collection (i.e., holes) and reduced electronic noise. In the next section, we report the results for the fabricated a unique unipolar charge-sensing detector and

empirically investigate energy resolution. Our measurement results match the simulation results at a 10% to 15% error rate, which may have been due to a number of reasons, such as different a-Se film properties and an imperfect gamma-ray source, which has several emission energies, unlike the perfect mono-energetic source used for simulations.

It should be noted that there was a small number of limitations to the Monte Carlo code used for this study. First, the currently available code only considers the deep trapping of carriers with a constant carrier lifetime. Shallow traps, carrier-releasing from the trap center, and trap-filling effects are not included in the trapping model. These events have a significant effect on EHP transport, and therefore also on the collection efficiency and temporal response of the detector. Second, the detector thickness used for this simulation study was only 70 μm , the same as what we fabricated for experiments. As discussed in the previous sections, the carrier transit time in a-Se is directly proportional to its thickness. For a thicker a-Se detector, the probability of the carrier trapping increases, and the spectrum becomes broader. However, considering the electrical parameters of the a-Se used for this simulation (Table 4.1), and the given film thickness, the generated charge was collected at almost full efficiency. For this reason, the significant effect of charge trapping on spectrum broadening can almost be ruled out, because Swank factors were found very close to unity with the simulation study. Despite these limitations, we adopted this Monte Carlo simulation package because, unlike analytical models, it allowed us to simulate detector pulse-height spectra response by considering three-dimensional spatio-temporal carrier transport in a-Se.

4.4 Conclusion

In this chapter, we investigated the temporal and energy resolutions of conventional and unipolar charge sensing a-Se detectors. The simulation results indicate the poor electron transport properties in a-Se as the primary cause of degraded temporal and energy resolution when using a conventional a-Se detector. Signal rise-time on the collecting electrode

Table 4.2: Calculated parameters of conventional a-Se detector based on the Monte-Carlo simulation results

Gamma-ray Sources	Applied Field	W_{\pm} (eV)	σ (EHP)	Energy Resolution (keV)	Swank Factor
Am241 (59.5 keV)	5 V/ μm	82.5 ± 0.61	58.9 ± 1.6	11.4	0.9933
	8 V/ μm	58.7 ± 0.46	72.3 ± 1.3	10	0.9949
	10 V/ μm	52.1 ± 0.62	79.6 ± 1.2	9.7	0.9950
	15 V/ μm	37 ± 1.04	94.8 ± 1.9	8.3	0.9965
	20 V/ μm	30.8 ± 1.29	108.6 ± 3.8	7.9	0.9968
Co57 (122 keV)	5 V/ μm	82 ± 1.03	99.5 ± 1.29	19.1	0.9954
	8 V/ μm	57.1 ± 1.2	131 ± 1.35	17.5	0.9962
	10 V/ μm	51.6 ± 1.5	137 ± 1.8	16.6	0.9965
	15 V/ μm	35.9 ± 0.98	166.3 ± 4.7	14	0.9975
	20 V/ μm	31.2 ± 1.3	181.7 ± 8.5	13.2	0.9978

for single photon absorption varied when utilizing a conventional a-Se detector, depending on the photon interaction depth resulting from a portion of the signal induced by an electron. For the same reason, when a conventional a-Se detector was used for pulse-height spectroscopy measurements, an asymmetric long tail to the left of the photopeak in the measured energy spectra formed, and the energy resolution deteriorated. To circumvent the deleterious effect of electron transport, we introduced a unipolar charge sensing device, which has an internal grid and is operated according to the same principle of a Frisch grid device, invented for gaseous detectors. The main notion here is to create a near-field effect within the proximity of collecting electrode, so that the detector only acquires a signal induced by holes, which will have better electrical transport properties than electrons. The theoretical results show that the temporal resolution of employing a-Se detectors with a unipolar charge-sensing method can be substantially increased. Additionally, it is indicated in the literature according to simulation results that when such a detector is employed for energy spectrum measurements, energy resolution of 10 keV at 59.5 keV can be achieved, while our calculation for a conventional a-Se detector indicated an energy resolution of 9.7

keV at an applied field of $10 \text{ V}/\mu\text{m}$, when no electronic or dark current noises existed.

Chapter 5

Fabrication and Experimental Characterization of Unipolar Charge Sensing Detector

5.1 Introduction

Considerable research effort has been dedicated to investigating wide band-gap and room temperature operated polycrystalline and amorphous photoconductors as viable alternatives to their single-crystalline counterparts [157, 23, 158, 159, 160, 161]. Among the various materials studied, amorphous selenium (a-Se) has undergone the most extensive development and has been commercialized for some of its X-ray imaging applications, such as mammography and tomosynthesis [23, 131, 162]. A-Se is a direct conversion photoconductor capable of very high spatial resolution that can enable early detection of calcification in the breast, which is an early warning of cancer. It also offers cost-effective and reliable coupling to large area readout circuitry. A-Se in conventional detector structure, however, cannot be leveraged for photon counting imaging applications, such as contrast-enhanced spectral mammography, where higher spatial resolution could confer significant diagnostic

advantages over current technology (e.g., based on CdTe and Si technology). Use of a-Se for photon counting imaging could also enable implementation of large area photon counting imagers, which is currently limited with existing sensor materials such as CdTe and CZT because of cost and yield issues associated with growth and bonding technology. A-Se photon counting imagers could achieve X-ray dose reduction, as well as energy discrimination for better contrast. The root of the problem is poor carrier transport properties, more specifically low electron mobility. Slow electron transport leads to depth-dependent signal variation and slow signal rise-time, as investigated in the previous chapter.

Interestingly, poor charge carrier properties of a-Se hinder its application for dynamic imaging, such as micro-angiography operated with energy integrating detectors. The reason is that despite the considerable progress that has been shown in the material development, the charge transport properties of a-Se are still far from optimal for high frame rate imaging applications. While the charge collection efficiency for holes is quite adequate, the collection efficiency for electrons is severely degraded due to the high density of energy distributed defect states, which causes trapping of some drifting carriers through the photoconductor layer. Release of these trapped carriers gives rise to a transient decaying current, also known as a photocurrent lag, for several seconds after the cessation of X-ray pulses. Such decaying current is superimposed to the subsequent output pulses, making the resulting image inaccurate. Increased lag degrades the temporal response and makes a-Se detectors impractical for real-time imaging today. Although the performance of energy integrating detectors is limited because of incorrect energy weighting and poor noise rejection compared to that of photon counting imagers, most currently deployed medical diagnosis and industrial non-destructive testing imaging systems are based on energy integration technology due to the availability of cost-effective TFT arrays and successful coupling of a scintillator layer to these TFT panels.

Several methods have been devised to address the poor temporal resolution problem of semiconductors having poor charge transport issues (e.g., CdTe and a-Se). The most used methods involve preferential sensing of the charge carriers with higher mobility and lifetime product, avoiding the contribution of slow carriers on the formation of the charge signal.

In this configuration, the effect of the trapping in the output signal is limited and can be mostly compensated by either some electronic manipulation techniques (e.g., pulse rise discrimination and pulse correction) or a particular electrode design [59, 163, 164, 165, 166, 167]. Such localized single polarity sensing with an electrode design has been implemented for a-Se detectors by two main methods in the past. The electron contribution can be minimized by placing the internal grids around the collecting electrode (as shown in the previous chapter). Alternatively, the charge signals induced by the uncollected electrons can be electronically subtracted from the total output signal [168]. The latter approach is employed in the coplanar-grid devices, while the former is used in the solid-state Frisch grid architecture. Regardless of the structure type, the main purpose is to establish a strong near field effect and electrostatic shielding in the proximity of collecting electrodes. Hence, the measured pulses from the detector are based on only the movement of holes in the near-field region, and the signal output is no longer affected by electron movement, trapping or de-trapping in the bulk of the detector. For example, one version of the solid-state Frisch grid device architecture was previously implemented, and considerable temporal resolution improvement was reported [50]. However, the structure was not practically feasible due to the charge injection from the grid layer to the bulk of the a-Se layer at higher fields. Therefore, the device was operated at very low applied electric field compared to the electric field used for commercial a-Se detectors (typically $10 \text{ V}/\mu\text{m}$). As discussed in Chapter 2, charge generation and collection efficiencies of a-Se detectors are highly dependent on the applied electric field.

In this chapter, we investigate the effect of single polarity charge sensing on the temporal performance of a-Se pixelated detectors using novel solid-state unipolar charge sensing device architecture fabricated using photolithography and film evaporation techniques. This scalable and manufacturable new design has several notable advantages. First, the measurement electronics are simpler since a conventional single-amplifier system can be used. Second, the electronic noise will be reduced because the noise contribution from one of the two amplifiers required in the co-planar grid technique is eliminated. This new device architecture uses a combination of higher dielectric strength materials to prevent charge

injection while operating the device at a practical electric field. Moreover, the octagonal internal grid achieves more effective unipolar charge sensing because it covers more area on the collecting electrode compared to the previously fabricated solid-state Frisch grid device (e.g., 1-D design).

Pulse-height spectroscopy setup with a lower system noise is designed to investigate temporal resolution of both conventional and unipolar charge sensing detectors. Rise-time, ionization energy and energy resolution of both types of detectors are measured with common gamma-ray radiation sources such as ^{241}Am and ^{57}Co . The experimental setup for exploring photocurrent lag is also implemented, and detailed analysis in a-Se is carried out to determine its feasibility for dynamic X-ray imaging applications when an a-Se detector is operated with a unipolar charge sensing regime.

5.2 Design and fabrication of the unipolar charge sensing detector

To overcome the low temporal resolution problem with a-Se, we have fabricated pixelated unipolar charge sensing detectors using a standard lithography process. Three types of detectors were fabricated with a various pixel pitch, (i.e., $20\ \mu\text{m}$, $35\ \mu\text{m}$, and $50\ \mu\text{m}$). The pixel pitch (or diameter of the opening in the grid layer) of the detectors is determined based on a few criteria. As investigated in the previous chapter with the weighting potential simulations, a smaller grid pitch is desired to achieve more effective shielding of the slow charge carriers so that they do not induce a considerable charge on the collecting electrode. Therefore, we decided to fabricate an array with the smallest possible pixel pitch, which is defined by the electrical quality of the dielectric layers and fabrication procedures. The dielectric layer should be thick enough to prevent discharge and electrical breakdown. Given the limitations, we found $20\text{-}\mu\text{m}$ pixel pitch as the smallest pixel size that can be fabricated reliably. The other detectors with larger pixels are also fabricated for comparison purposes. Details (e.g., number of pixels) of the fabricated detector arrays are given in

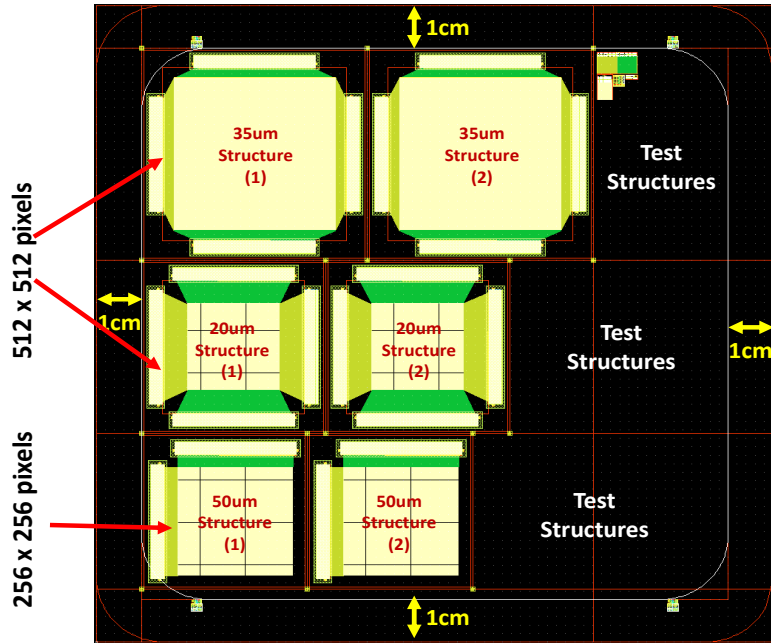


Figure 5.1: A total of 6 detector arrays with a various pixel pitch were fabricated on a single glass substrates. The pixel pitch of the detectors are $20\ \mu\text{m}$, $35\ \mu\text{m}$ and $50\ \mu\text{m}$.

Fig. 5.1. A single-pixel structure consists of molybdenum (Mo) collecting electrode and an octagonal-shaped chromium (Cr) metal grid that is buried into silicon-nitride (SiN_x) and polyimide (PI) insulating layers. Top and cross-sectional views of the single pixel structure employed for all detector arrays are shown in Fig. 5.2. SiN_x and metal layers were patterned with photolithography and a wet-dry etching process using five different photomasks. Some parts of the device fabrication were carried out by our collaborators at Advance Display Research Center at KyungHee University.

After the photolithography process, a thin PI layer ($500\ \text{nm}$) is spin-coated onto the pixelated substrates to serve as a passivation layer on the SiN_x layer. The PI layer in the detectors used for pulse-height spectroscopy experiments are not etched because the amount of the radiation absorbed by the detectors is insignificant; thus, no charge accumulation is expected at the PI/collecting electrode interface. However, we etched the

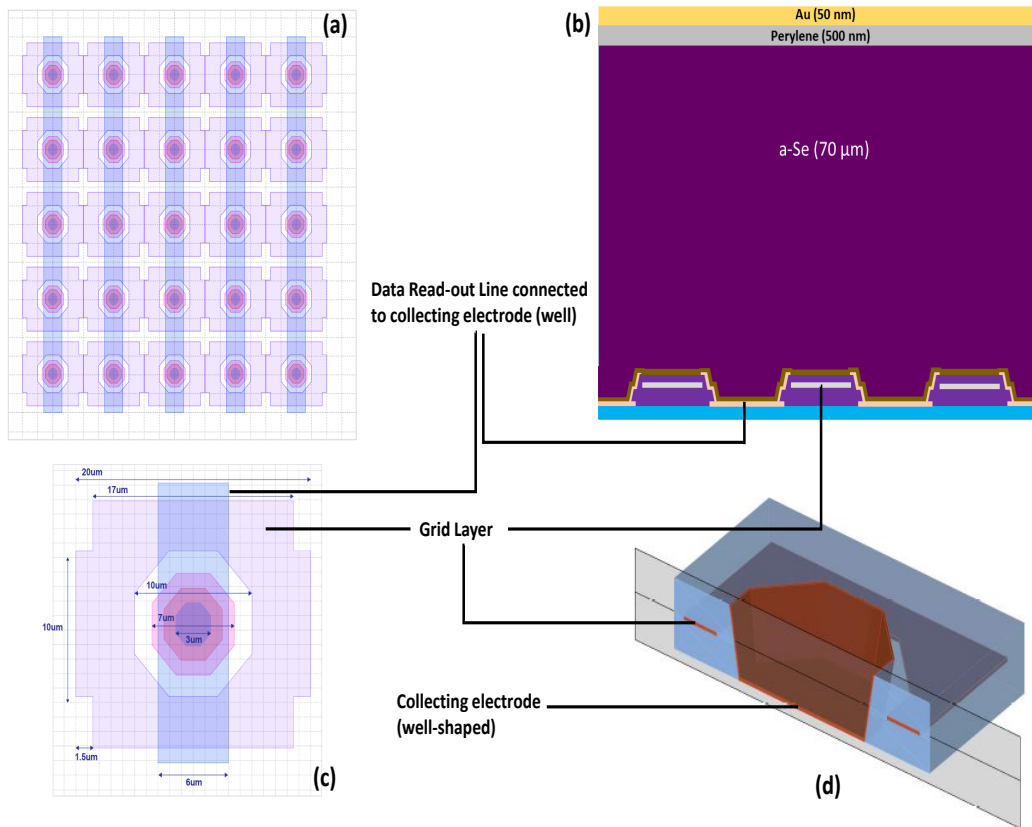


Figure 5.2: Schematic representation of a) the pixel array and c) a single pixel, b) cross-section of the unipolar charge sensing detector (2-D) and d) single pixel (3-D).

PI layer on the detectors (with Mask-5) used for the real-time photocurrent lag measurement because of the higher amount of radiation absorbed. PI prevents stress-induced crystallization and helps to passivate imperfect surface states of SiN_x by forming a good interfacial layer between SiN_x and amorphous selenium film. Stabilized a-Se layers with a thickness of 50- μm and 70- μm are thermally evaporated on the arrays used for photocurrent lag and pulse-height spectroscopy experiments, respectively. The hole blocking layer (perylene-tetracarboxylic-bisbenzimidazole (PTCBI) or perylene) and top metal electrode are deposited on the a-Se layer to provide the bias electric field for image charge collection. For the photocurrent lag measurements, the perylene layer is replaced with a PTCBI layer

to allow high-frequency device operation. One of the fabricated detectors (before and after evaporation of the a-Se layer) and part of its micro-graph are shown in Fig. 5.3. Details of the fabrication flow are explained in Fig. 5.4. Single-pixel conventional a-Se devices are also fabricated with different hole blocking layers for comparison purposes, similar to that of devices fabricated for the investigation of the hole conduction mechanism in the PI layer (shown in Fig. 3.1).

This unipolar charge sensing device structure differs from a previously fabricated solid-state Frisch grid architecture in that there exists a non-uniform electric field strength across the near-field region with a stronger field near the wall of the well and weakest at the center [169, 170, 171, 172]. The non-uniform electric field creates a local hot-spot electrical breakdown on the dielectric material and consequently induces excessive charge injection to the bulk of the photoconductor, making the detector impractical, especially for low dose imaging applications. In this unique design, however, the formation of a non-uniform electric field is avoided. As such, the highest electric field region is particularly formed on the top surface of the dielectric layer, where some fabrication methods can control the thickness and the uniformity. Critical to its feasibility to operate the device with a high electric field without an excessive charge injection, the optimal thickness of an insulating layer is determined based on simulation results and practical limitations with the fabrication procedures. For instance, Fig. 5.16 depicts the simulated electric field distribution at the surface of the insulating material, where the highest electric field strength is estimated around $70 \text{ V}/\mu\text{m}$ for one detector with a $20\text{-}\mu\text{m}$ pixel pitch, when the top and grid electrodes are biased to 500V and 80V , respectively. Almost all the electric field lines are terminated on the collecting electrode with this bias configuration indicating no charge immobilization is observed on the dielectric material, and hence, no sensitivity reduction due to incomplete charge collection is expected. Note that the required grid voltage is found to be lower for the detectors with a smaller pixel pitch (see section 5.4.2). For example, for the same device configuration (e.g., same a-Se thickness) and internal electric field ($8 \text{ V}/\mu\text{m}$), the grid voltage for the unipolar charge sensing detector with a $50\text{-}\mu\text{m}$ grid pitch is 165V while 135V is required for the same detector having a $35\text{-}\mu\text{m}$

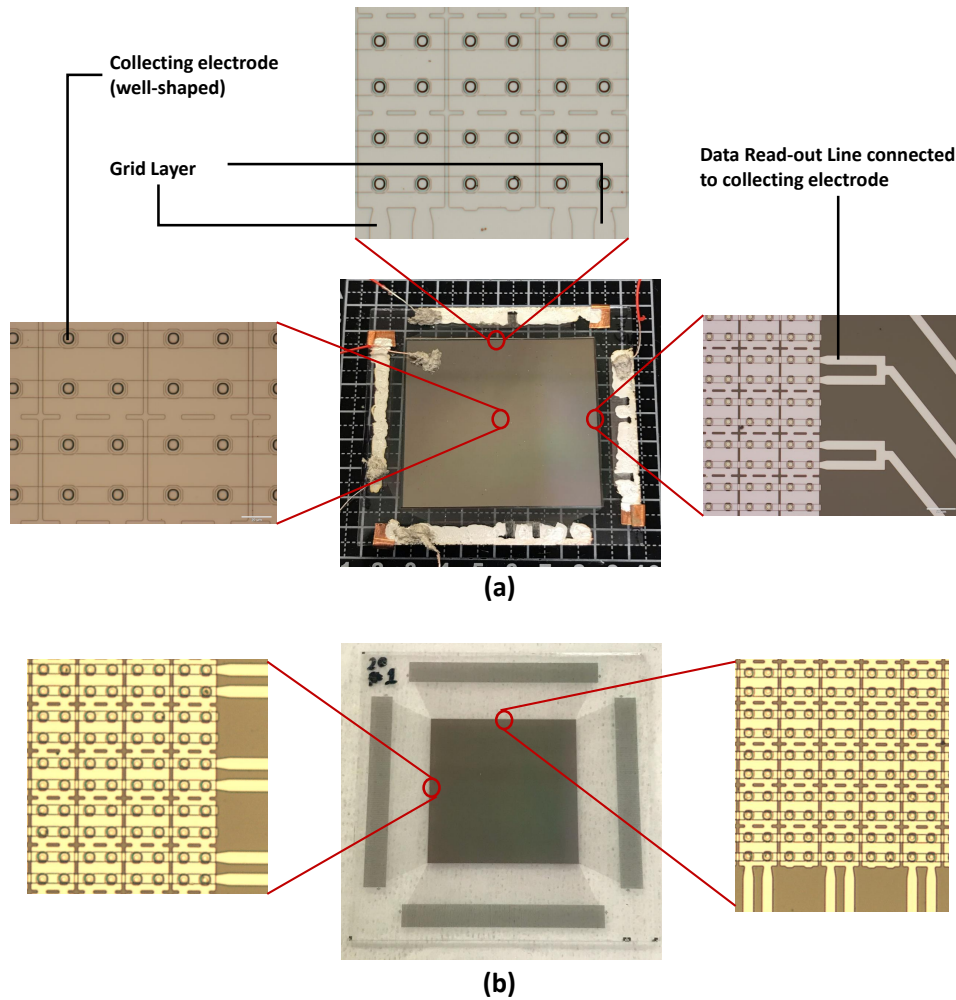
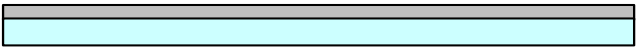
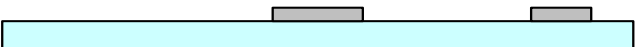


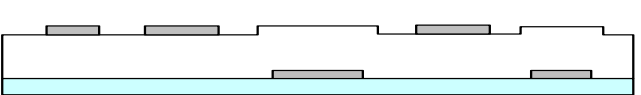
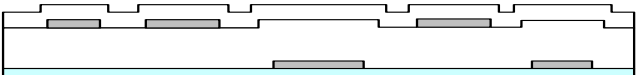
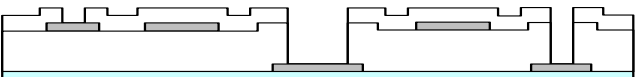
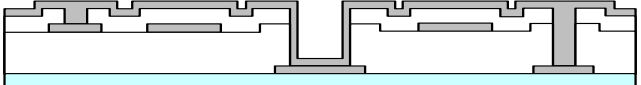


Figure 5.3: Fabricated unipolar charge sensing detectors and part of their micrograph (a) with and (b) without evaporated selenium.

grid pitch. The thickness of the SiN_x layer is, therefore, determined based on the larger pixel, which requires the highest grid voltage. Given the limitation and imperfection with our PECVD system, the dielectric strength of the fabricated SiN_x film is estimated around 3MV/cm although much higher values can be found in the literature. This empirical result suggests employing at least 500 nm thick SiN_x between the grid and collecting electrode to

<p>1st Step Data Readout-line Deposition</p>		<p>100-nm Molybdenum is thermally evaporated</p>
<p>2st Step Data Readout-line Patterning</p>		<p>Wet-etching with Mask#1 See Fig.7a</p>
<p>3st Step Dielectric-layer Deposition</p>		<p>SiN_x deposition 600-nm With PECVD</p>
<p>4st Step Metal-grid Deposition</p>		<p>100-nm Chromium is thermally evaporated</p>
<p>5st Step Metal-grid Patterning</p>		<p>Wet-etching with Mask#2 See Fig.7b</p>
<p>6th Step Dielectric-layer Deposition</p>		<p>SiN_x deposition 600-nm With PECVD</p>
<p>7th Step Open via to collecting electrode</p>		<p>Dry-etching with Mask#3 See Fig.7c</p>
<p>8th Step Collecting-electrode Deposition (well-shaped)</p>		<p>200-nm Molybdenum is thermally evaporated</p>

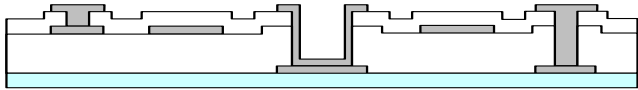
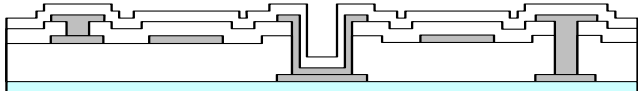
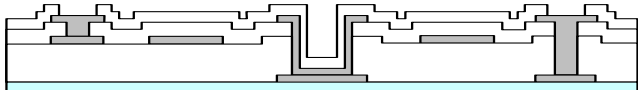
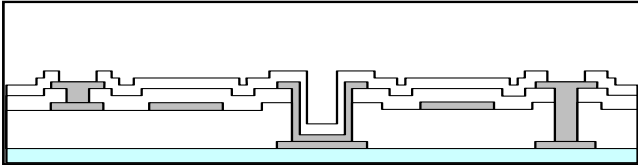
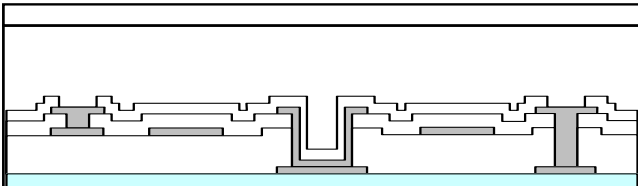
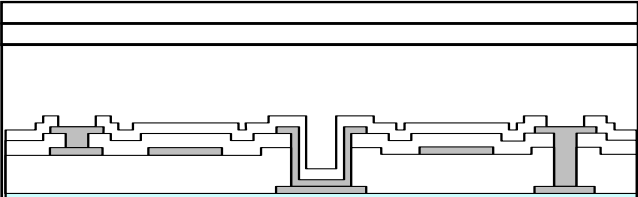
<p>9th Step Collecting-electrode Patterning</p>		<p>Wet-etching with Mask#4 See Fig.7d</p>
<p>10th Step Spin-coating Polyimide</p>		<p>Polyimide layer, 500-nm HD Microsystem PI-2610 HD Microsystem T9038 thinning solution</p>
<p>11th Step Pad and Well Opening (some detectors)</p>		<p>Dry-etching with Mask#5 See Fig.7e</p>
<p>12th Step A-Se deposition</p>		<p>Stabilized amorphous- selenium is thermally evaporated with a thickness of 50-um and 70-um</p>
<p>13th Step Hole-blocking Layer Deposition</p>		<p>Perylene and PT-CBI are thermally evaporated with a thickness of 500-nm and 50-nm, respectively</p>
<p>14th Step Top-metal Deposition</p>		<p>Gold semi-transparent gold layer is thermally evaporated (50-nm)</p>

Figure 5.4: Explanation of fabrication process steps.

avoid electrical breakdown. We should mention that the SiN_x film quality is degraded as the evaporation time and film thickness increase due to the formation of a porous structure in the film. The SiN_x film is fabricated with several evaporations, each of which deposits up to a 150-200 nm thick film to achieve the highest possible film quality.

5.3 Pulse height spectroscopy setup

The components of the PHS system (e.g., shaper and MCA) used in this study are the same as those used for the investigation of the hole conduction mechanism in PI (Chapter 3), except the preamplifier. Critical to reveal inherent properties of a-Se, the Amptek Coolfet preamplifier is replaced with the CUBE preamplifier, which is a very low noise monolithic CMOS preamplifier [173, 174]. Higher electronic noise causes broadening in the main spectral width and prevents resolving the lower end of the spectrum. These effects are also observed in a-Se due to incomplete charge collection. Therefore, it becomes a challenging task to identify the dominant mechanism responsible for degraded energy resolution. Previous studies demonstrated that the energy resolution of germanium and silicon drift detectors (SDD) could be improved substantially by using the CUBE preamplifier in place of the standard preamplifier (Camberra CI2002) under the same measurement conditions such as detector temperature, shaping time and bias voltage [175]. The Dante digital pulse processor (DPP) is also connected to the output of the CUBE preamplifier to measure signal rise-time of the detectors for single photon excitation with high temporal precision. The Dante DPP is equipped with a high-performance 16-bit analog-to-digital converter (ADC) which runs at 125 MSPS. XG-Lab designs both the CUBE preamplifier and the Dante DPP for achieving very high energy resolution with silicon drift detectors thanks to its state-of-the-art noise performance ($5.3 e^-$ of ENC with SDD) [176].

The PHS experimental setup and its circuit diagram are shown in Fig. 5.5 and Fig. 5.6, respectively. The CUBE preamplifier is wire-bonded to the printed-circuit-board (PCB), which is designed to achieve best noise performance. The PCB is connected to the bias

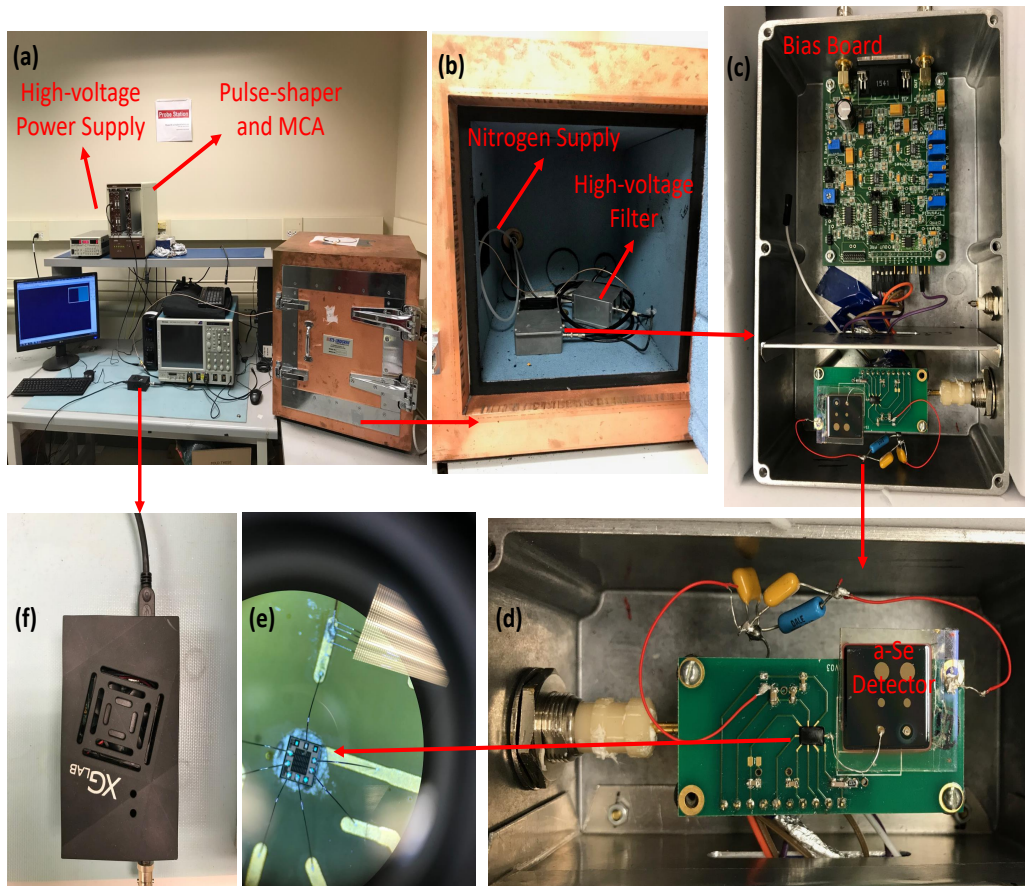


Figure 5.5: a) Pulse-height spectroscopy experimental setup for energy and time resolution measurement, b) copper housing with a vibration isolation foam, c) aluminium housing for the front-end electronic and the detector, d) a-Se detector on the low-noise custom-designed PCB, e) the CUBE preamplifier attached to the PCB, and f) the Dante ADC.

board that generates and filters the CUBE supply voltages, provides a reset signal to reset the preamplifier feedback capacitance, and buffers and amplifies the CUBE output signal. The CUBE preamplifier (Pre-038) has a feedback capacitance of 50 fF and is operated with a pulsed-reset mode with a MOS transistor periodically resetting the charge accumulated on the feedback capacitance due to dark current. A gain of 2 follows the

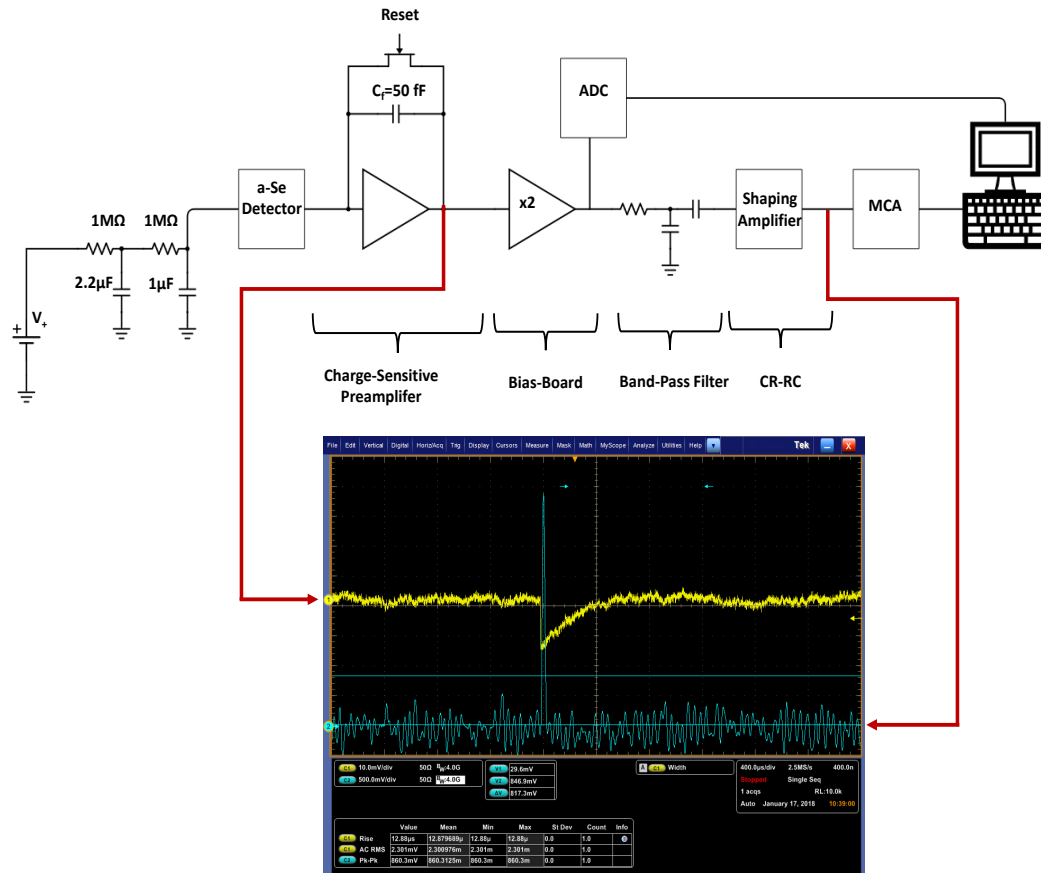


Figure 5.6: Circuit diagram of the PHS system and a typical output pulses of the preamplifier (yellow trace) and the shaper (green trace).

charge integration stage. The typical waveform of the preamplifier output signal is shown in Fig. 5.6. The dark current defines the reset period while the characteristic peaking time can be adjusted with the trimmer on the bias board. One important feature of having such a waveform is that it allows the measurement of the dark current concurrently during PHS measurements without introducing any other connection to detectors, which adds extra noise to the system. The following equation can calculate the dark current of the detectors:

$$I_{dark} = \frac{\Delta V \cdot C_f}{A \cdot \Delta t}, \quad (5.1)$$

where ΔV is the voltage, Δt is the time period that the preamplifier resets, C_f is feedback capacitance, and A is the amplification factor. We reduced the dark current related noise by employing a PI hole blocking layer with its optimized thickness of 1.5 μm . The dark currents were measured as only 10 fA/mm² at 8 V/ μm and 65 fA/mm² at 20 V/ μm , respectively. Therefore, the effect of noise due to dark current on the measured spectrum is insignificant. The reason for such as a low dark current is the extended time of the measurement duration. Due to the low activity of the gamma-ray sources used (e.g., 1 μCi), and the poor quantum detection efficiency of a-Se at this energy range with a 70- μm thickness, the measurements were carried out for 5-6 days, especially when the ⁵⁷Co gamma-ray source is incident on a-Se detectors. Therefore, as observed in the previous dark current analysis in Chapter-3, the dark current continued decaying by time and converged to its minimum several hours after the application of high voltage.

The size of the CUBE preamplifier is quite small (0.75 x 0.75 x 0.25 mm). Therefore, a-Se detectors are mounted very close to the preamplifier, and the stray capacitance is minimized due to a direct connection from the detector to the preamplifier input with a short bare wire. From signal-to-noise consideration, it is essential to maintain the lowest possible capacitive loading on the preamplifier input. We placed the detector, preamplifier, and the bias board into the same light-tight box. a-Se is very sensitive to optical photons, and any optical photon absorption may ruin the measurement since the signal of interest being measured is very low (only a few thousand electrons are generated per gamma-ray photon). We also placed this box into a copper box, which provides extra shielding for other noise sources (e.g., electromagnetic interference or vibration). The low-impedance output of the CUBE preamplifier is capable of driving its output signal into standard NIM modules (e.g., pulse shaper, ADC) through a long connection cable that creates large capacitance. The output pulses of the preamplifier are shaped and digitized with the same pulse-shaper and MCA used for the measurements in Chapter 3. The shaping time of the shaper is

adjusted accordingly, and the possible ballistic deficit effect (i.e., reduction in measured pulse amplitude) minimized to accommodate the extended transit time of photogenerated electrons. The longest transit time of the electron is calculated based on our time-of-flight measurements (see section 6.2) for the given applied field and a-Se thickness. For $E=8$ V/ μm and $d_{a-Se} = 70\mu\text{m}$, the transit time for electron and hole are calculated as $22 \mu\text{s}$ and $0.6 \mu\text{s}$, respectively. Here we used a shaping time, τ , of $12 \mu\text{s}$, which gives a peaking time of $12 \times 2.2 = 26.4 \mu\text{s}$. This shaping time barely satisfies the transit time of electrons. For the higher electric fields, the shaping time is adjusted accordingly to maintain the lowest possible noise. Note that a shaping time of shaping amplifier was not chosen arbitrarily large to achieve the best signal-to-noise performance. Due to the low count rate operation, the most emphasis is placed on the noise filtration and the minimization of the ballistic deficit.

5.3.1 Noise analysis and linearity measurements

In general, the total noise contributing to the each collected signal due to the single photon absorption is given as:

$$\sigma_{total} = \sqrt{\sigma_{stat} + \sigma_{photon} + \sigma_{dark} + \sigma_{elect}}, \quad (5.2)$$

where σ_{stat} is the statistical noise that originates from the intrinsic properties of the detector, and defines the lowest noise achievable with the detector, σ_{photon} is the shot noise associated with the total number of charge generated and is equal to \sqrt{ehp} , σ_{dark} is the noise due to the dark current of the detector configuration, and σ_{elect} is the noise associate with the electronic noise of the read-out electronics that complete the signal processing. The electronic noise is mainly dominated by the preamplifier noise in most of the PHS system. The measured dark current in our detector is insignificant, so does the dark current noise. The dark current shot noise is given as:

$$i_{shot} = \sqrt{2ei_{dark}\Delta f}, \quad (5.3)$$

where e is the elementary charge and Δf is the bandwidth. Given that the dark current is 50 fA and the shaping time is adjusted as 12 μ s, the dark current shot noise calculation using equation 5.3 yields to only 3.5 e_{rms} .

The electronic noise generation is a random process in nature, and it appears as a fluctuation in voltage or current. Because the noise signal bounces randomly back and forth around a zero value when averaged through the time-span of measurement, the root-mean-square (RMS) value is used for characterizing noise signals. Fig. 5.8(a) shows the output signal of the Dante ADC when the a-Se detector is connected to the preamplifier input and biased to 500 V. We measured the RMS electronic noise of the preamplifier in this configuration so that the added input capacitance effect due to the detector and connection can be considered. The common practice is to express the noise in terms of equivalent noise charge (ENC). This is defined as the amount of the charge that, if applied to the input terminal of the preamplifier, would give rise to the output voltage equal to the RMS value of the preamplifier due only to noise. Based on the $V_{out,rms}$ value of 200 μ V at the preamplifier output and the preamplifier feedback capacitance of 50 fF , we estimated the input-referred noise as 62 e^- (ENC), which is within the noise rating reported by the manufacturer of the preamplifier. Also, this measured electronic noise associated with CUBE preamplifier is almost an order of magnitude lower than the electronic noise measured in the PHS system used in Chapter-3 when we employ Amptek Coofet preamplifier.

The linearity and the calibration of the PHS system (e.g., pole-zero correction) are also tested before the detector is connected by using a low noise pulse generator (shown in Fig. 5.7). The test pulses have a fast-rising edge and relatively long tail. That simulates the induced current due to the single photon absorption in a-Se detector. This measurement also enabled us to identify the noise contribution of the other system components (shaper and MCA), and to confirm the measured preamplifier noise in FWHM (2.355σ) when we connect the detector to the preamplifier input node. The outputs of test pulses with positive polarity (holes) are shown in Fig. 5.8(b). We observed that the PHS system has an excellent linearity over whole test input range (10 mV-500 mV), and the noise added

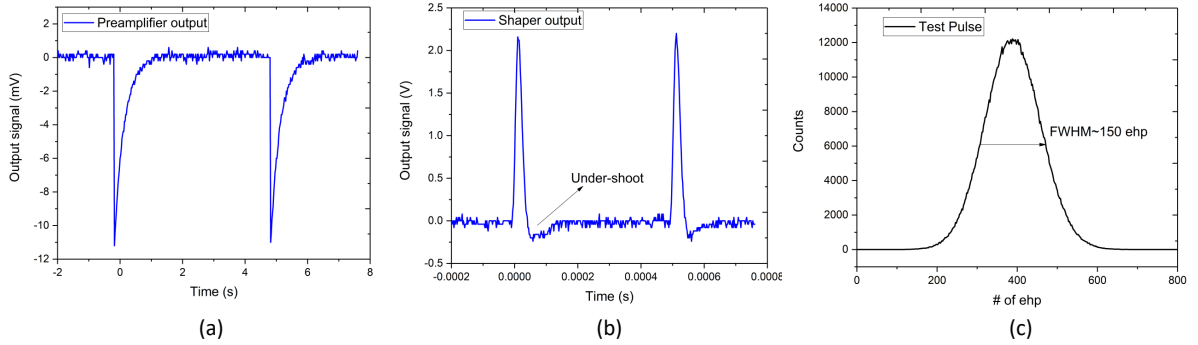


Figure 5.7: a) Output of the CUBE preamplifier, b) output of the shaper, c) output of the MCA for the input test pulses.

by other stages (shaper and MCA) were found significantly low.

5.4 Experimental results

5.4.1 Spectral performance of conventional detectors

Fig. 5.9 shows the measured energy spectra obtained with the conventional a-Se detector as a function of the applied electric field. The spectrum consists of a single-peak located above the low-amplitude background noise and long-tail related to the incomplete charge collection. The detector has a surface area (defined by the top electrode) of 1 mm^2 and a capacitance of 0.8 pF approximately. One of the most challenging parts of realizing small detector capacitance is to establish a simple and robust connection on such a small device area without using wire-bonding technology. High pressure and applied heat required for wire-bonding would lead to crystallization on a-Se, thus, we could not utilize wire-bonding for the connection on the top contact of the device. Instead, we made the connection manually under a microscope using a small chunk of conductive silver paste. Radioisotope sources ^{241}Am and ^{57}Co were used to provide monoenergetic gamma-ray photons with $\epsilon = 59.5 \text{ keV}$ and $\epsilon = 122 \text{ keV}$. The detector is exposed to gamma-ray photons from topside, and

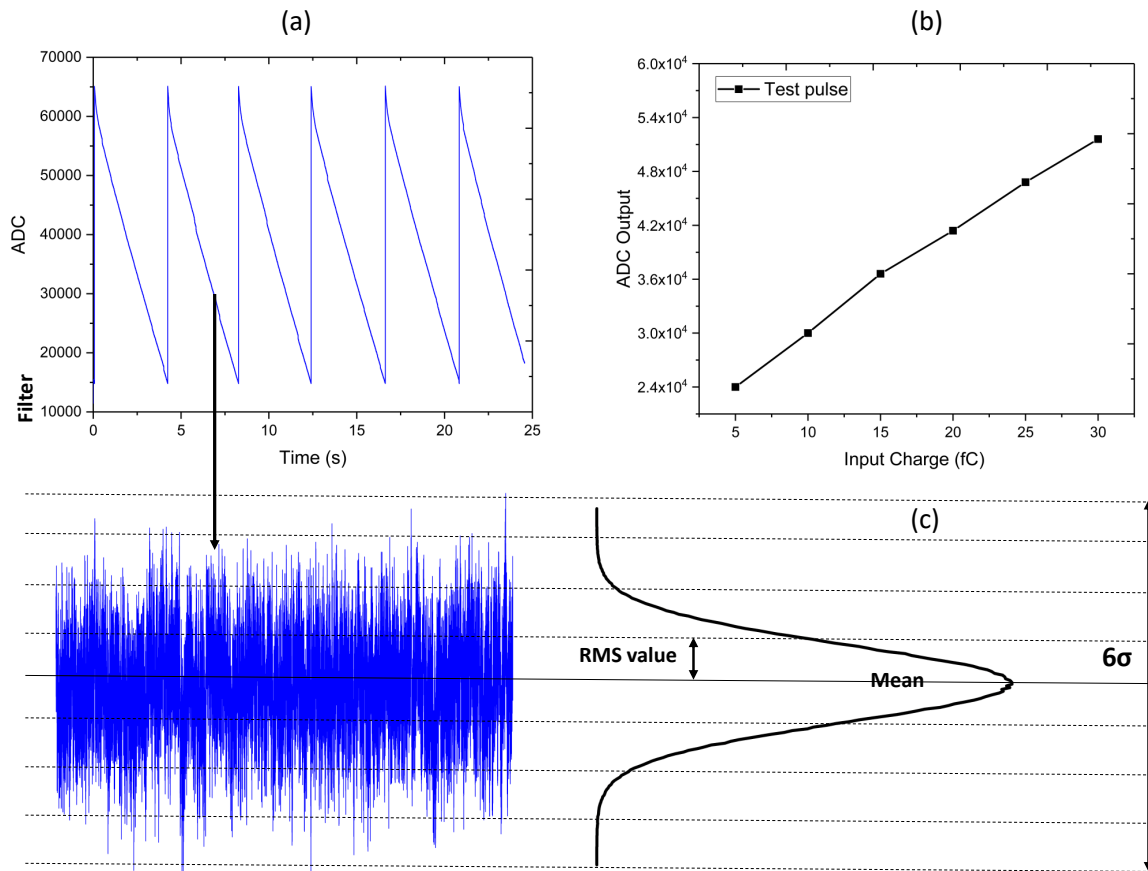


Figure 5.8: a) Output signal of the Dante ADC, b) linearity test results of the PHS system, c) Illustration of Gaussian noise parameters.

the detector-to-source distance is approximately 5 cm. The applied voltage on the detector is varied to provide an electric field in the range of 8-20 V/ μm (the spectrum at 8 V/ μm is shown in Fig. 5.20). No protection circuit is connected into the preamplifier input to achieve the best noise performance. However, the risk of damage on the preamplifier input stage (on the input FET) is much higher in this configuration. Therefore, we determined the upper limit of the electric field as 20 V/ μm to ensure that the input stage of the preamplifier is not damaged. The x-axis is calibrated in terms of electron-hole pairs, which

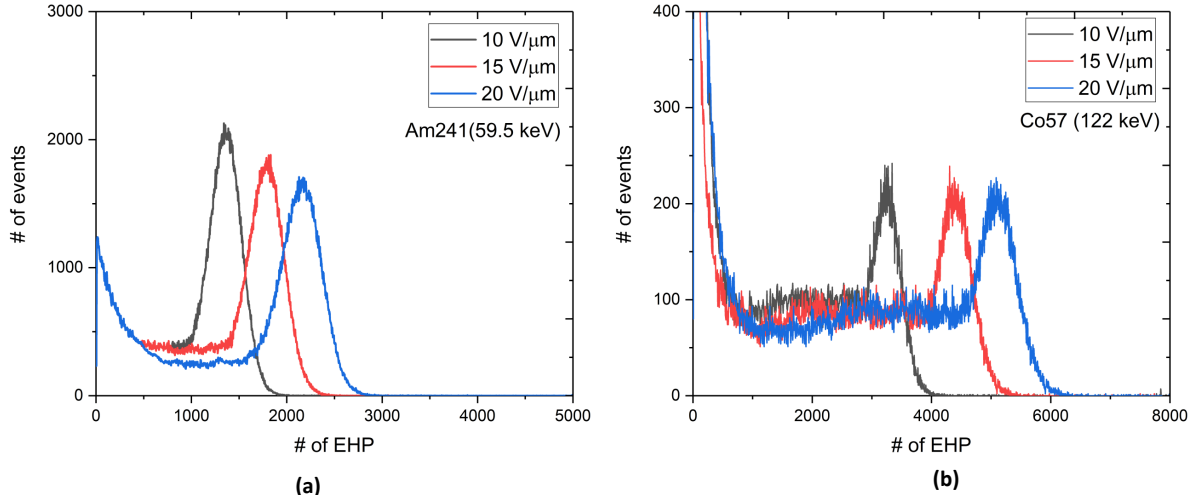


Figure 5.9: Measured energy spectrum by the a-Se conventional detector with a) ^{241}Am and b) ^{57}Co gamma-ray sources as a function of applied electric field.

is referred to as a total photogenerated charge in the preamplifier input. Mean and standard deviation values associated with each spectrum are estimated based on the Gaussian fitted curves.

Fig. 5.12(a) plots the ionization energy W_{\pm} against the electric field (E) for both photon energies. As seen in the figure, total EHP is proportional to the applied electric field and the incident photon energy, agreeing well with the simulation results obtained in the previous chapter. The results indicate inverse field dependence of the conversion gain, $W_{\pm} \propto E^{-2/3}$, and consequently sublinear field dependence of the mean photogenerated EHP, $\sim E^{2/3}$, as seen in the previous investigations. It can be seen from the results that W_{\pm} can be reduced by almost a factor of two by increasing E from 10 V/ μm to 20 V/ μm . These results demonstrate the significance of the hole blocking layer, as the high field operation of a-Se is required to achieve a higher charge gain while maintaining a lower dark current. In Fig. 5.12(b), our experimental results for the ^{241}Am source are re-plotted together with the simulation results and the measured results adapted from Blevis et al.(Fig. 5.10) to compare different experimental conditions and device properties.

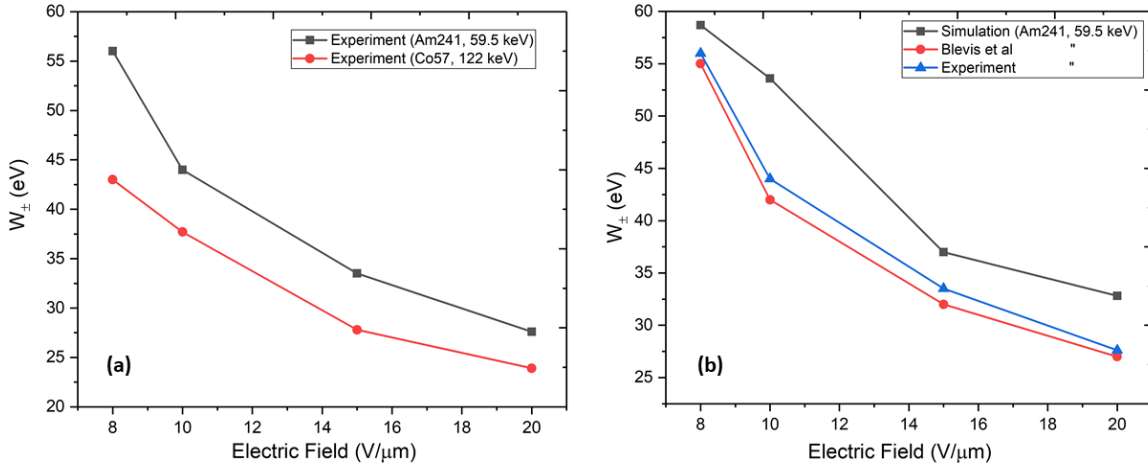


Figure 5.10: a) Measured ionization energy vs. applied electric field, b) adapted from Blevis et al [13], and simulated ionization energy vs. electric field.

The theoretical results obtained by the Monte-Carlo simulation are seen to lie almost 20% higher than the results obtained by both experiments, but the agreement between our experimental results and the results measured by Blevis et al. are very good, indicating the quality of the a-Se devices used by both studies are comparable. It was previously reported that E dependence of W_{\pm} can be explained by the recombination of a large amount of charge initially generated by the incident photon. A charge cloud is created after photon absorption with a different cloud diameter depending on the photon energy (e.g., the charge cloud diameter is around 8-10 μm for mammography energy range, (\sim 25-30 keV)). The recombination rate of such charges in different cloud sizes and charge density would be different, so does W_{\pm} . The simulation model takes these effects into account to some extent; however, it is limited by the lack of detailed theory of recombination in terms of charge distribution scale parameters. Therefore, one reason for higher W_{\pm} values in the simulation study compared to the empirical results might be that the simulation model overestimates the geminate recombination distance (recombination of photogenerated charge right after dissociation), \sim 1 nm for example, and does not include a physical model explaining the

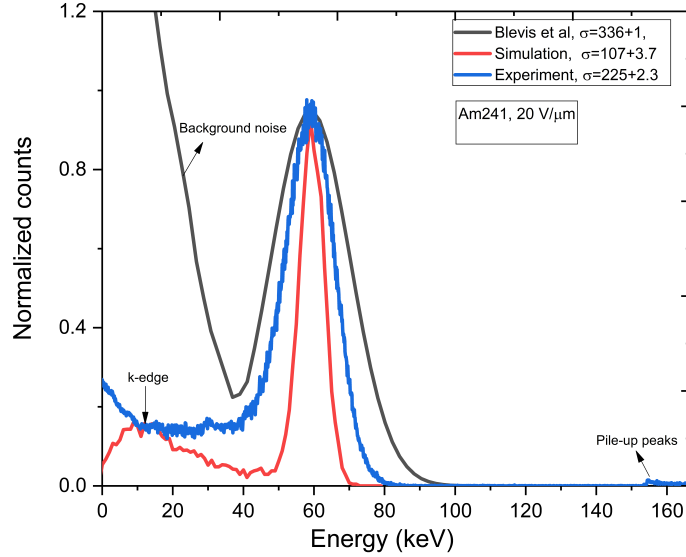


Figure 5.11: ^{241}Am spectra obtained by our conventional a-Se detector, Blevis et. al [13] and Monte-Carlo simulation.

W_{\pm} dependence on the charge cloud size and density with a high precision. Therefore, an excessive amount of the photogenerated charges are already considered to be lost before drifting to the collecting electrode. Another reason might be that the simulation study does not ignore the other peaks at lower energies in the spectrum when calculating W_{\pm} , thus provides poor estimation with respect to experimental results.

Standard deviation, σ , of the Gaussian-fitted curves based on the highest peak in each distribution were measured. Then, the FWHM energy resolutions were calculated, which is simply 2.335σ . The fitting does not consider the lower energy peaks such as K-fluorescence, Compton continuum, and background noise. The raw spectral width, represented in FWHM, at each applied field and photon energy were corrected for the measured electronic noise and the uncertainty associated with the signal shot noise. Fig. 5.12(a) shows the measured standard deviation in the spectral widths for both gamma-ray sources as a function of the applied electric field. The results indicate that as the ap-

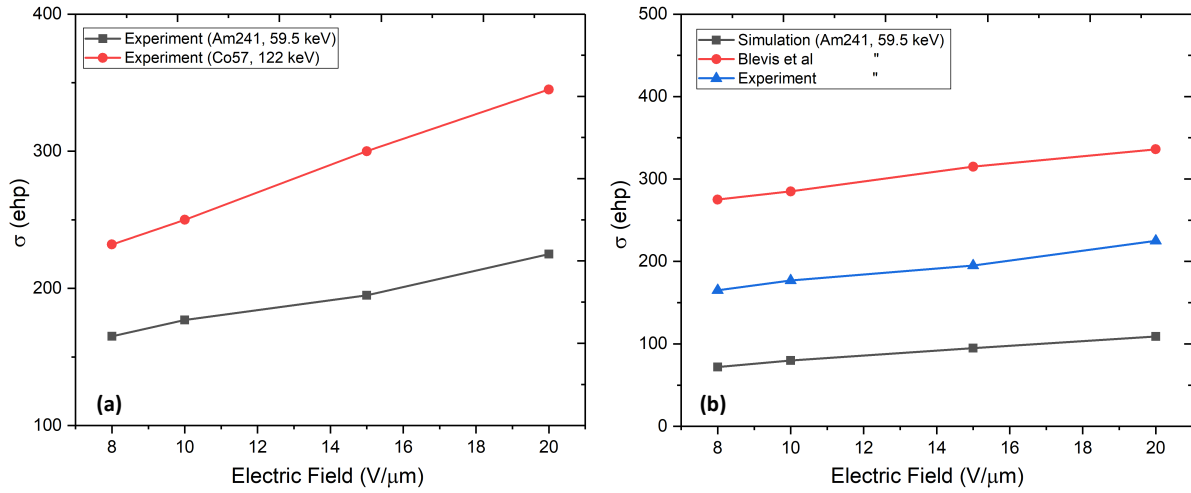


Figure 5.12: a) Measured σ vs. E , b) adapted from Blevis et al. [13] and simulated σ vs. E .

plied field and the incident photon energy increase, the standard deviation of the collected charges increases. These results are consistent with the results reported by Rowlands et al. This is clearly illustrated in Fig. 5.12(b), which compares standard deviations reported by another experimental study (Blevis et al.) with our measured results for the ^{241}Am gamma-ray source. The simulation results are also included in Fig. 5.12(b), which are obtained for the same conditions. A similar trend in standard deviation is also observed with the simulation results.

However, another noticeable result is that both experimental data show higher standard deviation compared to that of simulation data, although our measured standard deviation is much lower than that of the standard deviation measured in the other experimental study. This could be due to two main reasons. First, the gamma-ray source used in the simulation is a perfect monoenergetic source with the multiple filter combination. However, gamma-ray sources used in the experiments are not a perfect monoenergetic source. Second and most importantly, considerable noise is added to the experimental spectrum due to electronic noise and dark current. These noise sources are not considered in the simulation

study. Comparison of the measured noise (or standard deviation of the spectral width) by both experimental studies also confirm the second argument. Blevis et al. reported the measured electronic noise and the dark current as $500 e^-$ (ENC) and 1 pA, respectively. On the other hand, our electronic noise is only $62 e^-$ (ENC), and the dark current is almost two orders of magnitudes lower (~ 10 fA) compared to that of the dark current reported by Blevis et al. Therefore, the results show that the minimization of system and detector noises are of particular importance for the investigation of intrinsic properties of a-Se detectors.

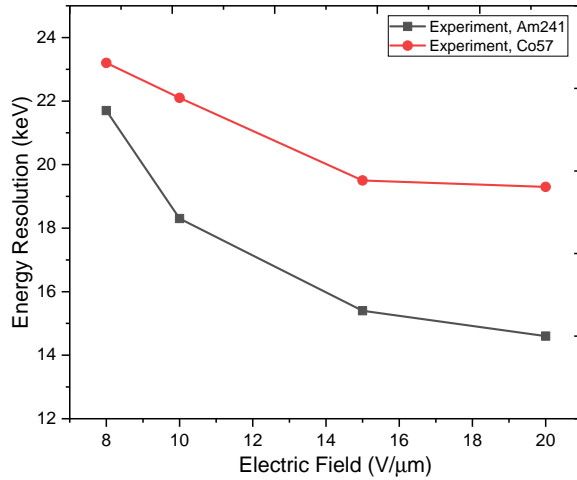


Figure 5.13: Measured energy resolution of the conventional a-Se detector for the incident gamma-ray sources of ^{241}Am and ^{57}Co

A significant improvement in energy resolution, ~ 18 keV at 59.5 keV, is achieved with our a-Se detector and pulse-height spectroscopy configuration compared to energy resolution reported in the literature, ~ 33 keV at 59.5 keV [13]. A vast improvement in energy resolution obtained indicates that conventional a-Se devices employing a lower dark current with an optimized thickness of PI, even at higher applied voltage, results in a considerable reduction of noise, leading to better energy resolution. This improvement could also be attributed to reduced electronic noise thanks to the state-of-the-art front-end electronics. Fig. 5.13 shows the estimated energy resolution at both gamma-ray energy as a function

of the applied electric field. For the higher applied field and incident photon energy, the FWHM of each spectrum is seen to be increasing. However, since the mean number of photogenerated charges increases faster, a spectrum with better energy resolution was obtained at higher fields and photon energies. FWHM energy resolution in the range of 15-24 keV was obtained over the parameter space. It should be noted that although the energy resolution of the a-Se detector is enhanced with better noise suppression, it is still an order of magnitude worse than the theoretical resolution based on charge statistic consideration explained in the previous chapter. There might be many reasons that contribute to the broadening of the spectrum; however, electron trapping is still one of the dominant factors. Further experimentations are needed to identify these resolution-limiting factors.

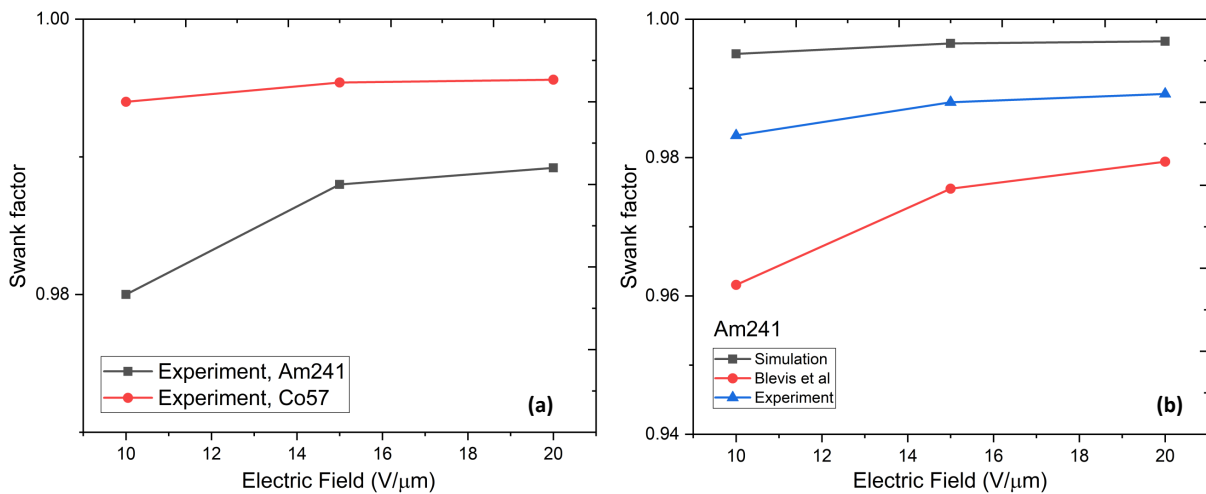


Figure 5.14: a) Measured Swank vs. E, b) adapted from Blevis et al. [14] and simulated Swank vs. E.

Fig. 5.14(a) shows Swank factors calculated from the experimental results for both gamma-ray energies as a function of the applied electric field. The results indicate that the Swank factor increases with the increasing electric field and incident photon energy and varies within the very narrow range of 0.981-0.996. Similar trends are observed with the calculated Swank factors based on the simulation results, which are given in Table

4.2. Fig. 5.14(b) shows our experimental and simulation results, as well as the calculated Swank factors adapted from Blevis et al. [14]. In all cases, due to lower variance of the spectrums, the simulated Swank factors are higher than the Swank factors calculated based on the experimental results. For the same reasons, our calculated Swanks factors are also higher than that of Swank factors reported by Blevis et al [12].

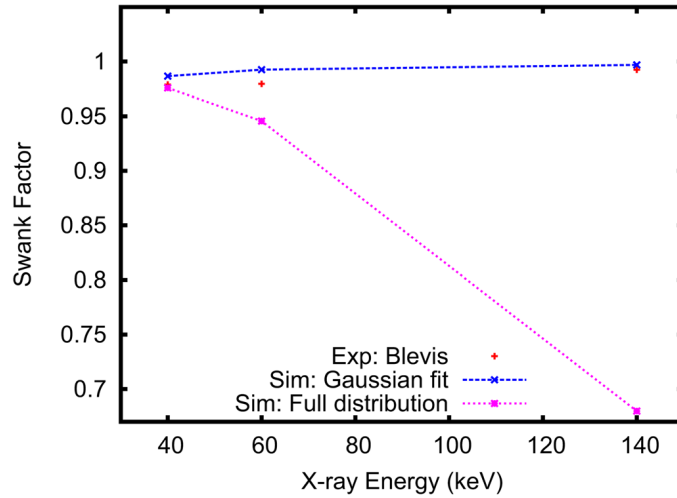


Figure 5.15: Calculated Swank noise based on Gaussian fitting and full spectrum. Reprinted from [12] with permission granted.

We need to point out that these results are valid only if charge trapping can be ruled out and the Gaussian fitting of the single photopeak is acceptable. However, significant degradation in the Swank factor is observed when the full distribution of pulse-height spectra is considered. The calculation of full distribution contains the effect of charge transport, not only the charge generation stage; hence, the thickness of a-Se and the electric field becomes important. Fig. 5.15 shows the significant difference between the Swank factor calculated based on Gaussian fitting and full spectrum distribution, where the Swank factor is found very close to unity using Gaussian fitting, indicating the statistical variation in the charge formation stage is close to unity. However, we already confirmed that the energy resolution is limited due to some factors, and we expect that the calculated

Swanks factor should be a true reflection of these factors. Therefore, we believe that Swank factor estimation with a full energy distribution is particularly important to justify the charge trapping effect on the statistical variation of the charge collection in a-Se.

5.4.2 Device operation and charge transfer measurements of unipolar charge sensing detectors

Before the signal rise-time and PHS measurements are carried out with the fabricated unipolar charge sensing detectors, a proper biasing configuration of the grid and top electrodes should be investigated to operate the device with an efficient single polarity charge sensing regime for a given device configuration (e.g., pixel pitch and photoconductor thickness). This ensures that no significant charge accumulation occurs on the dielectric layer and high radiation sensitivity is achieved through a high charge collection efficiency, which is only possible by collecting the charge carriers with higher mobility and lifetime product. Since the transport properties of holes are much better than that of electrons in a-Se devices, the top electrode and grid layers are positively biased such that all photogenerated holes are directed towards collecting electrodes. With this read-out scheme, a virtually full amplitude of the output signal is formed after holes pass through grid layer, as long as the collecting electrode collects all holes, even if electrons are not collected due to trapping at the region between the top electrode and grid. Also, the amplitude of the output signal will be reduced if these photogenerated holes are shared between grid and collecting electrodes.

Before performing experimental studies, simulation results were obtained to gain an initial insight so that possible breakdown with the dielectric layer on the grid layer can be avoided by operating the devices with a reasonable grid voltage. From the formation of electric field streamlines as shown in Fig. 5.16, the path of the carriers is determined, assuming that the internal electric field is uniform and not deteriorated due to the space-charge effect during the operation of the device. In order to maintain the same internal electric field strength for all device configurations with different pixel pitch, possible top

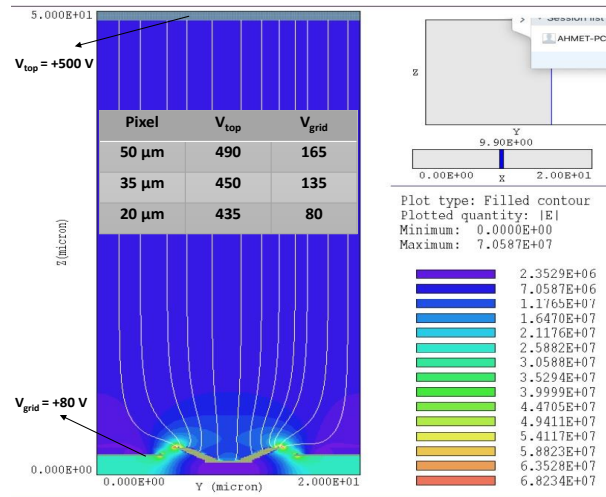


Figure 5.16: Simulated electric field stream lines for the device having a 20- μm pixel pitch. Inset shows the required grid voltage for the same device configuration for various pixel pitch, 20, 35 and 50 μm .

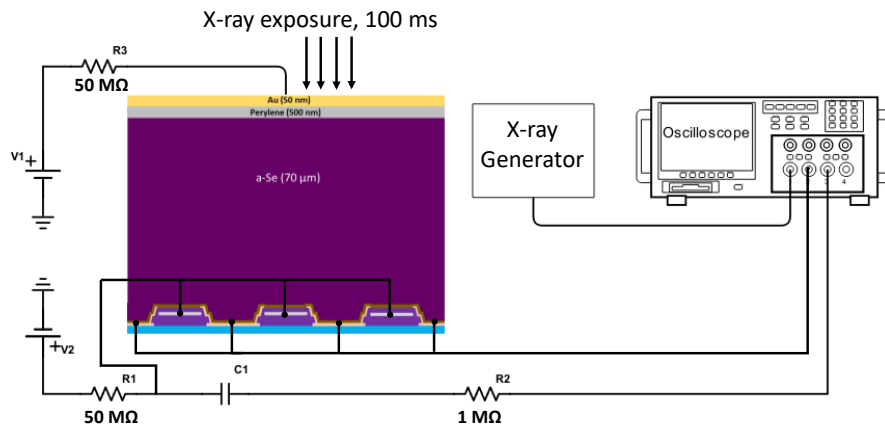


Figure 5.17: Experimental Setup used for charge transfer measurements.

electrode and grid voltage configurations were investigated. Our empirical results suggest that increasing voltage beyond 500 V on the top electrode for a device having 50- μm thick

a-Se is not practical to maintain small signal operation due to the increased dark current level. Furthermore, higher top electrode voltage leads to the higher possibility of dielectric layer breakdown on the grid metals because the grid voltage needs to be increased for a higher top electrode voltage to bend the electric field lines efficiently. For the devices containing PTCBI ($\sim 50\text{nm}$) and Polyimide ($\sim 800\text{nm}$) hole blocking layers, we measured the dark current densities at 500 V and found around 0.5 pA/mm^2 and 0.1 pA/mm^2 600 seconds after the application of high voltage, respectively. The measured dark current of the device with a perylene blocking layer is insignificantly low. Fig. 5.16 shows the electric field streamlines for one of the fabricated MPPC devices with $20\text{-}\mu\text{m}$ pixel pitch, where the top electrode and grid layer is biased to $+435\text{ V}$ and $+80\text{ V}$, respectively. Almost all the electric field lines end up on the collecting electrode, indicating that charge carriers are collected by only collecting electrode, and the charge transfer efficiency close to unity is achieved. Simulated grid voltage versus pixel pitch for achieving full charge transfer efficiency for the different grid pitch ($20, 35, \text{ and } 50\ \mu\text{m}$) are shown in inset of Fig. 5.16. The magnitude of the voltage required on the grid layer depends primarily on the voltage of the top electrode and photoconductor thickness, and it is reduced with a smaller pixel pitch. The average internal electric field is calculated around $8\text{V}/\mu\text{m}$ for all the devices, and it would remain substantially uniform because the required grid voltage is smaller compared to the voltage on the top electrode. It is also noticeable that the possibility of local hot-spot formation, and thus electrical breakdown, is lower with a smaller pixel pitch due to lower grid voltage required, as long as such a device is fabricated with uniform SiN_x and PI layers without any defects.

The experimental setup used for charge transfer measurements is shown in Fig. 5.17. The grid layer is capacitively coupled to oscilloscope input so that the amount of charge induced on the grid layer can be read-out simultaneously while it is biased to the required voltage. The detectors absorbed generated X-ray pulses, and induced photocurrents on the collecting electrode and the grid layer, if any, were measured concurrently by a digital oscilloscope. The number of pixels for each detector were binned to form a single pixel having the same active area, and measurements were carried out under identical internal

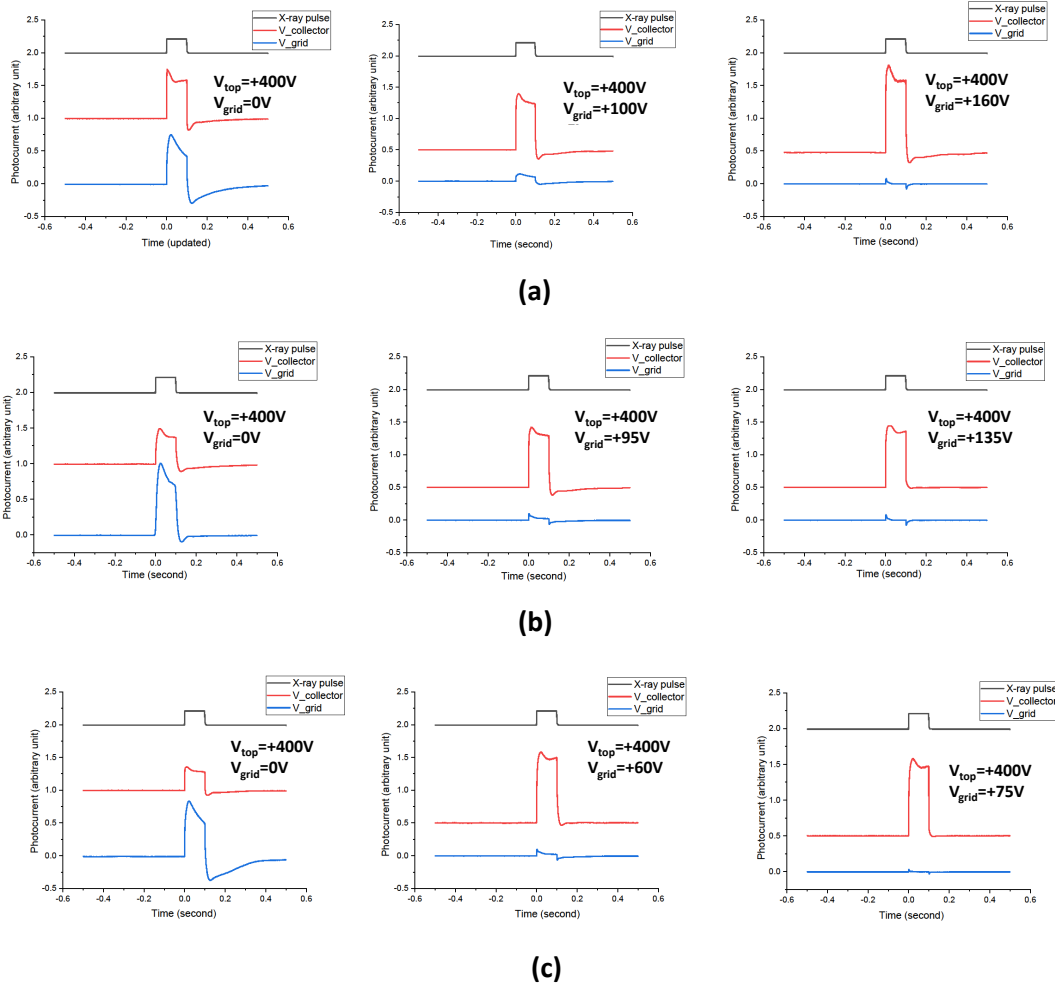


Figure 5.18: Charge transfer measurement for (a) $50 \mu\text{m}$ pixel, (b) $35 \mu\text{m}$ pixel, (c) $20 \mu\text{m}$ pixel at approximately $8 \text{ V}/\mu\text{m}$.

electric field strength ($8 \text{ V}/\mu\text{m}$) and X-ray dose (i.e., 1 mR). SRS series high voltage power supplies provided the bias for the top electrode and the grid layer. First, the voltage on the top electrode was gradually increased to the final value and waited until the dark current decayed to the saturation point. Then, the voltage on the grid layer was increased in a

few steps, and the transient of remnant charge was measured until no charge was left on the grid layer. Fig. 5.18 shows the charge transfer characteristics of the devices with a different pixel pitch. As expected, the total photo-induced charge is shared between the grid layer and collector when they are both grounded. However, the amount of the charge is proportional to the area covered by the collector; a lower amount of charge is induced for the device with a smaller pixel pitch. As the grid voltage is increased, we observe that more charge is terminated on the collector and the amplitude of the output signal reaches to its maximum when no charge is left on the grid, indicating full charge collection efficiency is achieved. There is a significant difference between the required grid voltages for different pixel pitch, agreeing well with the simulation results. What we observe is that the empirically investigated voltage values for the grids for full charge transfer efficiency are slightly higher than the values estimated with simulation studies. The reason might be the imperfection with the fabrication of the detectors. Moreover, we did not include the PI layer for the simulation studies because the surface coverage properties of the PI layer (i.e., its real thickness on SiN_x) cannot be predicted. Nevertheless, the measured voltage values are still within the expected range; only 15-20% discrepancy is observed.

5.4.3 Transient signal measurements

Depending on the simulation results and the charge transfer measurements, we found the unipolar charge sensing detector with a 20- μm grid pitch optimum for achieving the best temporal resolution. Smaller grid pitch requires lower grid voltage while maintaining a more effective near-field effect for more efficient single polarity charge sensing. Lower grid voltage reduces the risk of dielectric breakdown for the detectors operated at a higher electric field. The unipolar charge sensing detector used for this measurement has a 70- μm thick a-Se layer and PTCBI hole blocking layer for the application of high voltage. We used the ^{241}Am gamma-ray source with the activity of 10 μCi .

Through our test measurements, we investigated that the application of the high voltage on the grid layer causes a large amplitude transient noise, although it was not the case

for the charge transfer measurements. The different noise performance between these two setups should originate from the signal amplitude that is being measured by each setup, and the sensitivity of the amplifiers. With the charge transfer measurements, we used 100 ms-long X-ray pulses with 1 mR radiation dose, thereby the signal-to-noise ratio (SNR) was higher. However, here, we need to measure only 1000-1500 EHPs, which puts an extreme limitation in terms of SNR. The transient noise distorts and interferes with the original signal and prevents us from identifying it. We could not suppress this transient noise without the input protection circuit. Furthermore, we realized that employing such a circuit leads to extra noise, which shadows the main signal. Therefore, the operation of the detectors at the higher applied electric field is compromised. We empirically discovered the limit of the grid voltage and found as 150 V for the detector with a 20- μm grid pitch. The respective top voltage with the detector (having a 70- μm a-Se and 150 V grid voltage) is measured through the charge transfer measurement setup, and 700 V found as an efficient bending of the electric field lines to the collecting electrode. The internal electric field of the detector is calculated as around 8 V/ μm with this grid and top electrode voltage configuration. A conventional detector with the same a-Se thickness and PI hole blocking layer is also fabricated for comparison purposes.

Rise-time of the detectors output signal with a single photon excitation is measured as a figure-of-merit for the temporal response characteristics. The Dante ADC captures photogenerated charge pulses from the preamplifier at the sampling interval of 8 ns. Because the purpose of this measurement is to measure the rise-time of the pulses rather than their absolute amplitude, the digitized waveforms were offset corrected and normalized to the unit pulse height. The variation in the measured pulse heights is further analyzed with the PHS measurements in the next subsection. A baseline and the saturation points of each pulse are identified based on the average expected pulse height and the RC time constant of the measurement circuit, which defines the decay time of the output signal. Finally, the normalized pulses are shifted in time scale axis so that their starting points are matched. Fig. 5.19 shows the single photon excitation responses for both conventional and unipolar charge sensing detectors. Traces shown for each detector are averages of three

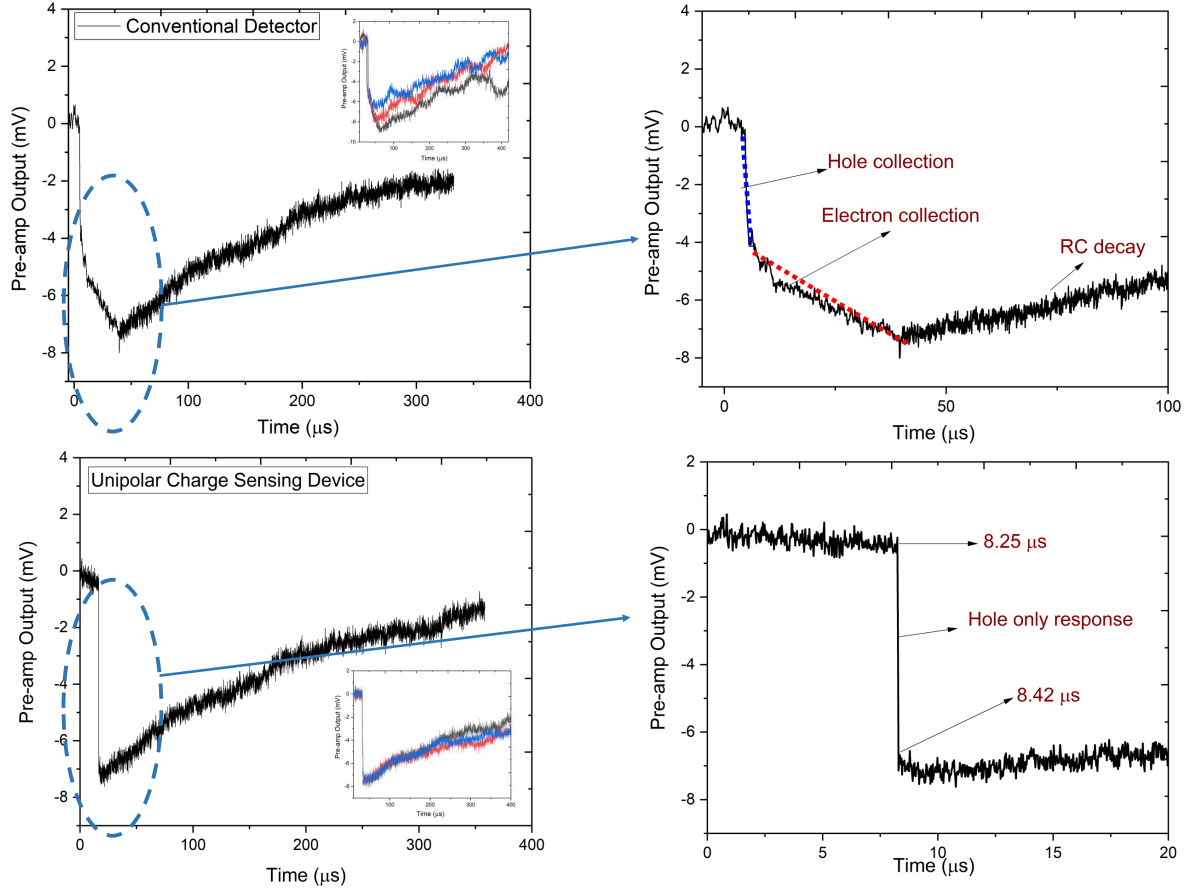


Figure 5.19: Collected charge as a function of time at $E = 8 \text{ V}/\mu\text{m}$ for a single gamma-ray photon interaction. For the conventional planar detector, signal rise-time is highly depth dependent and in the worst-case it is electron-transit-time-limited. However, for the unipolar charge sensing detector, signal risetime is substantially reduced due to near-field effect. Insets show the results for the multiple events.

successive signals, are illustrated in Fig. 5.19 (inset). After averaging, the waveforms are normalized again and compared to that of the theoretical results. We implemented the same corrections and normalization for more than 1000 pulses and found the deviation of the pulse heights only to be around 3-4%. The deviation is later calculated based on the

pulse-height spectroscopy results of both detectors. In Fig. 5.19(a), the measured signal with the conventional detector is shown. The signal follows the Hecht formula, where the signal rise-time has a faster component due to the drift of holes and a slower component due to the drift of electron, with the signal rise-time ranging from $0.6 \mu\text{s}$ (hole only) to $22.4 \mu\text{s}$ (electron only). Different pulse heights due to the different photon absorption depth are also evident. In the case of the unipolar charge sensing detector, however, the signal rise-time only consists of a faster component due to the hole-only collection, with the signal rise-time of only $150 \pm 11 \text{ ns}$. Furthermore, the variation in the pulse height of each detected signal is quite smaller. The photon count-rate calculation based on the assumptions in Chapter 6 yields more than two orders of magnitude improvement with the unipolar charge sensing detector compared to that of the conventional detector. We should state that theoretically predicted rise-time (hole dispersion limited) cannot be achieved due to some reasons. With the experimental results we obtained thus far, we do not have a satisfactory explanation, and further measurements are needed.

5.4.4 Spectral performance of unipolar charge sensing detectors

With the simple planar detector configuration, the poor electron collection characteristics of a-Se give rise to poor gamma-ray spectral response, particularly at the lower electric field operations. However, we have empirically shown that the signal rise-time and the variation of the pulse-height for single photon excitation can be reduced significantly with the unipolar charge sensing detector design. Here, we carried out further measurements with the PHS setup by replacing the conventional detector in the setup with the unipolar charge sensing detector used for signal rise-time measurements to identify the extent of the spectral improvement. During the operation, a bias voltage of 135 V and 680 V were applied to the grid and the top electrode, respectively. The average electric field across the detector was calculated around $8 \text{ V}/\mu\text{m}$ with this bias configuration. A total number of 30-by-30 pixels were binned to achieve a good compromise between a small capacitance for the lower noise and a detectable signal, which is limited due to lower activity of gamma-ray

source (^{241}Am , $10\ \mu\text{Ci}$) and lower quantum absorption efficiency of the detector for the a-Se layer thickness ($70\ \mu\text{m}$) employed. The spectra with the unipolar charge sensing detector were acquired with a shaping time of $2\ \mu\text{s}$, which is arranged depending on the hole transit time over the a-Se thickness. For comparison, we also measured the spectra with the conventional detector at the same applied field and with different shaping time (i.e., $12\ \mu\text{s}$) to accommodate electron drift time.

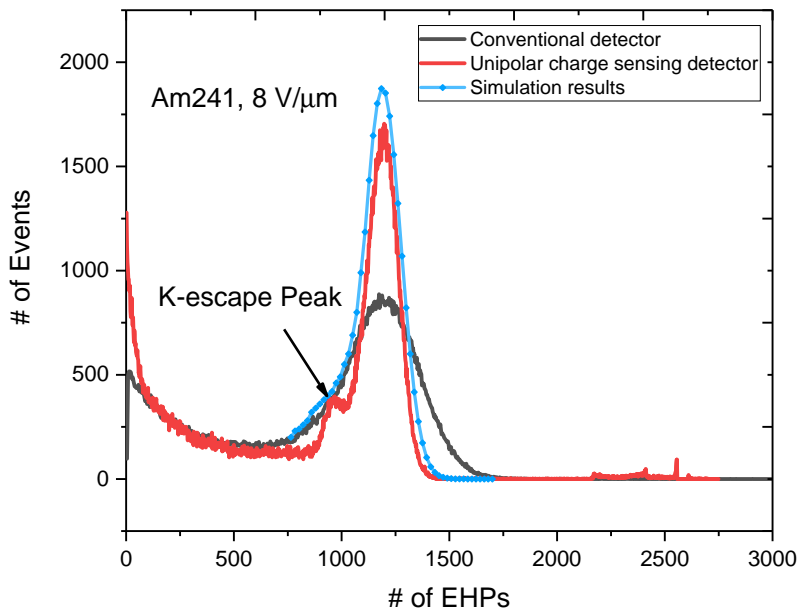


Figure 5.20: Spectrum of ^{241}Am obtained from the conventional and unipolar charge sensing a-Se detectors at $8\text{V}/\mu\text{m}$. Simulation result is also included (adapted from Stavro et al. [15]).

Fig. 5.20 shows the acquired spectrums for both detectors. Simulated spectra for the unipolar charge sensing detector (adapted from Stavro et al. [15]) is also included in the plot. In the spectrum obtained with the conventional detector, the photo-peak is broader, $24.2\ \text{keV}$ in FWHM, and most of the events responsible from the full energy absorptions are distributed to the broad continuum (i.e., tailing effect) due to the incomplete electron

collection. The K-fluorescence escape peak is not resolvable because the spectrum of the main photo-peak obscures its detection. On the other hand, a substantial enhancement in the spectral performance with the unipolar charge sensing is apparent, as indicated by the narrower photo-peak and the reduced tailing effect. The spectra closely resemble the simulated spectra except that the clear K-fluorescence escape peak shows up from the main photo-peak in the experimental spectra. This can be attributed to the lower electronic noise of the experimental system compared to that of the noise included in the simulation (e.g., $85 e^-$ (ENC)). The energy resolution obtained here, ~ 8.3 keV in FWHM, with the unipolar charge sensing detector is likely limited by the hole collection efficiency of a-Se, and the resolution can be further improved with a higher applied electric field if the lower noise can be achieved with the front-end electronics for the higher grid voltage.

5.5 Photocurrent lag and ghosting measurements

Temporal performance of the a-Se detectors in energy integration mode is characterized by mainly two figure-of-merits: photocurrent lag and ghosting. Lag is an increase in the photocurrent signal level after the X-ray exposure and, hence, it is measured after the X-ray exposure is terminated. Ghosting is defined as the change in X-ray sensitivity of the detector and, as opposed to lag, is measured during subsequent X-ray exposure. Previous studies reported that photocurrent lag in a-Se detectors is originated from two primary sources: the release of trapped electrons and increased charge injection from the metal contacts [97]. Two main technologies have been investigated by Anrad and Hologic companies for the commercial a-Se detectors to prevent charge injection. Anrad uses n-like and p-line blocking layers, which are doped a-Se layers [177]. The main problem with this technology is that the drifting of dopant ions under the applied field changes the properties of the intrinsic layer, thus causes long-term stability problem. Hologic utilizes a perylene insulation layer as a hole blocking layer. The presence of this layer causes a charge accumulation at the insulator/a-Se interface and prevents the use of the detector for

real-time imaging applications. The PI hole blocking layer, however, allows high frame rate imaging while effectively limiting the dark current, as investigated in Chapter 3. Once the lag originated from cumulative charge injection is eliminated by the PI hole blocking layer, the remaining lag is accounted for by the intrinsic properties of the a-Se photoconductor. In this section, we report the lag and ghosting measurement results of a conventional a-Se detector by limiting the increased dark current with the PI layer. We also report the lag results obtained by the unipolar charge sensing detector for the real-time X-ray imaging application such as fluoroscopy.

5.5.1 Measurement setup and method

We carried out photocurrent measurements to validate whether the fabricated unipolar charge sensing devices eliminate the photocurrent lag. First, both unipolar charge sensing and conventional devices are exposed to X-ray pulse. Then the photogenerated current is fed into a Keithley-427 current amplifier, and the output signal is measured with an oscilloscope. The top electrode and grid layers of the unipolar charge sensing detector are biased with the bias voltages, as investigated in the charge transfer measurements to operate the device with a full unipolar charge sensing regime. Recall from Figure xx that there is no considerable charge accumulation detected at the interface under the X-ray illumination for 1 second of exposure. However, here, we follow the fluoroscopic imaging procedure in terms of exposure time and the total radiation dose (e.g., 10 minutes continuous exposure). Therefore, any insignificant accumulation during short exposure would accumulate over time and degrades the internal electric field during this long measurement. To rule out this possibility, the PI layer on the collecting electrode of the unipolar charge sensing detector is etched.

Fig. 5.21 illustrates a typical X-ray response of the a-Se detector under the illumination of the pulsed X-ray source [16]. As evident from the response, the dark current increases during the exposure. Therefore, an average signal amplitude should be defined to determine the sensitivity of the detector. Then, the lag and the ghosting can be quantified. The

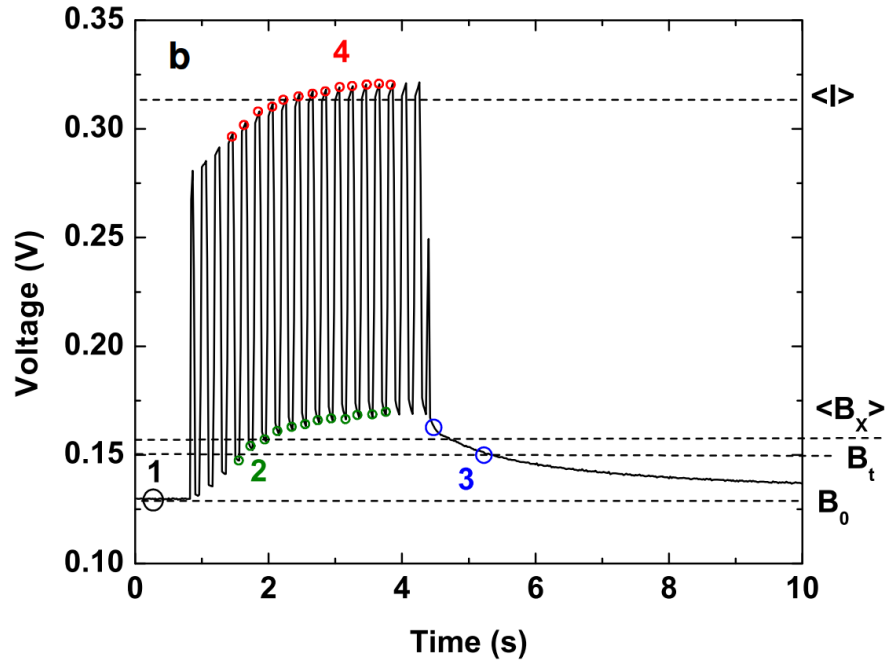


Figure 5.21: Typical output signal of a-Se detector under continuous X-ray pulse illumination [16].

residual dark current is measured before and after the exposure. The sensitivity, S , is defined as the difference between the average photocurrent, $\langle I \rangle$, and the average dark current, $\langle B_x \rangle$. The data points used for the calculation of $\langle I \rangle$ and $\langle B_x \rangle$ are indicated in the figure. Then the first frame lag, I_{ff} , is defined as follows:

$$I_{ff} = \frac{B_t - B_0}{S}, \quad (5.4)$$

where B_t is the dark current measured at t second after the X-ray exposure is terminated and B_0 is the steady-state dark current defined as the dark current before any X-ray exposure. Average lag, I_{ave} , associated with the enhanced charge injection during X-ray exposure is defined as follows:

$$I_{\text{ave}} = \frac{\langle B_x \rangle - B_0}{S}, \quad (5.5)$$

Finally, ghosting is defined as follows:

$$g_n = \frac{S_n}{S_1}, \quad (5.6)$$

where S_1 and S_n are the X-ray sensitivity measured at the first and n^{th} X-ray exposure, respectively.

5.5.2 Experimental results

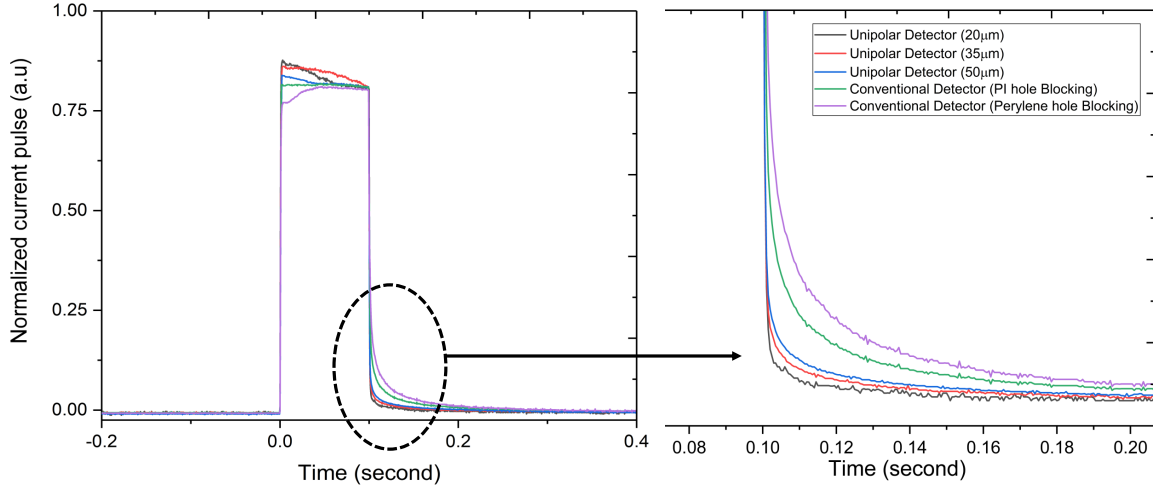


Figure 5.22: Photocurrent pulses obtained for first frame lag measurements by conventional and unipolar charge sensing devices.

Fig. 5.22 shows the measured transient signals from the unipolar charge sensing detectors with various grid pitch and conventional devices at $8 \text{ V}/\mu\text{m}$. The photocurrent lag was

measured as the residual percentage signal at 33 ms (30 Hz) after the termination of X-ray pulse. The measured first frame lag for conventional devices with perylene and polyimide is estimated at around 7% and 5% respectively. As reported with the previous studies, the cause of the photocurrent lag is identified with either de-trapping of the negative space charge or the increased charge injection. These results suggest that the increased charge injection plays a significant role in the temporal performance of the device. PI limits the charge injection more effectively as reported before; hence, the photocurrent lag is reduced compared to that of lag obtained with the conventional PTCBI hole blocking layer detector. On the other hand, the measured lag results with the unipolar charge sensing devices justify the second assumption that the cause of the lag can be de-rapping of the trapped charges as well. The measured lags with the unipolar charge sensing devices are all lower than 1% and decrease further with the smaller grid pitch. Also, the results indicate that further insensitivity to the slower carriers is achieved by establishing more effective electrostatic shielding with smaller pixel pitch, again agreeing well with the simulation results. We believe that the remaining lag observed with MPPC detectors is due to the de-trapping of holes in the bulk of a-Se.

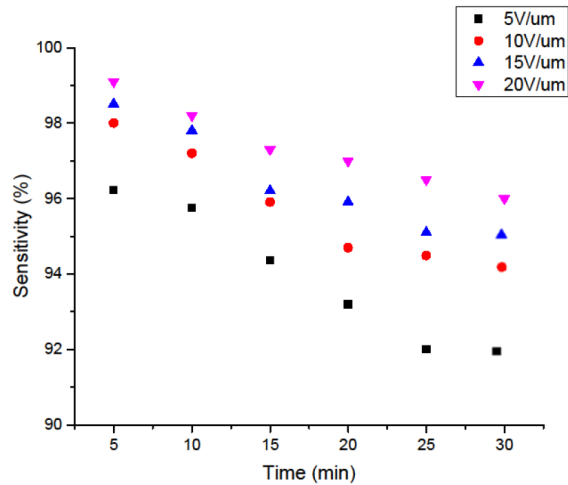


Figure 5.23: Ghosting measurement results for conventional detector as a function of accumulated dose for various applied field.

Fig. 5.23 illustrates the results of ghosting measurements obtained with the conventional detector as a function of the applied electric field with an uninterrupted 30 minutes of X-ray exposure (30 Hz). The results indicate that the rate of decrease in sensitivity increases with a lower electric field. This result agrees with our theoretical analysis and indicates that the rate of charge trapping is higher due to the shorter carrier drift range. Consequently, we have the highest sensitivity drop with an applied field of $5 \text{ V}/\mu\text{m}$, while the lower ghosting is observed at a higher electric field operation. This can be attributed to two main reasons. First, the carrier drift range is longer due to the higher electric field; thus, the charge trapping rate is lower. Second, charge injection rate is higher with the higher applied voltage. Therefore, the trapped charges recombine with the injected charges from the contact, mitigating the sensitivity reduction. For example, the lowest ghosting is seen with the applied field of $20 \text{ V}/\mu\text{m}$, which is only 4% after the 30 minutes of X-ray exposure. At the commonly used electrical field, $10 \text{ V}/\mu\text{m}$, the X-ray sensitivity drops to 95% after 30 minutes of exposure, which is acceptable for commercial FPDs. Note that the total dose used for ghosting measurement is 540 mR within 30 minutes of operation. We observed that the steady-state equilibrium between trapping and recombination of photo-induced charges is obtained after around 2 minutes.

In the presence of continuous X-ray pulse, the charge injection from the metal contact is enhanced due to the increased electric field at the metal/blocking layer interface. Also, the density of de-trapped charge increases with the increased density of the trapped charge until the equilibrium condition is reached. Therefore, the effect of lag can be emphasized more clearly with the measurement of the average lag, which imposes the real limitation with a-Se based detectors intended for real-time imaging. We measured the average lag of both conventional and the unipolar charge sensing detectors ($20\text{-}\mu\text{m}$ grid pitch) by irradiating with uninterrupted X-ray pulses similar to that of fluoroscopy for 10 minutes (e.g., 30 fps, 70 kVp, $10 \mu\text{R}/\text{pulse}$, 10 ms wide), where the X-ray pulse generator is programmed and triggered with a signal generator. We employed the PTCBI blocking layer for both devices, in which we observed almost no charge accumulation at the interface at $8 \text{ V}/\mu\text{m}$, thus a real-time measurement is possible. The average lag is measured. Fig. 5.24 shows the results,

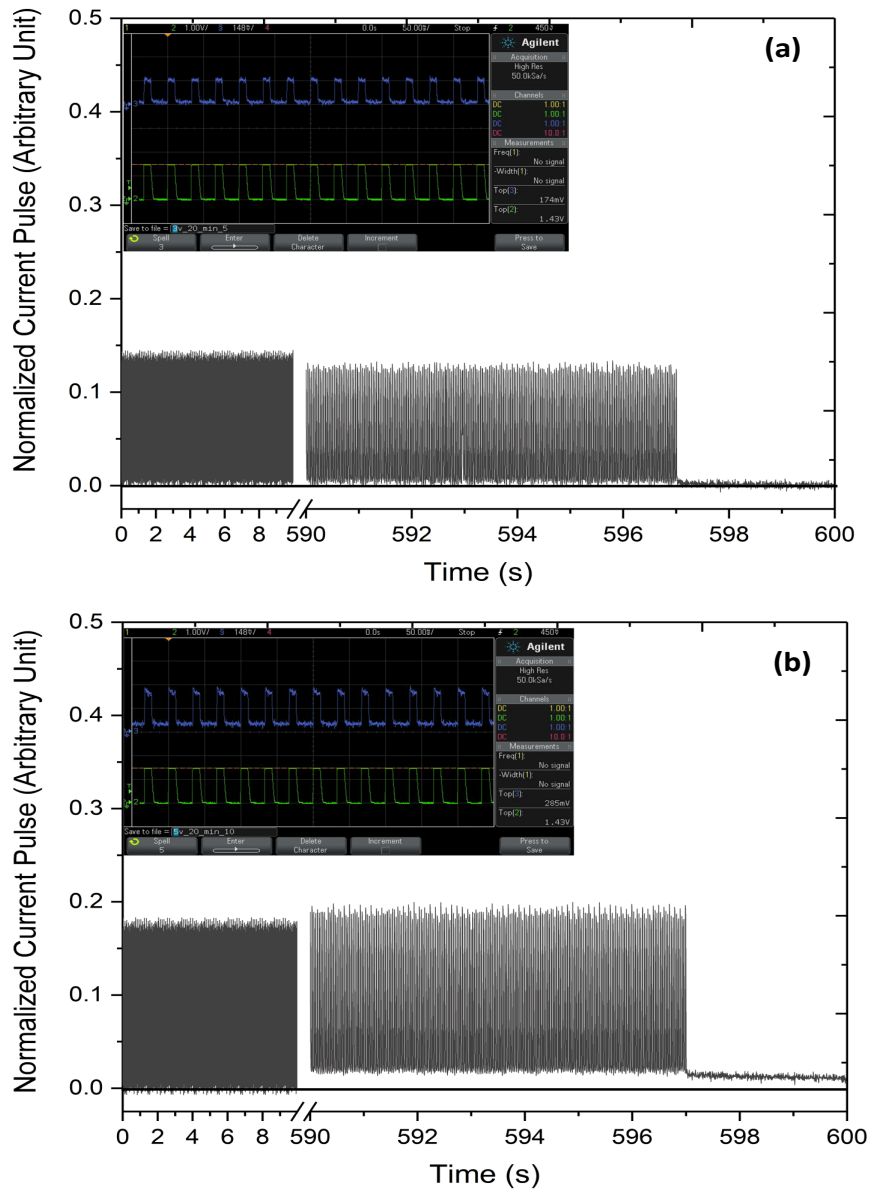


Figure 5.24: Photocurrent measurements results for average lag estimation a) Unipolar charge sensing device with 20- μm pixel b) Conventional a-Se device with PTCBI hole blocking layer.

where the measured average lag for conventional and unipolar charge sensing devices are estimated around 16% and 1.4%, respectively. Again, we observe a substantial reduction in the lag level and considerable improvement with temporal performance. Previous studies reported that the lag is the function of a cumulative dose. However, this measurement demonstrates that the lag is almost constant with the unipolar charge sensing device, even for the cumulative dose used for fluoroscopy.

5.6 Conclusion

In this chapter, we fabricated a-Se based unipolar charge sensing detectors with a various grid pitch, and demonstrated that the significant temporal resolution improvement can be achieved both for energy integration and photon counting mode of operations. The experimental setup for measuring the single photon counting capability of a-Se detectors via very low noise pulse height spectroscopy system has been implemented. It is clear from the experimental results that the energy resolution of conventional a-Se detectors can be improved when the low noise front-end electronics are employed. The energy resolution as low as 14.5 keV at 59.5 keV (^{241}Am) with a conventional a-Se detectors at 20 V/ μm has been achieved. The energy resolution of a-Se detectors are seen to increase with the higher electric field operation of the detectors if the low dark current in the detector is maintained. We demonstrated that unipolar charge sensing detectors provide an effective method to sense the collection of charges of one polarity type so that the poor collection of the opposite type of charges becomes unimportant. Transient signal measurements indicate that the depth-independent signal rise-time with the unipolar charge sensing detector is achieved with more than two orders of magnitude improvement compared to the conventional detectors rise-time, which is limited with the electron transit time across the a-Se layer. Significantly better energy (8.3 keV at 59.5 keV) and time resolution (~ 150 ns) than the obtained by conventional detectors are achieved with this unipolar charge sensing method, indicating its promise for the contrast-enhanced photon counting imaging. A

detailed analysis of memory artifacts related to the a-Se detectors have also been implemented to determine the feasibility of the use of a-Se photoconductor for dynamic X-ray imaging applications. Photocurrent lag of 16% has been measured with the conventional detector at the onset of 10 minutes long uninterrupted X-ray exposure, while the measured photocurrent lag is only 1.4% for the unipolar charge sensing detector for the same conditions. Given that the poor temporal response is the main impediment for realizing a-Se based dynamic imaging detectors, the fabricated unipolar charge sensing detector can be utilized for real-time imaging operations such as micro-angiography for imaging fine brain vessels with an unsurpassed spatial resolution.

Chapter 6

Amorphous Selenium Based CMOS-Integrated Single-Photon-Counting X-Ray Detector

6.1 Introduction

Large-area digital X-ray detectors are rapidly replacing X-ray film screen and computed radiography systems globally because of their better imaging performance and efficient work flows. However, X-ray detector technology still has considerable room for improvement in high-resolution and low-dose applications such as mammography and angiography, where lower radiation dose is essential for patient safety, and better contrast and spatial resolution can reduce medical diagnostic errors.

Single photon counting (SPC) X-ray detectors provide energy discrimination for improved image contrast and offer the advantages of lower noise and higher dynamic range compared to traditional integration-mode X-ray detectors [178][179]. However, current

SPC X-ray detector technology is limited to small-area imaging applications due to scaling constraints on both the X-ray sensor material and the readout integrated circuit (IC). With the recent advances in column-buttable CMOS IC technology, IC scaling constraints are mitigated, making the X-ray sensor a limiting step [180].

Existing X-ray sensor materials demonstrated for SPC applications detect X-rays directly and make use of primarily crystalline (e.g., Si) or poly-crystalline (e.g., CZT, CdTe) materials. However, these materials are challenging to scale to large-area medical applications because of yield and cost issues associated with the growth and bonding technology needed to interface the sensor with the readout IC.

An alternate approach is to use a large-area-compatible direct-X-ray-detection sensor such as poly-crystalline HgI_2 [181]. However, HgI_2 is not yet commercially available. A commercially viable alternative is amorphous selenium (a-Se), already the predominant technology for large-area mammography X-ray detectors. The technical challenges for photon counting with a-Se lie in overcoming (1) the slow carrier-transport properties of a-Se [23], which lead to count-rate limitations due to pile-up, and (2) low X-ray-to-charge conversion gain, which degrades SNR. In this chapter, we report, for the first time, the design and preliminary characterization of an a CMOS-integrated SPC detector with an a-Se photoconductor. Our design features ultra-small $11 \times 11\text{-}\mu\text{m}^2$ pixels which enable us to overcome the count-rate limitations imposed by a-Se by leveraging the small-pixel geometry with amorphous semiconductors [143]. We also employ a unique pixel circuit design to achieve sufficient SNR for photon counting with a-Se.

6.2 Sensor characterization

We quantify the count-rate limitations of our proposed SPC detector and show that by leveraging the small-pixel effect, we could achieve adequate detector performance for mammography. To potentially achieve higher spatial resolution compared to existing detectors, we design our prototype using $11 \times 11\text{-}\mu\text{m}^2$ pixels. Based on the expected maximum

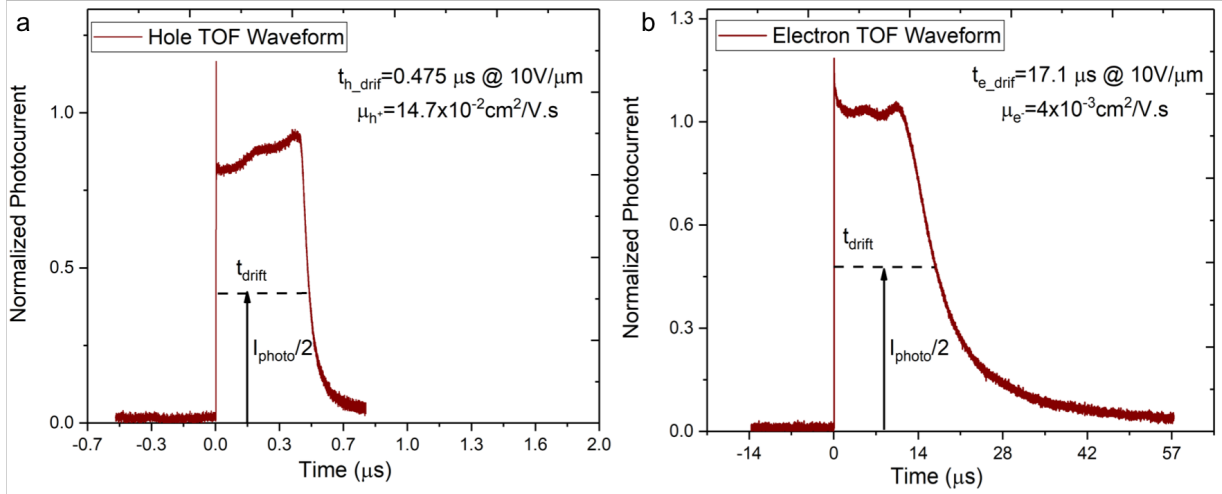


Figure 6.1: Time-of-flight (TOF) transient photoconductivity measurements of an a-Se sensor showing the response of (a) holes and (b) electrons.

incident flux of $108 \text{ photons/s/mm}^2$ for mammography [182], our pixels must support a maximum count rate C_{max} of $\sim 12 \times 10^3 \text{ photons/s/pixel}$.

However, our time-of-flight (TOF) measurements of a $100 - \text{mm}^2$ a-Se sensor show that the long electron transport time would prevent us from meeting C_{max} . Based on our TOF results shown in Fig. 6.1(a) and (b), we compute hole and electron mobilities of 0.147 and $0.004 \text{ cm}^2/\text{V.s}$, respectively. From these, we estimate hole drift time t_{h} and electron drift time t_{e} of $1.36 \mu\text{s}$ and $50 \mu\text{s}$, respectively, for a $200 - \mu\text{m}$ - thick a-Se sensor biased at a $10\text{V}/\mu\text{m}$ electric field (typical for mammography). Targeting a maximum pile-up probability P_p of 20% , we calculate the per-pixel count rate of the detector $C_d = -\ln(1 - P_p)/t_e \approx 1500 \text{ photons/s/pixel}$, which does not meet the C_{max} requirement.

Consequently, we choose to operate our SPC detector in a unipolar charge sensing regime to observe the faster carriers (holes), thereby masking the extended rise time due to slower carriers (electrons). This small pixel effect (SPE) is noticeable when pixel geometry is made significantly smaller than the sensor thickness. Repeating the above Cd calculation, but with the hole drift time t_{h} , we estimate an achievable count rate of 55×10^3

photons/s/pixel, exceeding C_{max} .

6.3 Detector design and implementation

The cross-section of our detector, shown in Fig. 6.2, consists of a $0.5\text{-}\mu\text{m}$ -thick continuous parylene stabilization layer deposited on individual top-metal Al pads (under an $8 \times 10\text{-}\mu\text{m}^2$ passivation opening) on the CMOS pixel array readout IC, a $70\text{-}\mu\text{m}$ -thick a-Se layer (deposited via thermal evaporation and shadow masking), and a 50-nm -thick Au top-contact to bias a-Se. As a proof-of-concept, we are employing an a-Se thickness about $3\times$ smaller than that used in a conventional mammography detector. The total applied bias voltage to a-Se is limited to 300 V (or $\sim 4\text{ V}/\mu\text{m}$) to protect our CMOS IC from high-voltage breakdown since no encapsulation layer is utilized. Nevertheless, we expect sufficient photon capture to characterize our detector using a mono-energetic 60-keV radioactive source.

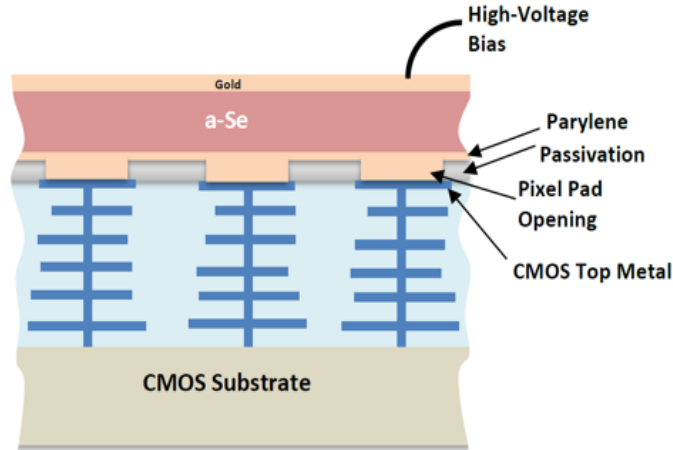


Figure 6.2: Simplified cross-section of the CMOS-integrated a-Se SPC X-ray detector.

Our $4 \times 3\text{ mm}^2$ SPC detector IC, shown in Fig. 6.3, is designed in a 1.8-V -supply, $0.18\text{-}\mu\text{m}$ mixed-signal CMOS (non-CIS) process and integrates two 26×196 SPC-pixel

arrays. Each $11 \times 11 - \mu\text{m}^2$ pixel is connected to a unique off-array 5-bit counter, to register single-photon events.

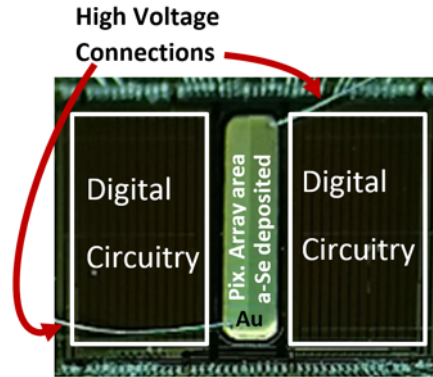


Figure 6.3: Photograph of the $4 \times 3\text{-mm}^2$ SPC X-ray detector IC.

We employ the pixel architecture shown in Fig. 6.4, with the timing diagram shown in Fig. 6.5. Generated charge from a captured photon is integrated on parasitic capacitance C_i , estimated at 20 fF, for a fixed period T_{int} before being reset (during a $0.3 - \mu\text{s}$ pixel dead time). We threshold the input voltage signal against a reference voltage V_{th} corresponding to the desired photon energy using offset-corrected 1st-stage comparator PA1 followed by gain stage PA2. The resolved logic value from PA2 is then latched and used to increment or hold the counter value. In our design, pixel input-referred noise is dominated by reset noise $Q_{nr} = (kTC_i)^{0.5}/q = 57 e_{rms}^-$ (at $T = 300$ K) and comparator input noise, leading to a total simulated noise Q_n of $\sim 90 e_{rms}^-$.

We use pulse-height spectroscopy (PHS) measurements to characterize the a-Se sensor layer. PHS results for a $70 - \mu\text{m}$ -thick $0.7 - \text{mm}^2$ a-Se sensor biased at 300 V are shown in Fig. 6.6, and indicate an ionization energy W_{\pm} of 78 eV for 60-keV photons. Based on these results, we estimate that a signal charge Q_i of 769 ehp is generated per captured 60-keV photon, leading to an estimated SNR for our SPC detector of $10 \log_{10}[Q_i^2/(Q_i + Q_n^2)] = 18.2$ dB. PHS measurements are also used to quantify the expected number of photon counts under the same conditions and parameters as for our integrated SPC detector.

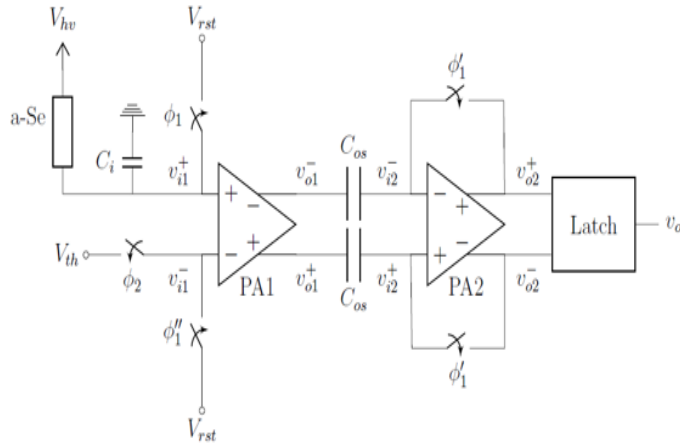


Figure 6.4: CMOS pixel circuit schematic, consisting of two amplifier stages followed by a latch. Capacitor C_i represents the parasitic input capacitance of the pixel. Output-offset correction of amplifier PA1 is implemented with capacitors C_{os} .

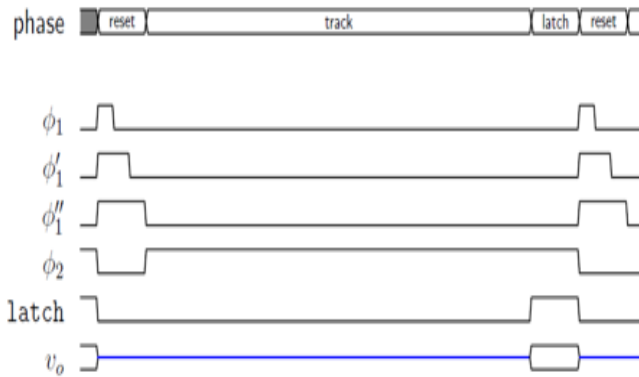


Figure 6.5: Timing diagram showing the three-phase operation of the CMOS pixel circuit. Reset dead time is $0.3\mu s$ and the integration (track) phase lasts for $9.7\mu s$.

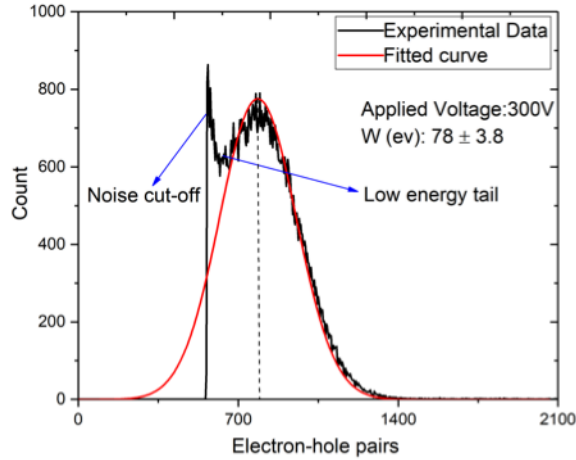


Figure 6.6: Calibrated pulse-height spectrum from measurement of a $70 - \mu m$ -thick a-Se sensor exposed to a mono-energetic $59.5\text{-keV } ^{241}\text{Am}$ source.

Semi-Gaussian output pulses, characterized with a $44 - \mu s$ peaking time, are acquired from a multi-channel analyzer for 120 min. In Fig. 6.6, the spectrum is seen above the background noise component. The total number of counts, calculated by integrating the area under the spectrum, is $87 \text{ kcounts}/\text{mm}^2$. Considering the $121 - \mu m^2$ pixel area of our SPC detector, the expected number of counts for the same exposure time is estimated at 7.2 counts/pixel.

6.4 Experimental results and discussion

We demonstrate photon-counting operation of our SPC detector using the experimental setup shown in Fig. 6.7 and a mono-energetic $60\text{-keV } ^{241}\text{Am}$ source. We measure an average of 5.5 counts/pixel for 80 adjacent pixels in one row of the detector over a 120-min period, which is comparable to the 7.2 counts/pixel estimated via PHS measurements. Fig.6.8 (a) displays the count results from these pixels with and without the source present. Hit probability versus estimated input charge for one pixel in the row is displayed in Fig. 6.8(b), showing an input-referred noise of $190 e_{rms}^-$. This is greater than the simulated

result and is caused by an anomalous source of interference on the particular chip under test. The detection histogram and variation in pixel threshold voltage are shown in Figs. 6.8(c) and (d), respectively. Based on the results obtained, we hypothesize that the SPE

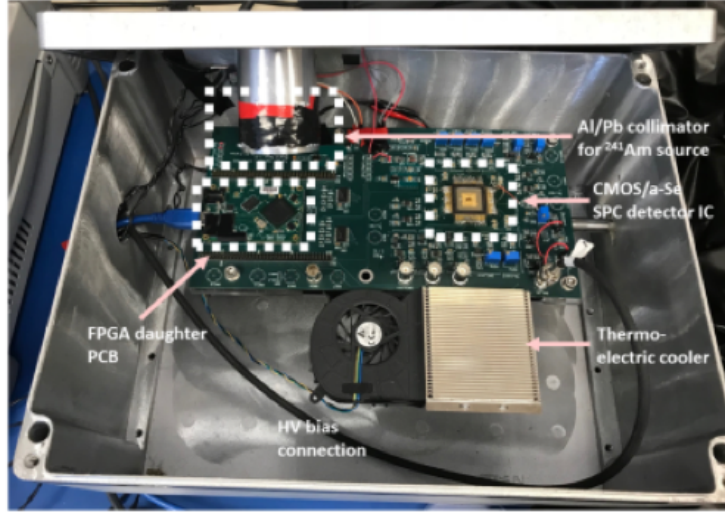


Figure 6.7: Experimental setup of the integrated a-Se SPC detector. The Al/Pb collimation tube attached to the lid (containing the radiation source) is aligned with the SPC chip surface using a precision stepper. The source to detector distance is 7 mm.

is enabling unipolar charge sensing in our detector, mitigating the impact of slow electron drift times in a-Se. Although we observed a $44 - \mu s$ electron drift time in a large-area $70 - \mu m$ -thick a-Se sensor, SPE enables use of the shorter $9.7 - \mu s$ integration time while maintaining a charge-collection efficiency that is close to unity in the integrated detector.

6.5 Conclusion

We have demonstrated, for the first time, single-X-ray-photon counting using an a-Se photoconductor integrated with a CMOS readout IC. The presented results are also unique because, to the best of our knowledge, the $11 \times 11 - \mu m^2$ pixel pitch is the smallest

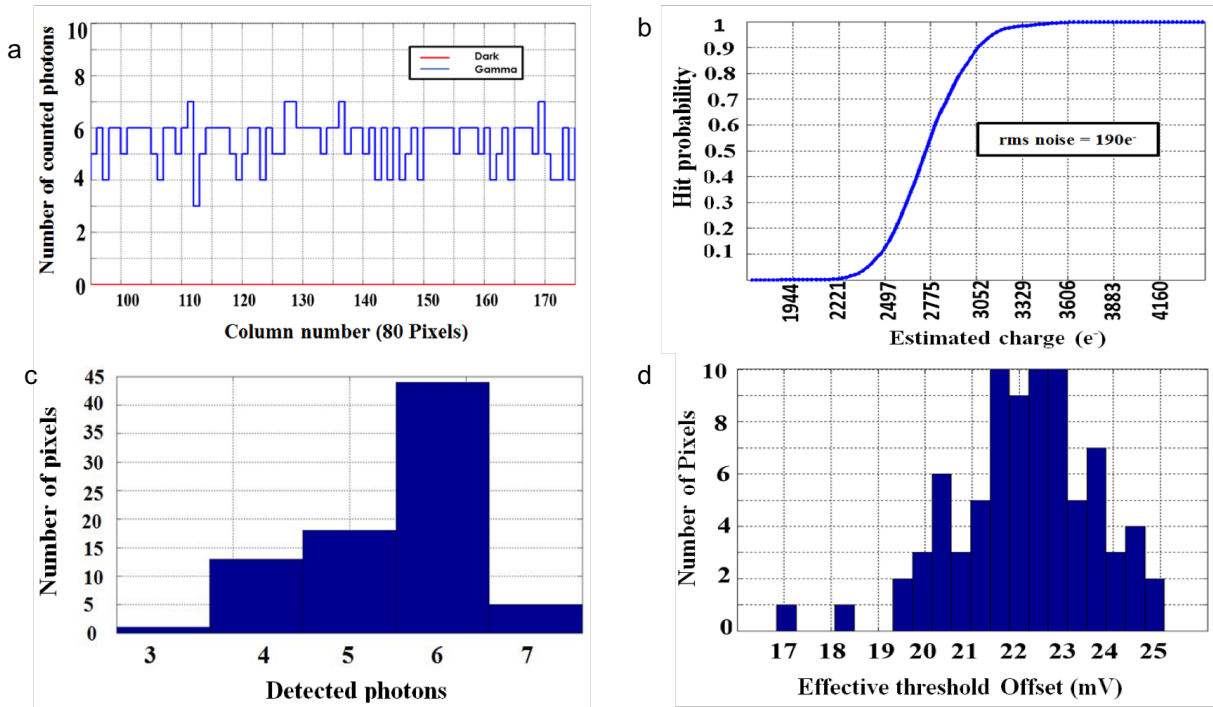


Figure 6.8: Measured counting results from 80 adjacent pixels in one row of the CMOS-integrated SPC detector when exposed to a mono-energetic 60-keV ^{241}Am source.(a)Counted photons per pixel with the radiation source present and absent (dark).(b)Hit probability versus input generated charge.(c)Histogram of detected photons.(d)Histogram counts for threshold offset.

reported for X-ray photon counting and this work reports the first demonstration of SPE for amorphous semiconductors.

This research indicates that by leveraging a combination of synergistic device and circuit architectures, amorphous material shortcomings related to slow carrier transport, noise, and gain can be overcome. The counting operation demonstrated with an a-Se photoconductor in this research indicates that well-established large-area a-Se can meet the requirements of emerging medical imaging applications such as photon-counting mammography or angiography without resorting to new sensor materials or crystalline semiconductors that are challenging to scale up to larger areas.

Chapter 7

Conclusions and Recommendations for Future Work

This thesis stemmed from the recognition that some of the inherent properties of a-Se make it an excellent candidate photoconductor for use in digital radiography. The research conducted in this thesis is primarily composed of three main parts: analytical modelling of a-Se detectors temporal performance, experiments carried out with a conventional a-Se to examine its intrinsic properties and the feasibility study for a-Se-based photon-counting detector with alternative device architectures. A number of important findings are summarized in this chapter and the possible future work as a natural extension of this thesis is discussed.

7.1 Conclusions

The thesis started with the investigation of the hole conduction mechanism in polyimide (PI) blocking layer to identify an optimum PI thickness and operation voltage for achieving optimum dark current performance with a-Se radiation detectors. Some electrical properties of PI layer when employed in a conventional a-Se detector were determined using the

characterization method common in high energy physics called pulse-height spectroscopy (PHS). A number of factors emerged as a primary technical limitation for designing selenium PHS system. PHS is a standard method for characterizing semiconductors used in charge particle spectrometers. Although the method itself has been discussed in literature, benchtop PHS systems have been used to characterize higher gain, faster crystalline and polycrystalline photoconductors. To characterize a-Se based detector, however, the PHS experimental setup needed to be optimized for a lower gain, and slower response. The lack of intrinsic gain and high ionization energy in a-Se (e.g., 42 eV at $10 \text{ V}/\mu\text{m}$) gave rise that the induced charge signal due to the single photon absorption was easily overwhelmed by the electronic noise. As a results, considerable effort was dedicated on designing and optimizing PHS system components.

We demonstrated, for the first time, the use of PHS to extract the internal electric field of an a-Se detector having a PI blocking layer. PHS enables more accurate measurement of the internal electric field of the detector because single-photon interactions in radiation detectors do not distort the internal electric field significantly. We fabricated a set of a-Se detectors, each having a PI layer with different thicknesses, and measured instantaneous electric field (i.e., 60 V for $1 \mu\text{m}$) within a-Se and PI layers using PHS, as well as the dark current of each detector. We also investigated detector response under X-ray pulse illumination to determine the optimal thickness of PI (i.e., $1.5\text{-}2 \mu\text{m}$) necessary to achieve the best photo-to-dark current ratio for low radiation dose imaging applications. Finally, we represented an analytical model of the steady-state dark current behavior and hole conduction mechanism in PI, which incorporates the Poole-Frankel emission model, and compared our model to experimental results. The PHS approach reported in this work can enable selection and design of optimal blocking layer material when integrated with existing (e.g., a-Se, CZT) and emerging direct conversion radiation semiconductors (e.g., PbO, TIBr).

The second part of the thesis comprises the comprehensive theoretical and experimental study of an a-Se to address the inherent poor charge transport properties. The analytical models were derived, and the simulation results were obtained for signal rise-time and

charge collection efficiency with both conventional and unipolar charge sensing detectors. These analysis provide a powerful method for understanding the detector behaviour to optimize detector design and configuration. Theoretical results showed that by operating an a-Se detector in unipolar charge sensing regime, hole-mostly signals are obtained, and the problem of poor electron transport becomes largely irrelevant.

We have fabricated three types of pixelated unipolar charge sensing detectors with various pixel pitch using standard lithography process. The PHS setup with a very low noise front-end electronics were designed, and experiments were performed to investigate the achievable time and energy resolution based on the unipolar charge sensing detectors. The energy resolution as low as 14.5 keV at 59.5 keV (Am241) with a conventional a-Se detectors at 20 V/ μm has been achieved. The energy resolution of a-Se detectors are seen to increase with the higher electric field operation of the detectors if the low dark current in the detector is maintained. We demonstrated that a unipolar charge sensing detectors provide an effective method to sense the collection of charges of one polarity type so that the poor collection of the opposite type of charges becomes unimportant. Transient signal measurements indicate that the depth-independent signal rise-time with the unipolar charge sensing detector is achieved with more than two orders of magnitude improvement compared to the conventional detectors rise-time, which is limited with the electron transit time across the a-Se layer. Significantly better energy resolution, ~ 8.3 keV at 59.5 keV, and time resolution, ~ 150 ns with 70- μm thick a-Se device, than the obtained by conventional detectors are achieved with this unipolar charge sensing method, indicating its promise for the contrast-enhanced photon counting imaging. A detailed analysis of memory artifacts related to the a-Se detectors have also been implemented to determine the feasibility of the use of a-Se photoconductor for dynamic X-ray imaging applications. Based on the photocurrent measurement results, the fabricated unipolar charge sensing device provides lower lag ($\sim 1.4\%$ vs. $\sim 16\%$ for 10 minutes long uninterrupted X-ray exposure) and higher temporal resolution through preferential charge sensing of the carriers with a higher mobility. Taking advantage of inherent high spatial resolution of a-Se, the unipolar charge sensing detector offers a potential to achieve avalanche gain for low noise

and high frame rate X-ray imaging applications, addressing two main limitations with a fluoroscopy imaging. Although the temporal and energy resolution improvements were shown for a-Se photoconductor with the implemented unipolar charge detection architecture, detectors based on other thermally evaporated semiconductors (e.g., PbO and HgI₂), being suffered from poor charge transport properties problem, can also benefit from this device architecture.

We reported, for the first time, results from a single photon-counting X-ray detector monolithically integrated with an amorphous semiconductor. Our prototype detector combines a-Se with a 0.18- μm -CMOS readout integrated circuit containing two 26×196 photon counting pixel arrays. The detector features $11 \times 11\text{-}\mu\text{m}$ pixels to overcome a-Se count-rate limitations by unipolar charge sensing of the faster charge carriers (holes) via a unique pixel geometry that leverages the small pixel effect for the first time in an amorphous semiconductor. Measured results from a mono-energetic radioactive source are presented and demonstrate the untapped potential of using amorphous semiconductors for high-spatial-resolution photon-counting X-ray imaging applications.

7.2 Recommendations for future work

Direct conversion a-Se detectors have been successfully used in commercial medical imaging detectors for its superior properties of high spatial resolution. However, the required photon-to-charge conversion energy of amorphous selenium in practical bias electric field of $10 \text{ V}/\mu\text{m}$ is one order of magnitude lower than the conversion energy of the other direct conversion materials such as CdTe or PbO. We demonstrated that the energy resolution of any detector is fundamentally limited with the number of photogenerated charges. It is therefore desirable to develop selenium imaging detector with a charge gain. Previous studies have shown that an avalanche gain with an a-Se due to the impact ionization is achievable under the applied field of $> 90 \text{ V}/\mu\text{m}$. However, one of the challenge is to maintain lower dark current while operating the detector at this applied field. By parti-

tioning the selenium detection layer to a low field charge absorption and drift region, and a high field region by using one or two layers of additional grid structures, avalanche gain can be obtained. In recent years, several research groups had explored this structure and variations of partitioning selenium field for charge collection and charge gain layers (2) (3). Fabricating this grid structure requires insulating material having a high dielectric strength to avoid hot spot electrical breakdown. Furthermore, the electric field strength across the gain region is non-uniform with stronger field near the wall of the well and weakest at the center of well or the trough. Image charges from different positions in the bulk will drift along the field line passing through the point of charge origin to the avalanche gain region. Non-uniform field strength distribution across the gain region will result in different avalanche gain for charges generated from even the same pixel. Since the gain factor increases extremely rapidly above the threshold field, the added image noise from this non-uniform gain distribution can make the image very noisy especially for low radiation dose applications. To stabilize the avalanche gain, some negative feedback circuit will also be needed to avoid *run-away avalanche* or high noise around the avalanche threshold potential.

One important extension of this thesis can be the use of our fabricated unipolar charge sensing structure to achieve a stable avalanche gain, or proportional gain, with a-Se detectors. The proper operation of the detector was proposed by Lee et al. [171]. Recall from the Fig. 5.2 showing the structure of the unipolar charge sensing detector that, during image charge accumulation, a negative potential is applied to the buried grid electrode. Positive charge from the selenium layer in the bulk are directed away from the pixel central electrode (near zero volt) and to the selenium/dielectric interface above the buried grid electrode. In readout mode, the voltage of one row of buried grid electrode is changed from negative to positive. With the reversal of the electric field at the dielectric interface with selenium, the collected positive image charge residing on that row will move to the outside rim of the respective central pixel electrode. One column of charge information will be collected by the array of charge amplifiers. This structure does not require TFT arrays and can be fabricated from just dielectric materials and conductive materials, as demon-

strated in section 5.2. A-Se with thickness sufficient to absorb the desired x-ray energy is deposited on this pixel array platform. Top charge blocking layer and a top electrode are deposited on to provide the bias electric field for image charge collection.

By switching the voltage of one column of buried electrode, the collected charges residing on the dielectric interface will move down the potential well and be integrated by the charge amplifiers. This action is repeated when the transfer of charges is completed. The voltage of this column will return to negative to continue collection of image charge and the voltage of the next column will change to positive for readout until the images charges from all the lines are readout. In dynamic imaging, this readout scheme can continue endlessly by transferring the charges from the first column right after the last column is readout. The voltage required to transfer the image charges accumulated on the dielectric area depends on the bias electric field in the bulk, the pixel size and the ratio of the linear dimension between the grid electrode and the central readout electrode, as investigated in section 5.4.2. The optimal condition for minimizing both the accumulation and readout grid voltage is when the edge of the pixel from the rim is similar to the radius of the central electrode. During readout, the electric field is converging at the rim of the readout electrode. All image charges accumulated during x-ray exposure need to drift along the dielectric interface to the rim of the pixel central electrode. For a high field ring of 80 volts or more, avalanche gain is achieved. Since all charges need to drift through the high field ring before reaching the readout electrode, similar gain factor is applied to all charges regardless of the point of charge origin. Non-uniform charge gain for different image charges in the bulk can therefore be avoided.

Since only positive charges (holes) transfer from the dielectric interface are moving through this converging field, and the counter charges (electrons) produced in the avalanche process are moving along the diverging field (in the opposite direction with weaker field strength) will not undergo secondary impact ionization, no *run-away avalanche* can be avoided. This is similar to a condition of a wire proportional counter. Because of these two factors (limited number of image charges available for transfer and converging electric field at the rim), proportional gain can be achieved from controlling the buried grid voltage

during readout mode. For smaller unit pixels such as $10\ \mu m$, less than 50V are needed to produce proportional gain. Since the bulk bias voltage can be maintained constant during charge accumulation and rolling line charge readout, this detector can be used for dynamic imaging with proportional gain.

Given that the energy resolution is improved substantially with a proportional avalanche gain, the fabricated unipolar charge sensing a-Se detectors, providing a stable avalanche gain, can be leveraged by dual energy discrimination allowing phenomenal color X-ray imaging. Full field X-ray panel with a-Se can be realized with acceptable count rate and energy resolution. Colour X-ray imaging can be used to identify some diseases such as brittle-bone disease. Besides, the improved photon counting rate with the unipolar charge sensing regime can lead to realization of a-Se based micro-dose contrast enhanced mammography with an unsurpassed spatial resolution.

References

- [1] W. Zhao and J. A. Rowlands. X-ray imaging using amorphous selenium: feasibility of a flat panel self-scanned detector for digital radiology. *Medical Physics*, 22(10):1595–1604, October 1995.
- [2] S. O. Kasap, M. Zahangir Kabir, and J. A. Rowlands. Recent advances in X-ray photoconductors for direct conversion X-ray image detectors. *Current Applied Physics*, 6(3):288–292, June 2006.
- [3] S. Kasap, J. B. Frey, G. Belev, O. Tousignant, H. Mani, L. Laperriere, A. Reznik, and J. A. Rowlands. Amorphous selenium and its alloys from early xeroradiography to high resolution X-ray image detectors and ultrasensitive imaging tubes. *physica status solidi (b)*, 246(8):1794–1805, 2009.
- [4] S. Abbaszadeh. Indirect conversion amorphous selenium photodetectors for medical imaging applications. PhD Thesis. January 2014.
- [5] M. Abkowitz. Density of states in a-Se from combined analysis of xerographic potentials and transient transport data. *Philosophical Magazine Letters*, 58(1):53–57, July 1988.
- [6] J. M. Boone, M. H. Buonocore, and V. N. Cooper. Monte Carlo validation in diagnostic radiological imaging. *Medical Physics*, 27(6):1294–1304, June 2000.

- [7] E. A. Davis and N. F. Mott. Conduction in non-crystalline systems V. Conductivity, optical absorption and photoconductivity in amorphous semiconductors. *The Philosophical Magazine: A Journal of Theoretical Experimental and Applied Physics*, 22(179):0903–0922, November 1970.
- [8] J. L. Hartke. The ThreeDimensional PooleFrenkel Effect. *Journal of Applied Physics*, 39(10):4871–4873, September 1968.
- [9] C. J. Haugen. Charge transport in stabilized A-Se films used in X-ray image detector applications. *PhD Thesis*, January 1999.
- [10] M. Martini, J. W. Mayer, and K. R. Zanio. Drift Velocity and Trapping in SemiconductorsTransient Charge Technique. In Raymond Wolfe, editor, *Applied Solid State Science*, volume 3, pages 181–261. Elsevier, January 1972.
- [11] J. H. Hubbell and S. M. Seltzer. X-ray mass attenuation coefficients. NIST standard reference database 126. [<https://dx.doi.org/10.18434/t4d01f>]. Technical report, Radiation Physics Division, PML, NIST, 2004.
- [12] Y. Fang, A. Badal, N. Allec, K. S. Karim, and A. Badano. Spatiotemporal Monte Carlo transport methods in x-ray semiconductor detectors: Application to pulse-height spectroscopy in a-Se: Monte Carlo methods in semiconductor x-ray detectors. *Medical Physics*, 39(1):308–319, December 2011.
- [13] I. M. Blevis, D. C. Hunt, and J. A. Rowlands. Measurement of x-ray photogeneration in amorphous selenium. *Journal of Applied Physics*, 85(11):7958–7963, May 1999.
- [14] I. M. Blevis, D. C. Hunt, and J. A. Rowlands. X-ray imaging using amorphous selenium: Determination of Swank factor by pulse height spectroscopy. *Medical Physics*, 25(5):638–641, May 1998.
- [15] J. Stavro, A. H. Goldan, and W. Zhao. Photon counting performance of amorphous selenium and its dependence on detector structure. *Journal of Medical Imaging*, 5(4):043502, October 2018.

- [16] S. Abbaszadeh, C. C. Scott, O. Bubon, A. Reznik, and K. S. Karim. Enhanced Detection Efficiency of Direct Conversion X-ray Detector Using Polyimide as Hole-Blocking Layer. *Scientific Reports*, 3:3360, November 2013.
- [17] A. Sultana, A. Reznik, K. S. Karim, and J. A. Rowlands. Design and feasibility of active matrix flat panel detector using avalanche amorphous selenium for protein crystallography. *Medical Physics*, 35(10):4324–4332, 2008.
- [18] A. Sultana, K. S. Karim, and J. A. Rowlands. The effect of K- fluorescence reabsorption of selenium on the performance of an imaging detector for protein crystallography. *physica status solidi c*, 6(S1):S231–S235, 2009.
- [19] J. Beutel, H. L. Kundel, and R. L. V. Metter. *Handbook of Medical Imaging*. SPIE Press, 2000.
- [20] E. L. Gingold, D. L. Y. Lee, L. S. Jeromin, B. G. Rodricks, M. G. Hoffberg, and C. L. Williams. Development of a novel high-resolution direct conversion x-ray detector. In *Medical Imaging 2000: Physics of Medical Imaging*, volume 3977, pages 185–193. International Society for Optics and Photonics, April 2000.
- [21] M. Galanti, R. Gott, and J. F. Renaud. A High Resolution, High Sensitivity Channel Plate Image Intensifier for Use in Particle Spectrographs. *Review of Scientific Instruments*, 42(12):1818–1822, December 1971.
- [22] D. C. Hunt, O. Tousignant, and J. A. Rowlands. Evaluation of the imaging properties of an amorphous selenium-based flat panel detector for digital fluoroscopy. *Medical Physics*, 31(5):1166–1175, May 2004.
- [23] S. Kasap, J. B. Frey, G. Belev, O. Tousignant, Habib Mani, J. Greenspan, L. Laperriere, O. Bubon, A. Reznik, G. DeCrescenzo, K. S. Karim, and J. A. Rowlands. Amorphous and Polycrystalline Photoconductors for Direct Conversion Flat Panel X-Ray Image Sensors. *Sensors*, 11(5):5112–5157, May 2011.

- [24] D. L. Y. Lee, L. K. Cheung, and L. S. Jeromin. New digital detector for projection radiography. In *Medical Imaging 1995: Physics of Medical Imaging*, volume 2432, pages 237–249. International Society for Optics and Photonics, May 1995.
- [25] E. Samei and M. J. Flynn. An experimental comparison of detector performance for direct and indirect digital radiography systems. *Medical Physics*, 30(4):608–622, 2003.
- [26] J. A. Rowlands, W. G. Ji, W. Zhao, and D. L. Y. Lee. Direct-conversion flat-panel x-ray imaging: reduction of noise by presampling filtration. In *Medical Imaging 2000: Physics of Medical Imaging*, volume 3977, pages 446–455. International Society for Optics and Photonics, April 2000.
- [27] C. M. Castelli, N. M. Allinson, K. J. Moon, and D. L. Watson. High spatial resolution scintillator screens coupled to CCD detectors for X-ray imaging applications. *Nuclear Instruments and Methods in Physics Research Section A: Accelerators, Spectrometers, Detectors and Associated Equipment*, 348(2):649–653, September 1994.
- [28] M. J. Yaffe and J. A. Rowlands. X-ray detectors for digital radiography. *Physics in Medicine and Biology*, 42(1):1–39, January 1997.
- [29] S. O. Kasap and J. A. Rowlands. Direct-conversion flat-panel X-ray image sensors for digital radiography. *Proceedings of the IEEE*, 90(4):591–604, April 2002.
- [30] B. T. Polischuk, Z. Shukri, A. Legros, and H. Rougeot. Selenium direct-converter structure for static and dynamic x-ray detection in medical imaging applications. In *Proc. SPIE*, volume 3336, pages 494–505, July 1998.
- [31] S. Tokuda, H. Kishihara, S. Adachi, T. Sato, Yoshihiro Izumi, O. Teranuma, Y. Yamane, and S. Yamada. Large-area deposition of a polycrystalline CdZnTe film and its applicability to x-ray panel detectors with superior sensitivity. In *Medical Imaging 2002: Physics of Medical Imaging*, volume 4682, pages 30–41. International Society for Optics and Photonics, May 2002.

- [32] S. Adachi, N. Hori, K. Sato, S. Tokuda, Toshiyuki Sato, K. Uehara, Y. Izumi, H. Nagata, Y. Yoshimura, and S. Yamada. Experimental evaluation of a-Se and CdTe flat-panel x-ray detectors for digital radiography and fluoroscopy. In *Medical Imaging 2000: Physics of Medical Imaging*, volume 3977, pages 38–47. International Society for Optics and Photonics, April 2000.
- [33] W. C. Barber, E. Nygard, J. C. Wessel, N. Malakhov, Gregor Wawrzyniak, N. E. Hartsough, T. Gandhi, and J. S. Iwanczyk. Fast photon counting CdTe detectors for diagnostic clinical CT: dynamic range, stability, and temporal response. In *Medical Imaging 2010: Physics of Medical Imaging*, volume 7622, page 76221E. International Society for Optics and Photonics, March 2010.
- [34] P. M. Shikhaliev, S. G. Fritz, and J. W. Chapman. Photon counting multienergy x-ray imaging: Effect of the characteristic x rays on detector performance. *Medical Physics*, 36(11):5107–5119, 2009.
- [35] E. A. Davis. Optical absorption, transport and photoconductivity in amorphous selenium. *Journal of Non-Crystalline Solids*, 4:107–116, April 1970.
- [36] J. L. Hartke. Drift Mobilities of Electrons and Holes and Space-Charge-Limited Currents in Amorphous Selenium Films. *Physical Review*, 125(4):1177–1192, February 1962.
- [37] M. L. Benkhedir, M. Brinza, and G. J. Adriaenssens. Electronic density of states in amorphous selenium. *Journal of Physics: Condensed Matter*, 16(44):S5253–S5264, October 2004.
- [38] K. Koughia, Z. Shakoor, S. O. Kasap, and J. M. Marshall. Density of localized electronic states in a-Se from electron time-of-flight photocurrent measurements. *Journal of Applied Physics*, 97(3):033706, January 2005.

- [39] R. E. Tallman, B. A. Weinstein, A. Reznik, M. Kubota, K. Tanioka, and J. A. Rowlands. Photo-crystallization in a-Se imaging targets: Raman studies of competing effects. *Journal of Non-Crystalline Solids*, 354(40):4577–4581, October 2008.
- [40] K. S. Kim and D. Turnbull. Crystallization of amorphous selenium films. II. Photo and impurity effects. *Journal of Applied Physics*, 45(8):3447–3452, August 1974.
- [41] B. Fogal, R. E. Johanson, G. Belev, S. O’Leary, and S. O Kasap. X-ray induced effects in stabilized a-Se X-ray photoconductors. *Journal of Non-Crystalline Solids*, 299-302:993–997, April 2002.
- [42] S. O. Kasap, K. V. Koughia, B. Fogal, G. Belev, and R. E. Johanson. The influence of deposition conditions and alloying on the electronic properties of amorphous selenium. *Semiconductors*, 37(7):789–794, July 2003.
- [43] M. Choquette, Y. Demers, Z. Shukri, O. Tousignant, Kunio Aoki, M. Honda, A. Takahashi, and A. Tsukamoto. Performance of a real-time selenium-based x-ray detector for fluoroscopy. In *Medical Imaging 2001: Physics of Medical Imaging*, volume 4320, pages 501–508. International Society for Optics and Photonics, June 2001.
- [44] Wei Zhao, W. G. Ji, Anne Debrie, and J. A. Rowlands. Imaging performance of amorphous selenium based flat-panel detectors for digital mammography: characterization of a small area prototype detector. *Medical Physics*, 30(2):254–263, February 2003.
- [45] S. O. Kasap and J. A. Rowlands. Review X-ray photoconductors and stabilized a-Se for direct conversion digital flat-panel X-ray image-detectors. *Journal of Materials Science: Materials in Electronics*, 11(3):179–198, April 2000.
- [46] W. E. Spear. The Hole Mobility in Selenium. *Proceedings of the Physical Society*, 76(6):826–832, December 1960.

- [47] G. S. Belev, Bud Fogal, K. V. Koughia, R. E. Johanson, and S. O. Kasap. Dependence of charge-carrier ranges in stabilized a-Se on preparation conditions and alloying. *Journal of Materials Science: Materials in Electronics*, 14(10):841–842, October 2003.
- [48] H G Chotas, C E Floyd, and C E Ravin. Memory artifact related to selenium-based digital radiography systems. *Radiology*, 203(3):881–883, June 1997.
- [49] S. O. Kasap. Charge Transport in Selenium Based Amorphous Xerographic Photoreceptors. page 275.
- [50] A. H. Goldan, J. A. Rowlands, O. Tousignant, and K. S. Karim. Unipolar time-differential charge sensing in non-dispersive amorphous solids. *Journal of Applied Physics*, 113(22):224502, June 2013.
- [51] S. Abbaszadeh, S. Ghaffari, S. Siddiquee, M. Z. Kabir, and K. S. Karim. Characterization of Lag Signal in Amorphous Selenium Detectors. *IEEE Transactions on Electron Devices*, 63(2):704–709, February 2016.
- [52] S. Siddiquee and M. Z. Kabir. Modeling of photocurrent and lag signals in amorphous selenium x-ray detectors. *Journal of Vacuum Science & Technology A*, 33(4):041514, June 2015.
- [53] N. Safavian, M. Yazdandoost, D. Wu, M. H. Izadi, K. S. Karim, and J. A. Rowlands. Investigation of gain non-uniformities in the two TFT current programmed amorphous silicon active pixel sensor for fluoroscopy, chest radiography, and mammography tomosynthesis applications. In *Medical Imaging 2010: Physics of Medical Imaging*, volume 7622, page 76221N. International Society for Optics and Photonics, March 2010.
- [54] K. S. Karim, A. Nathan, and J. A. Rowlands. Amorphous silicon active pixel sensor readout circuit for digital imaging. *IEEE Transactions on Electron Devices*, 50(1):200–208, January 2003.

- [55] C. D. Arvanitis, S. E. Bohndiek, G. Royle, A. Blue, H. X. Liang, A. Clark, M. Pryderch, R. Turchetta, and R. Speller. Empirical electro-optical and x-ray performance evaluation of CMOS active pixels sensor for low dose, high resolution x-ray medical imaging. *Medical Physics*, 34(12):4612–4625, 2007.
- [56] S. Abbaszadeh, K. S. Karim, and V. Karanassios. Measurement of UV from a Microplasma by a Microfabricated Amorphous Selenium Detector. *IEEE Transactions on Electron Devices*, 60(2):880–883, February 2013.
- [57] R. N. Cahn, B. Cederstrm, M. Danielsson, A. Hall, M. Lundqvist, and D. Nygren. Detective quantum efficiency dependence on x-ray energy weighting in mammography. *Medical Physics*, 26(12):2680–2683, 1999.
- [58] H. Bornefalk and M. Lundqvist. Dual-energy imaging using a photon counting detector with electronic spectrum-splitting. In *Medical Imaging 2006: Physics of Medical Imaging*, volume 6142, page 61421H. International Society for Optics and Photonics, March 2006.
- [59] A. Camlica, A. El-Falou, R. Mohammadi, P. M. Levine, and K. S. Karim. CMOS-Integrated Single-Photon-Counting X-Ray Detector using an Amorphous-Selenium Photoconductor with 11-by-11 um Pixels. In *2018 IEEE International Electron Devices Meeting (IEDM)*, pages 32.5.1–32.5.4, December 2018.
- [60] J. Giersch, D. Niederlhner, and G. Anton. The influence of energy weighting on X-ray imaging quality. *Nuclear Instruments and Methods in Physics Research Section A: Accelerators, Spectrometers, Detectors and Associated Equipment*, 531(1):68–74, September 2004.
- [61] P. M. Shikhaliev. Beam hardening artefacts in computed tomography with photon counting, charge integrating and energy weighting detectors: a simulation study. *Physics in Medicine and Biology*, 50(24):5813–5827, December 2005.

- [62] M. Rabbani, R. Shaw, and R. V. Metter. Detective quantum efficiency of imaging systems with amplifying and scattering mechanisms. *JOSA A*, 4(5):895–901, May 1987.
- [63] I. A. Cunningham and R. Shaw. Signal-to-noise optimization of medical imaging systems. *JOSA A*, 16(3):621–632, March 1999.
- [64] R. Shaw. The Equivalent Quantum Efficiency of the Photographic Process. *The Journal of Photographic Science*, 11(4):199–204, July 1963.
- [65] W. Zhao and J. A. Rowlands. Digital radiology using active matrix readout of amorphous selenium: Theoretical analysis of detective quantum efficiency. *Medical Physics*, 24(12):1819–1833, 1997.
- [66] J A Rowlands, W Zhao, I M Blevis, D F Waechter, and Z Huang. Flat-panel digital radiology with amorphous selenium and active-matrix readout. *RadioGraphics*, 17(3):753–760, May 1997.
- [67] J. F. Hainfeld, F. A. Dilmanian, D. N. Slatkin, and H. M. Smilowitz. Radiotherapy enhancement with gold nanoparticles. *Journal of Pharmacy and Pharmacology*, 60(8):977–985, 2008.
- [68] M. F. Stone, W. Zhao, B. V. Jacak, P. O’Connor, B. Yu, and P. Rehak. The x-ray sensitivity of amorphous selenium for mammography. *Medical Physics*, 29(3):319–324, February 2002.
- [69] W. Que and J. A. Rowlands. X-ray imaging using amorphous selenium: Inherent spatial resolution. *Medical Physics*, 22(4):365–374, 1995.
- [70] M. Nevill. Conduction in amorphous materials. *Electronics and Power*, 19(14):321–324, August 1973.
- [71] W. E. Spear. Electronic transport and localization in low mobility solids and liquids. *Advances in Physics*, 23(3):523–546, May 1974.

- [72] F. K. Dolezalek and W. E. Spear. Electronic transport properties of some low mobility solids under high pressure. *Journal of Non-Crystalline Solids*, 4:97–106, April 1970.
- [73] S. O. Kasap and C. Juhasz. Time-of-flight drift mobility measurements on chlorine-doped amorphous selenium films. *Journal of Physics D: Applied Physics*, 18(4):703–720, April 1985.
- [74] S. M. Vaezi-Nejad. Xerographic time of flight experiment for the determination of drift mobility in high resistivity semiconductors. *International Journal of Electronics*, 62(3):361–384, March 1987.
- [75] H. Scher and E. W. Montroll. Anomalous transit-time dispersion in amorphous solids. *Physical Review B*, 12(6):2455–2477, September 1975.
- [76] G. Pfister. Hopping transport in a molecularly doped organic polymer. *Physical Review B*, 16(8):3676–3687, October 1977.
- [77] U. Neitzel, I. Maack, and S. Gnther-Kohfahl. Image quality of a digital chest radiography system based on a selenium detector. *Medical Physics*, 21(4):509–516, April 1994.
- [78] G. Zentai, L. Partain, M. Richmond, K. Ogusu, and S. Yamada. 50 m pixel size a-Se mammography imager with high DQE and increased temperature resistance. In *Medical Imaging 2010: Physics of Medical Imaging*, volume 7622, page 762215. International Society for Optics and Photonics, March 2010.
- [79] J. H. Siewerdsen, L. E. Antonuk, Y. el Mohri, J. Yorkston, W. Huang, J. M. Boudry, and I. A. Cunningham. Empirical and theoretical investigation of the noise performance of indirect detection, active matrix flat-panel imagers (AMFPIs) for diagnostic radiology. *Medical Physics*, 24(1):71–89, January 1997.
- [80] M. Z. Kabir, M. W. Rahman, and W. Y. Shen. Modelling of detective quantum efficiency of direct conversion x-ray imaging detectors incorporating charge carrier

trapping and K-fluorescence. *IET Circuits, Devices Systems*, 5(3):222–231, May 2011.

- [81] I. A. Cunningham. Linear-systems modeling of parallel cascaded stochastic processes: the NPS of radiographic screens with reabsorption of characteristic x-radiation. In *Medical Imaging 1998: Physics of Medical Imaging*, volume 3336, pages 220–230. International Society for Optics and Photonics, July 1998.
- [82] G. Belev and S. O. Kasap. Amorphous selenium as an X-ray photoconductor. *Journal of Non-Crystalline Solids*, 345-346:484–488, October 2004.
- [83] I. Chen and J. Mort. Xerographic Discharge Characteristics of Photoreceptors. *Journal of Applied Physics*, 43(3):1164–1170, March 1972.
- [84] K. Hecht. Zum Mechanismus des lichtelektrischen Primrstromes in isolierenden Kristallen. *Zeitschrift fr Physik*, 77(3):235–245, March 1932.
- [85] A. Owens. *Compound Semiconductor Radiation Detectors*. Taylor & Francis, April 2016. Google-Books-ID: zTHOBQAAQBAJ.
- [86] M. Z. Kabir. Dark current mechanisms in amorphous selenium-based photoconductive detectors: an overview and re-examination. *Journal of Materials Science: Materials in Electronics*, 26(7):4659–4667, July 2015.
- [87] R. E. Johanson, S O. Kasap, J Rowlands, and B Polischuk. Metallic electrical contacts to stabilized amorphous selenium for use in X-ray image detectors. *Journal of Non-Crystalline Solids*, 227-230:1359–1362, May 1998.
- [88] S. A. Mahmood, M. Z. Kabir, O. Tousignant, H. Mani, J. Greenspan, and P. Botka. Dark current in multilayer amorphous selenium x-ray imaging detectors. *Applied Physics Letters*, 92(22):223506, June 2008.

- [89] G. Pfister and A. I. Lakatos. One-Carrier and Two-Carrier Steady-State Space-Charge-Limited Currents in Amorphous Selenium Films. *Physical Review B*, 6(8):3012–3018, October 1972.
- [90] V. I. Arkhipov, E. V. Emelianova, Y. H. Tak, and H. Bessler. Charge injection into light-emitting diodes: Theory and experiment. *Journal of Applied Physics*, 84(2):848–856, June 1998.
- [91] S. Abbaszadeh, N. Allec, and K. Karim. Characterization of Low Dark-Current Lateral Amorphous-Selenium Metal-Semiconductor-Metal Photodetectors. *IEEE Sensors Journal*, 13(5):1452–1458, May 2013.
- [92] S. Abbaszadeh, N. Allec, S. Ghanbarzadeh, U. Shafique, and K. S. Karim. Investigation of Hole-Blocking Contacts for High-Conversion-Gain Amorphous Selenium Detectors for X-Ray Imaging. *IEEE Transactions on Electron Devices*, 59(9):2403–2409, September 2012.
- [93] Y. Fang, D. Sharma, A. Badal, K. S. Karim, and Aldo Badano. Monte Carlo Simulation of a-Se X-ray Detectors for Breast Imaging: Effect of Nearest-Neighbor Recombination Algorithm on Swank Noise. In A. D. A. Maidment, Predrag R. Bakic, and S. Gavenonis, editors, *Breast Imaging*, Lecture Notes in Computer Science, pages 575–582. Springer Berlin Heidelberg, 2012.
- [94] M. Maolinbay, Y. El-Mohri, L. E. Antonuk, K. W. Jee, S. Nassif, X. Rong, and Q. Zhao. Additive noise properties of active matrix flat-panel imagers. *Medical Physics*, 27(8):1841–1854, August 2000.
- [95] M. Lundqvist, B. Cederstrom, V. Chmill, M. Danielsson, and B. Hasegawa. Evaluation of a photon-counting X-ray imaging system. *IEEE Transactions on Nuclear Science*, 48(4):1530–1536, August 2001.

- [96] N. Mail, P. O'Brien, and G. Pang. Lag correction model and ghosting analysis for an indirectconversion flatpanel imager. *Journal of Applied Clinical Medical Physics*, 8(3):137–146, July 2007.
- [97] B. Zhao and W. Zhao. Temporal performance of amorphous selenium mammography detectors. *Medical Physics*, 32(1):128–136, January 2005.
- [98] O. Tousignant, M. Choquette, Y. Demers, L. Laperriere, Jonathan Leboeuf, M. Honda, M. Nishiki, A. Takahashi, and A. Tsukamoto. Progress report on the performance of real-time selenium flat-panel detectors for direct x-ray imaging. In *Proc. SPIE*, volume 4682, pages 503–511, May 2002.
- [99] K. S. Karim, A. Nathan, J. A. Rowlands, and S. O. Kasap. X-ray detector with on-pixel amplification for large area diagnostic medical imaging. *IEE Proceedings - Circuits, Devices and Systems*, 150(4):267–273, August 2003.
- [100] M. Simon, K. J. Engel, B. Menser, X. Badel, and J. Linnros. Challenges of pixelated scintillators in medical X-ray imaging. *Nuclear Instruments and Methods in Physics Research Section A: Accelerators, Spectrometers, Detectors and Associated Equipment*, 591(1):291–295, June 2008.
- [101] J. G. Yorker, L. S. Jeromin, D. L. Y. Lee, E. F. Palecki, K. P. Golden, and Z. Jing. Characterization of a full-field digital mammography detector based on direct x-ray conversion in selenium. In *Proc. SPIE*, volume 4682, pages 21–30, May 2002.
- [102] H. K. Kim, I. A. Cunningham, Zhye Yin, and Gyuseong Cho. On the Development of Digital Radiography Detectors : A Review. 9(4):15.
- [103] S. A. Mahmood and M. Z. Kabir. Dark current mechanisms in stabilized amorphous selenium based n-i detectors for x-ray imaging applications. *Journal of Vacuum Science & Technology A*, 29(3):031603, April 2011.

- [104] J. B. Frey, G. Belev, O. Tousignant, H. Mani, L. Laperriere, and S. O. Kasap. Dark current in multilayer stabilized amorphous selenium based photoconductive x-ray detectors. *Journal of Applied Physics*, 112(1):014502, July 2012.
- [105] A. Camlica, D. L. Lee, and K. S. Karim. Increased temporal resolution of amorphous selenium detector using preferential charge sensing approach. In *Proc. SPIE*, volume 10573, page 105735W, March 2018.
- [106] K. Kikuchi, Y. Ohkawa, K. Miyakawa, T. Matsubara, K. Tanioka, M. Kubota, and N. Egami. Hole-blocking mechanism in high-gain avalanche rushing amorphous photoconductor (HARP) film. *Physica Status Solidi (b)*, 8(9):2800–2803, 2011.
- [107] S. Abbaszadeh, A. Tari, W. S. Wong, and K. S. Karim. Enhanced Dark Current Suppression of Amorphous Selenium Detector With Use of IGZO Hole Blocking Layer. *IEEE Transactions on Electron Devices*, 61(9):3355–3357, September 2014.
- [108] N. R. Tu and K. C. Kao. High-field electrical conduction in polyimide films. *Journal of Applied Physics*, 85(10):7267–7275, May 1999.
- [109] S. Diaham and M. L. Locatelli. Space-charge-limited currents in polyimide films. *Applied Physics Letters*, 101(24):242905, December 2012.
- [110] S. Ghaffari, S. Abbaszadeh, S. Ghanbarzadeh, and K. S. Karim. Characterization of Optically Sensitive Amorphous Selenium Photodetector at High Electric Fields. *IEEE Transactions on Electron Devices*, 62(7):2364–2366, July 2015.
- [111] J. A. Rowlands, G. DeCrescenzo, and N. Araj. X-ray imaging using amorphous selenium: Determination of x-ray sensitivity by pulse height spectroscopy. *Medical Physics*, 19(4):1065–1069, 1992.
- [112] P. J. Sellin. Recent advances in compound semiconductor radiation detectors. *Nuclear Instruments and Methods in Physics Research Section A: Accelerators, Spectrometers, Detectors and Associated Equipment*, 513(1):332–339, November 2003.

- [113] C. Xu, H. Chen, M. Persson, S. Karlsson, M. Danielsson, C. Svensson, and H. Bornefalk. Energy resolution of a segmented silicon strip detector for photon-counting spectral CT. *Nuclear Instruments and Methods in Physics Research Section A: Accelerators, Spectrometers, Detectors and Associated Equipment*, 715:11–17, July 2013.
- [114] W. Zhao, G. DeCrescenzo, and J. A. Rowlands. Investigation of lag and ghosting in amorphous selenium flat-panel x-ray detectors. In *Medical Imaging 2002: Physics of Medical Imaging*, volume 4682, pages 9–21. International Society for Optics and Photonics, May 2002.
- [115] E. Itoh and M. Iwamoto. Electronic density of state in metal/polyimide Langmuir-Blodgett film interface and its temperature dependence. *Journal of Applied Physics*, 81(4):1790–1797, February 1997.
- [116] F. C. Chiu, C. Y. Lee, and T. M. Pan. Current conduction mechanisms in Pr₂O₃/oxynitride laminated gate dielectrics. *Journal of Applied Physics*, 105(7):074103, April 2009.
- [117] R. A. Street. Thermal generation currents in hydrogenated amorphous silicon pin structures. *Applied Physics Letters*, 57(13):1334–1336, September 1990.
- [118] D. Min, S. Li, M. Cho, and A. R. Khan. Investigation Into Surface Potential Decay of Polyimide by Unipolar Charge Transport Model. *IEEE Transactions on Plasma Science*, 41(12):3349–3358, December 2013.
- [119] K. Taguchi and J. S. Iwanczyk. Vision 20/20: Single photon counting xray detectors in medical imaging. *Medical physics*, 40(10), 2013.
- [120] M. Danielsson, H. Bornefalk, B. Cederstroem, V. Chmill, Bruce H. Hasegawa, M. Lundqvist, D. R. Nygren, and T. Tabar. Dose-efficient system for digital mammography. In *Medical Imaging 2000: Physics of Medical Imaging*, volume 3977, pages 239–249. International Society for Optics and Photonics, April 2000.

- [121] J. Tanguay, H. K. Kim, and Ian A. Cunningham. The role of x-ray Swank factor in energy-resolving photon-counting imaging. *Medical Physics*, 37(12):6205–6211, 2010.
- [122] E. Fredenberg, M. Hemmendorff, B. Cederstrm, M. slund, and M. Danielsson. Contrast-enhanced spectral mammography with a photon-counting detector. *Medical Physics*, 37(5):2017–2029, 2010.
- [123] John M. Lewin, Pamela K. Isaacs, Virginia Vance, and Fred J. Larke. Dual-Energy Contrast-enhanced Digital Subtraction Mammography: Feasibility. *Radiology*, 229(1):261–268, October 2003.
- [124] P. M. Shikhaliev. Projection x-ray imaging with photon energy weighting: experimental evaluation with a prototype detector. *Physics in Medicine and Biology*, 54(16):4971–4992, July 2009.
- [125] M. Locker, P. Fischer, S. Krimmel, H. Kruger, M. Lindner, K. Nakazawa, T. Takahashi, and N. Wermes. Single photon counting X-ray imaging with Si and CdTe single chip pixel detectors and multichip pixel modules. *IEEE Transactions on Nuclear Science*, 51(4):1717–1723, August 2004.
- [126] K. Spartiotis, A. Leppnen, T. Pantsar, J. Pyyhti, Pasi Laukka, K. Muukkonen, O. Mnnist, J. Kinnari, and T. Schulman. A photon counting CdTe gamma- and X-ray camera. *Nuclear Instruments and Methods in Physics Research Section A: Accelerators, Spectrometers, Detectors and Associated Equipment*, 550(1):267–277, September 2005.
- [127] C. Xu, M. Danielsson, and H. Bornefalk. Evaluation of Energy Loss and Charge Sharing in Cadmium Telluride Detectors for Photon-Counting Computed Tomography. *IEEE Transactions on Nuclear Science*, 58(3):614–625, June 2011.
- [128] R. Ballabriga, M. Campbell, E. H. M. Heijne, X. Llopart, and L. Tlustos. The Medipix3 Prototype, a Pixel Readout Chip Working in Single Photon Counting Mode

- With Improved Spectrometric Performance. *IEEE Transactions on Nuclear Science*, 54(5):1824–1829, October 2007.
- [129] C. Szeles. CdZnTe and CdTe materials for X-ray and gamma ray radiation detector applications. *physica status solidi (b)*, 241(3):783–790, 2004.
- [130] C Scheiber. CdTe and CdZnTe detectors in nuclear medicine. *Nuclear Instruments and Methods in Physics Research Section A: Accelerators, Spectrometers, Detectors and Associated Equipment*, 448(3):513–524, July 2000.
- [131] M. Bissonnette, M. Hansroul, E. Masson, S. Savard, S. Cadieux, P. Warmoes, D. Gravel, J. Agopyan, B. Polischuk, W. Haerer, T. Mertelmeier, J. Y. Lo, Y. Chen, J. T. Dobbins Iii, J. L. Jesneck, and S. Singh. Digital breast tomosynthesis using an amorphous selenium flat panel detector. In *Medical Imaging 2005: Physics of Medical Imaging*, volume 5745, pages 529–540. International Society for Optics and Photonics, April 2005.
- [132] S. K. Moore. Better breast cancer detection. *IEEE Spectrum*, 38(5):50–54, May 2001.
- [133] Bo Zhao and Wei Zhao. Imaging performance of an amorphous selenium digital mammography detector in a breast tomosynthesis system. *Medical Physics*, 35(5):1978–1987, 2008.
- [134] W. E. Spear. Transit Time Measurements of Charge Carriers in Amorphous Selenium Films. *Proceedings of the Physical Society. Section B*, 70(7):669–675, July 1957.
- [135] K. Tanioka, J. Yamazaki, K. Shidara, K. Taketoshi, T. Kawamura, S. Ishioka, and Y. Takasaki. An avalanche-mode amorphous Selenium photoconductive layer for use as a camera tube target. *IEEE Electron Device Letters*, 8(9):392–394, September 1987.
- [136] K. Tanioka. High-Gain Avalanche Rushing amorphous Photoconductor (HARP) detector. *Nuclear Instruments and Methods in Physics Research Section A: Acceler-*

- ators, Spectrometers, Detectors and Associated Equipment*, 608(1, Supplement):S15–S17, September 2009.
- [137] J. D. Eskin, H. H. Barrett, and H. B. Barber. Signals induced in semiconductor gamma-ray imaging detectors. *Journal of Applied Physics*, 85(2):647–659, December 1998.
- [138] P. N. Luke. Singlepolarity charge sensing in ionization detectors using coplanar electrodes. *Applied Physics Letters*, 65(22):2884–2886, November 1994.
- [139] S. Ramo. Currents Induced by Electron Motion. *Proceedings of the IRE*, 27(9):584–585, September 1939.
- [140] W. Shockley. Currents to Conductors Induced by a Moving Point Charge. *Journal of Applied Physics*, 9(10):635–636, October 1938.
- [141] Z. He. Review of the ShockleyRamo theorem and its application in semiconductor gamma-ray detectors. *Nuclear Instruments and Methods in Physics Research Section A: Accelerators, Spectrometers, Detectors and Associated Equipment*, 463(1):250–267, May 2001.
- [142] J. D. Eskin, H. H. Barrett, H. B. Barber, and J. M. Woolfenden. The effect of pixel geometry on spatial and spectral resolution in a CdZnTe imaging array. In *1995 IEEE Nuclear Science Symposium and Medical Imaging Conference Record*, volume 1, pages 544–548 vol.1, October 1995.
- [143] H. H. Barrett, J. D. Eskin, and H. B. Barber. Charge Transport in Arrays of Semiconductor Gamma-Ray Detectors. *Physical Review Letters*, 75(1):156–159, July 1995.
- [144] G. F. Knoll. *Radiation Detection and Measurement*. John Wiley & Sons, August 2010. Google-Books-ID: 4vTJ7UDel5IC.

- [145] J. G. Mainprize, D. C. Hunt, and M. J. Yaffe. Direct conversion detectors: The effect of incomplete charge collection on detective quantum efficiency. *Medical Physics*, 29(6):976–990, 2002.
- [146] S. M. Arnab and M. Z. Kabir. Impact of charge carrier trapping on amorphous selenium direct conversion avalanche X-ray detectors. *Journal of Applied Physics*, 122(13):134502, October 2017.
- [147] M. R. Lemacks, S. C. Kappadath, Chris C. Shaw, X. Liu, and G. J. Whitman. A dual-energy subtraction technique for microcalcification imaging in digital mammography—a signal-to-noise analysis. *Medical Physics*, 29(8):1739–1751, August 2002.
- [148] T. Asaga, C. Masuzawa, A. Yoshida, and H. Matsuura. Dual-energy subtraction mammography. *Journal of Digital Imaging*, 8(1):70, February 1995.
- [149] J. M. Boone, G. S. Shaber, and M. Tecotzky. Dual-energy mammography: A detector analysis. *Medical Physics*, 17(4):665–675, July 1990.
- [150] U. Fano. Ionization Yield of Radiations. II. The Fluctuations of the Number of Ions. *Physical Review*, 72(1):26–29, July 1947.
- [151] R. H. Redus, J. A. Pantazis, A. C. Huber, V. T. Jordanov, J. F. Butler, and B. Apotovsky. Fano Factor Determination For CZT. *MRS Online Proceedings Library Archive*, 487, 1997.
- [152] P. Rehak, J. Walton, E. Gatti, A. Longoni, Marco Sanpietro, J. Kemmer, H. Dietl, P. Holl, R. Klanner, G. Lutz, A. Wylie, and H. Becker. Progress in semiconductor drift detectors. *Nuclear Instruments and Methods in Physics Research Section A: Accelerators, Spectrometers, Detectors and Associated Equipment*, 248(2):367–378, August 1986.
- [153] R. K. Swank. Absorption and noise in xray phosphors. *Journal of Applied Physics*, 44(9):4199–4203, September 1973.

- [154] R. Fahrig, J. A. Rowlands, and M. J. Yaffe. X-ray imaging with amorphous selenium: detective quantum efficiency of photoconductive receptors for digital mammography. *Medical Physics*, 22(2):153–160, February 1995.
- [155] F. Salvat, J. Fernandez-Varea, and J. Sempau. Penelope. A code system for Monte Carlo simulation of electron and photon transport. *NEA Data Bank, Workshop Proceeding, Barcelona*, pages 4–7, January 2007.
- [156] Yuan Fang, Andreu Badal, Nicholas Allec, Karim S. Karim, and Aldo Badano. Monte Carlo simulation of amorphous selenium imaging detectors. In *Medical Imaging 2010: Physics of Medical Imaging*, volume 7622, page 762214. International Society for Optics and Photonics, March 2010.
- [157] M. Schieber, A. Zuck, H. Gilboa, and G. Zentai. Reviewing Polycrystalline Mercuric Iodide X-Ray Detectors. *IEEE Transactions on Nuclear Science*, 53(4):2385–2391, August 2006.
- [158] P. R. Bennett, K. S. Shah, L. J. Cirignano, M. B. Klugerman, L. P. Moy, F. Olschner, and M. R. Squillante. Characterization of polycrystalline TlBr films for radiographic detectors. *IEEE Transactions on Nuclear Science*, 46(3):266–270, June 1999.
- [159] M. S. Yun, S. Cho, R. Lee, G. Jang, Y. Kim, W. Shin, and S. Nam. Investigation of PbI₂ Film Fabricated by a New Sedimentation Method as an X-ray Conversion Material. *Japanese Journal of Applied Physics*, 49(4R):041801, April 2010.
- [160] Q. Zhao, L. E. Antonuk, Y. El-Mohri, Y. Wang, Hong Du, A. Sawant, Z. Su, and J. Yamamoto. Performance evaluation of polycrystalline HgI₂ photoconductors for radiation therapy imaging: Performance evaluation of polycrystalline HgI₂ for MV imaging. *Medical Physics*, 37(6Part1):2738–2748, May 2010.
- [161] S. Tokuda, H. Kishihara, S. Adachi, and T. Sato. Preparation and characterization of polycrystalline CdZnTe films for large-area, high-sensitivity X-ray detectors. *Journal of Materials Science: Materials in Electronics*, 15(1):1–8, January 2004.

- [162] K C Young. Recent developments in digital mammography. *Imaging*, 18(2):68–74, June 2006.
- [163] L. T. Jones and P. B. Woollam. Resolution improvement in CdTe gamma detectors using pulse-shape discrimination. *Nuclear Instruments and Methods*, 124(2):591–595, March 1975.
- [164] M. Richter and P. Siffert. High resolution gamma ray spectroscopy with CdTe detector systems. *Nuclear Instruments and Methods in Physics Research Section A: Accelerators, Spectrometers, Detectors and Associated Equipment*, 322(3):529–537, November 1992.
- [165] O. Limousin. New trends in CdTe and CdZnTe detectors for X- and gamma-ray applications. *Nuclear Instruments and Methods in Physics Research Section A: Accelerators, Spectrometers, Detectors and Associated Equipment*, 504(1):24–37, May 2003.
- [166] P. N. Luke. Unipolar charge sensing with coplanar electrodes-application to semiconductor detectors. *IEEE Transactions on Nuclear Science*, 42(4):207–213, August 1995.
- [167] P. N Luke. Electrode configuration and energy resolution in gamma-ray detectors. *Nuclear Instruments and Methods in Physics Research Section A: Accelerators, Spectrometers, Detectors and Associated Equipment*, 380(1):232–237, October 1996.
- [168] P. N. Luke, M. Amman, T. H. Prettyman, P. A. Russo, and D. A. Close. Electrode design for coplanar-grid detectors. *IEEE Transactions on Nuclear Science*, 44(3):713–720, June 1997.
- [169] A. H. Goldan, O. Tousignant, K. S. Karim, and J. A. Rowlands. Unipolar time-differential pulse response with a solid-state Charpak photoconductor. *Applied Physics Letters*, 101(21):213503, November 2012.

- [170] D. L. Y. Lee. Selenium detector with a grid for selenium charge gain. In *Medical Imaging 2005: Physics of Medical Imaging*, volume 5745, pages 216–222. International Society for Optics and Photonics, April 2005.
- [171] D. L. Lee, H. Jang, A. Camlica, and K. S. Karim. A novel radiation imaging detector with proportional charge gain. In *Medical Imaging 2018: Physics of Medical Imaging*, volume 10573, page 105735X. International Society for Optics and Photonics, March 2018.
- [172] J. Stavro, A. H. Goldan, and W. Zhao. SWAD: inherent photon counting performance of amorphous selenium multi-well avalanche detector. In *Medical Imaging 2016: Physics of Medical Imaging*, volume 9783, page 97833Q. International Society for Optics and Photonics, March 2016.
- [173] L. Bombelli, C. Fiorini, T. Frizzi, R. Alberti, and R. Quaglia. High rate X-ray spectroscopy with CUBE preamplifier coupled with silicon drift detector. In *2012 IEEE Nuclear Science Symposium and Medical Imaging Conference Record (NSS/MIC)*, pages 418–420, October 2012.
- [174] L. Bombelli, C. Fiorini, T. Frizzi, R. Alberti, and A. Longoni. CUBE, A low-noise CMOS preamplifier as alternative to JFET front-end for high-count rate spectroscopy. In *2011 IEEE Nuclear Science Symposium Conference Record*, pages 1972–1975, October 2011.
- [175] T. Krings, D. Proti, C. Rossi, L. Bombelli, R. Alberti, and T. Frizzi. High-resolution X-ray spectroscopy with multi-element HPGe- and Si(Li)-detectors and CUBE preamplifiers. *Journal of Instrumentation*, 9(05):C05050–C05050, May 2014.
- [176] C. Fiorini, L. Bombelli, P. Busca, A. Marone, R. Peloso, R. Quaglia, P. Bellutti, M. Boscardin, F. Ficorella, G. Giacomini, A. Picciotto, C. Piemonte, N. Zorzi, N. Nelms, and B. Shortt. Silicon Drift Detectors for Readout of Scintillators in

- Gamma-Ray Spectroscopy. *IEEE Transactions on Nuclear Science*, 60(4):2923–2933, August 2013.
- [177] G. Belev and S. O. Kasap. Reduction of the dark current in stabilized a-Se based X-ray detectors. *Journal of Non-Crystalline Solids*, 352(9):1616–1620, June 2006.
- [178] M. slund, B. Cederstrm, M. Lundqvist, and M. Danielsson. Physical characterization of a scanning photon counting digital mammography system based on Si-strip detectors. *Medical Physics*, 34(6Part1):1918–1925, 2007.
- [179] E. Fredenberg, M. Lundqvist, B. Cederstrm, M. slund, and M. Danielsson. Energy resolution of a photon-counting silicon strip detector. *Nuclear Instruments and Methods in Physics Research Section A: Accelerators, Spectrometers, Detectors and Associated Equipment*, 613(1):156–162, January 2010.
- [180] R. Ballabriga, M. Campbell, E. Heijne, X. Llopart, L. Tlustos, and W. Wong. Medipix3: A 64k pixel detector readout chip working in single photon counting mode with improved spectrometric performance. *Nuclear Instruments and Methods in Physics Research Section A: Accelerators, Spectrometers, Detectors and Associated Equipment*, 633:S15–S18, May 2011.
- [181] H. Kim, S. Han, J. Yang, S. Kim, Y. Kim, S. Kim, D. Yoon, J. Lee, J. Park, Y. Sung, S. Lee, S. Ryu, and G. Cho. A sampling-based 128128 direct photon-counting X-ray image sensor with 3 energy bins and spatial resolution of 60m/pixel. In *2012 IEEE International Solid-State Circuits Conference*, pages 110–112, February 2012.
- [182] L. Abbene, G. Gerardi, S. Del Sordo, and G. Raso. Performance of a digital CdTe X-ray spectrometer in low and high counting rate environment. *Nuclear Instruments and Methods in Physics Research Section A: Accelerators, Spectrometers, Detectors and Associated Equipment*, 621(1):447–452, September 2010.